pyEFPE: An improved post-Newtonian waveform model for inspiralling precessing-eccentric compact binaries

Gonzalo Morras [●],[1, 2, *] Geraint Pratten [●],[2, †] and Patricia Schmidt [●][2, ‡]

[1]*Instituto de Física Teórica UAM/CSIC, Universidad Autónoma de Madrid, Cantoblanco 28049 Madrid, Spain*
[2]*School of Physics and Astronomy and Institute for Gravitational Wave Astronomy,*
University of Birmingham, Edgbaston, Birmingham, B15 2TT, United Kingdom
(Dated: February 7, 2025)

The measurement of spin-precession and orbital eccentricity in gravitational-wave (GW) signals is a key priority in GW astronomy, as these effects not only provide unique insights into the astrophysical formation and evolution of compact binaries but also, if neglected in waveform models, could introduce significant biases in parameter estimation, searches, and tests of General Relativity. Despite the growing potential of upcoming LIGO-Virgo-KAGRA observing runs and future detectors to measure eccentric-precessing signals, accurately and efficiently modeling them remains a significant challenge. In this work, we present pyEFPE, a frequency-domain post-Newtonian (PN) waveform model for the inspiral of precessing-eccentric compact binaries. pyEFPE improves upon previous models by introducing analytical expressions for the Fourier mode amplitudes, enhancing the numerical stability of the multiple scale analysis framework, and adding recently derived PN corrections, critical to accurately describe signals in GW detectors. Additionally, we simplify the numerical implementation and introduce a scheme to interpolate the polarization amplitudes, achieving a speedup of up to $\sim \mathcal{O}(20)$ in the waveform computations, making the model practical for data analysis applications. We thoroughly validate pyEFPE by comparing it to other waveform models in the quasi-circular and eccentric-spin-aligned limits, finding good agreement. Additionally, we demonstrate pyEFPE's capability to analyze simulated GW events, accurately recovering the parameters of signals described by both pyEFPE and IMRPhenomXP. While pyEFPE still lacks important physical effects, such as higher-order PN corrections, higher-order modes, mode asymmetries, tidal interactions or the merger-ringdown phase, it represents a significant step towards more complete waveform models, offering a flexible and efficient framework that can be extended in future work to incorporate these effects.

I. INTRODUCTION

One of the most pressing questions in modern relativistic astrophysics is to understand the formation and evolutionary processes of stellar-mass black holes. Even though the LIGO [1], Virgo [2], and KAGRA [3] detectors are making hundreds of gravitational-wave (GW) detections [4–6], there are still numerous open questions on the interpretation of the underlying astrophysical population [7–11]. Among all the observables, spin-precession [12–14] and eccentricity [15–18] are two of the most exciting as they are thought to be comparatively clean tracers for the underlying astrophysical formation channel. Whilst the majority of current observations seem to be consistent with quasi-circular (non-eccentric) binaries [19], there is tentative evidence that some events may have non-zero eccentricity [20–23], based on analyses using aligned-spin eccentric models. However, it has recently been noted that the complex interplay between spin-precession and residual eccentricity can introduce a systematic uncertainty on astrophysical inference [24, 25], see also [26], underpinning the urgency of developing waveform models that include both effects.

This urgency also extends to the challenges faced by incorporating additional physics in GW searches, e.g. [27–30], and tests of General Relativity, e.g. [31–34].

Furthermore, one of the key science goals for LISA is to trace the origin and evolution of massive black holes [35–37] with mass $M \sim 10^4 - 10^9 M_\odot$. Whilst the population properties of these binaries are highly uncertain, accurate constraints on their masses, spins, and orbital eccentricity will provide crucial insight into black hole seed formation scenarios, galaxy assembly, and the evolution of large scale structure. For example, spin precession could be coupled to the properties of the host galaxy, with binaries in gas-rich environments potentially undergoing a secular alignment of the black hole spin via the Bardeen-Petterson effect [38, 39], itself driven by Lense-Thirring precession [40]. Similarly, orbital eccentricity is thought to be sensitive to the surrounding environment, with several mechanisms being able to generate non-negligible eccentricity through binary-disk interactions [41–47],

It should therefore be apparent that the rapid development of waveform models that accurately capture both spin-precession and eccentricity is one of the key challenges in modern GW astronomy. In the past few years, there has been significant progress in constructing aligned-spin eccentric waveform models. This includes recent progress using post-Newtonian (PN) calculations [48–54], the effective-one-body (EOB) formalism [55–65], and NR informed models [66, 67]. However,

* gonzalo.morras@uam.es
† g.pratten@bham.ac.uk
‡ p.schmidt@bham.ac.uk

only limited progress has been made in the joint modeling of precession and eccentricity [68–76].

In this work, we build upon a series of studies that, over the past few years, have established the foundations for constructing Efficient Fully Precessing Eccentric (EFPE) waveforms [72–74]. Ref. [72] developed much of the formalism for these frequency-domain post-Newtonian waveform models for inspiralling precessing-eccentric compact binaries. Building on this, Ref. [73] introduced a more efficient method to model spin-precession dynamics using a multiple scale analysis (MSA) approach [77–83]. Most recently, Ref. [74] formalized the description of the eccentricity correction to the waveform amplitudes, allowing to extend the domain of validity of EFPE waveforms to moderate eccentricities ($e \lesssim 0.8$). With respect to these works, in `pyEFPE` we introduce several key improvements

1. In Sec. II we derive closed analytical expressions for the Newtonian Fourier mode amplitudes, greatly simplifying the amplitude computation with respect to Ref. [74], while improving the accuracy and speed.

2. In Sec. III we derive self-consistent expressions for the MSA introduced in Ref. [73] and improve its numerical stability, making the `pyEFPE` waveform more stable and less prone to failures.

3. In Sec. IV and in appendix B, we revisit the PN equations, fixing typos and incorporating the recently derived 2.5PN and 3PN aligned-spin eccentric contributions from Ref. [53] into the evolution equations.

4. In Sec. VI we provide a detailed description of the numerical implementation of the `pyEFPE` waveform, demonstrating how to use the Runge-Kutta method to solve the equations of motion and derive frequency-domain waveforms in a simpler and more efficient manner than in Ref. [72]. We also describe how to interpolate the amplitudes to speed up the waveform by a factor up to $\sim \mathcal{O}(20)$ at a minimal cost of accuracy.

5. The `pyEFPE` waveform will be publicly available at https://github.com/gmorras/pyEFPE, making it the first EFPE model widely accessible to the community. Furthermore, its `Python` implementation is designed to be easy to understand, use, and modify.

As for the rest of the paper, in Sec. V, we explain how `pyEFPE` uses the SUA approximation [84] to analytically compute the waveform in the frequency domain, fixing a typo in Refs. [72–74]. In Sec. VII, we thoroughly test and validate `pyEFPE`, verifying that it reproduces the expected phenomenology of inspiral waveforms with spin-precession and orbital eccentricity, performing mismatch comparisons with other waveform models in the quasi-circular and eccentric-spin-aligned limits, and

demonstrating its capability to estimate the parameters of simulated GW signals. Finally, in Sec. VIII we conclude, summarizing our findings and outlining potential directions for future work.

Unless otherwise specified, in this paper we use geometric units ($G = c = 1$), and write vectors in boldface, adding a hat in the case of unit vectors. Additionally, angular momenta are expressed as dimensionless quantities by scaling them with the total mass squared, M^2, such that, for example $\boldsymbol{L} = \boldsymbol{L}^{\text{physical}}/M^2$ or $\boldsymbol{S}_i = \boldsymbol{S}_i^{\text{physical}}/M^2$.

II. GRAVITATIONAL WAVES FROM PRECESSING ECCENTRIC BINARIES

In this section, we derive the GW emission of a precessing eccentric binary, assuming the system's dynamics are known. While these dynamics are thoroughly studied in later sections, starting with the GW emission provides a broad overview of the problem and helps identify the parts of the system requiring modeling. Specifically, we focus on the leading-order (Newtonian) quadrupolar GW emission, e.g. [85], incorporating precession effects in the waveform by performing a time-dependent rotation of the waveform modes [86–89].

A. Newtonian eccentric orbit

At Newtonian order, the orbit of an eccentric binary in the center-of-mass frame can described with the Keplerian parametrization [90, 91]

$$r(u) = a(1 - e\cos u), \tag{1a}$$

$$\phi_N = v(u) \equiv 2\arctan\left[\left(\frac{1+e}{1-e}\right)^{1/2}\tan\frac{u}{2}\right], \tag{1b}$$

$$\ell \equiv n(t - t_0) = u - e\sin u, \tag{1c}$$

where the relative separation vector is given by $\boldsymbol{x} = r(\cos\phi_N, \sin\phi_N, 0)$, a is the semi-major axis, e the eccentricity, $n = 2\pi/P$ the mean motion, where P is the orbital period, and t_0 is a constant of integration; the auxiliary variables u, v and ℓ are the eccentric, true and mean anomalies, respectively.

When PN effects are taken into account, the orbit will no longer be described by Eq. (1), and small perturbations appear. However, the orbit can be written in a similar way, using the "quasi-Keplerian" parametrization [90, 92–95]. Here, we will ignore small periodic corrections to the orbit and only keep the secular effects. In particular, the equation for the orbital phase ϕ will be modified by the periastron advance k [96, 97] to read:

$$\phi = (1 + k)v = (1 + k)\ell + (1 + k)(v - \ell)$$

$$\approx \underbrace{(1+k)\ell}_{\lambda} + \underbrace{v - \ell}_{W} \,. \tag{2}$$

In the first term, the periastron advance k cannot be neglected, even though it is formally of 1PN order, as ℓ becomes very large for long observation times and $k\ell$ induces a significant change in the orbital phase. In the second term, the contribution of k to ϕ is subdominant since $|v - \ell| \leq \pi$ and therefore $k(v - \ell)$ is a small periodic phase change of order 1PN.

The periastron advance can be seen explicitly by looking at the argument of periastron $\delta\lambda = \phi - v$, which tracks the phase of the periastron of the elliptic orbit, and can be computed as

$$\delta\lambda = \lambda - \ell = k\ell \,, \tag{3}$$

which grows linearly in time and is directly proportional to the periastron advance k.

B. Waveform of a spin-precessing binary

To describe the waveform of a spin-precessing binary we follow the descriptions and conventions of Ref. [74]. The GW polarizations, $h_{+,\times}$, can be decomposed in terms of spin-weighted spherical harmonics [98, 99], i.e.,

$$h_+ - ih_\times = \sum_{l=2}^{\infty} \sum_{m=-l}^{l} h^{lm} \, _{-2}Y^{lm}(\Theta_{\rm p}, \Phi_{\rm p}) \,, \tag{4}$$

where $(\Theta_{\rm p}, \Phi_{\rm p})$ are the spherical angles of the wave propagation vector as measured in the inertial binary source frame, and $_{-2}Y^{lm}$ are the spin-weighted spherical harmonics of spin weight -2.

When the spins of the component objects $\boldsymbol{S}_i$ are not aligned with the orbital angular momentum $\boldsymbol{L}$, the system undergoes spin induced precession [100, 101] in which $\boldsymbol{L}$, and therefore the orbital plane, precesses around the total angular momentum $\boldsymbol{J} = \boldsymbol{L} + \boldsymbol{S}_1 + \boldsymbol{S}_2$. This spin-induced orbital precession greatly complicates the structure of the GW modes h_{lm} of Eq. (4) [101]. However, the modes can be mostly simplified by transforming from the inertial to a "co-precessing" frame that is instantaneously aligned with the orbital angular momentum and then, using the dynamics, rotating the co-precessing frame modes H_{lm} back to the inertial frame in which the h^{lm} are defined (Eq. (4)) [86–89]. Note that in the co-precessing frame, precession effects are reduced but not entirely eliminated [89, 102, 103]. The rotation of the modes is given by [86]

$$h^{lm'} = \sum_{m=-l}^{l} D^l_{m'm}(\phi_z, \theta_L, \zeta) H^{lm} \,, \tag{5}$$

where $D^l_{m'm}(\phi_z, \theta_L, \zeta)$ are the Wigner D-matrices and ϕ_z, θ_L and ζ are the three Euler angles that describe the rotation from the co-precessing to the inertial frame. In particular, θ_L is the angle between $\hat{\boldsymbol{L}}$ and $\hat{\boldsymbol{J}}$, ϕ_z is the angle of the projection of $\boldsymbol{L}$ projection onto the plane perpendicular to $\hat{\boldsymbol{J}}$ and ζ is the third Euler angle, fixed by the minimal-rotation condition $\dot{\zeta} = -\dot{\phi}_z \cos\theta_L$ [88, 104].

Therefore, the problem has now simplified to describing the GW modes H^{lm} of an approximately nonprecessing system, which will be functions of the eccentric orbit. Using the quasi-Keplerian parametrization (Eqs. (1,2)), these modes can be expressed as [74]

$$H^{lm}(t) = h_0 \, {\rm e}^{-im\phi(t)} \, K^{lm}[u(t)]$$
$$\equiv h_0 \hat{H}^{lm}(t) \,, \tag{6}$$

where

$$h_0 \equiv 4\sqrt{\frac{\pi}{5}} \frac{M\nu}{d_L} (M\omega)^{2/3} \,, \tag{7}$$

where d_L is the luminosity distance to the binary, $M = m_1 + m_2$ is the total mass, ω is the mean orbital angular velocity, and $\nu = m_1 m_2 / M^2$ is the symmetric mass ratio. Since H^{lm} are the GW modes in the co-precessing frame, ignoring small mode asymmetries [102, 103], they satisfy

$$H^{l-m} = (-1)^l (H^{lm})^* \,. \tag{8}$$

Putting together Eqs. (4,6), the waveform polarizations in the inertial frame are given by

$$h_+ - ih_\times = \sum_{l=2}^{\infty} \sum_{m=-l}^{l} A_{l,m} \hat{H}^{lm} \,, \tag{9}$$

where we have defined

$$A_{l,m}(t) \equiv h_0 \sum_{m'=-l}^{l} {}_{-2}Y^{lm'}(\Theta, \Phi) D^l_{m'm}(\phi_z, \theta_L, \zeta) \,, \tag{10}$$

and (Θ, Φ) are the spherical angles of the binary as measured in the co-precessing frame. Note that, given the rotation formula for spherical harmonics, $A_{l,m}(t)$ is proportional to the inertial frame spherical harmonics. Since h_+ and $h_\times$ are real valued, using Eq. (9) and its complex conjugate, together with the mode symmetry of Eq. (8) we can separate the two polarizations as

$$h_{+,\times}(t) = \sum_{l=2}^{\infty} \sum_{m=-l}^{l} {\sf A}_{l,m}^{+,\times} \hat{H}^{lm} \,, \tag{11}$$

where we have defined

$$\mathsf{A}_{l,m}^+ = \frac{1}{2} \left[A_{l,m} + (-1)^l (A_{l,-m})^* \right] \,, \tag{12a}$$

$$\mathsf{A}_{l,m}^\times = \frac{i}{2} \left[A_{l,m} - (-1)^l (A_{l,-m})^* \right] \,. \tag{12b}$$

Note that the $\mathsf{A}_{l,m}^{+,\times}$ amplitudes also satisfy a mode symmetry similar to Eq. (8), i.e.

$$\mathsf{A}_{l,-m}^{+,\times} = (-1)^l (\mathsf{A}_{l,m}^{+,\times})^* \qquad (13)$$

Using $(D_{m'-m}^l)^* = (-1)^{m'+m} D_{-m'm}^l$, we can simplify Eq. (12) as

$$\mathsf{A}_{l,m}^{+,\times} = h_0 \sum_{m'=-l}^{l} \mathsf{P}_{l,m,m'}^{+,\times}(\Theta, \Phi) D_{m'm}^l(\phi_z, \theta_L, \zeta), \quad (14\text{a})$$

$$\mathsf{P}_{l,m,m'}^{+} = \frac{1}{2} \left[{}_{-2}Y^{lm'} + (-1)^{l+m+m'} ({}_{-2}Y^{l-m'})^* \right], \qquad (14\text{b})$$

$$\mathsf{P}_{l,m,m'}^{\times} = \frac{\mathrm{i}}{2} \left[{}_{-2}Y^{lm'} - (-1)^{l+m+m'} ({}_{-2}Y^{l-m'})^* \right], \qquad (14\text{c})$$

where the $\mathsf{P}_{l,m,m'}^{+,\times}(\Theta, \Phi)$ terms remain constant throughout the evolution and therefore need to only be computed once at initialization.

To compute the GW polarizations as a function of time we need to evaluate the co-precessing GW modes $\hat{H}^{lm'}(\ell, u(\ell))$. Naively, this requires numerically solving the transcendental Eq. (1c) to obtain the eccentric anomaly u as a function of the mean anomaly ℓ. However, this can be avoided by writing the GW modes as a Fourier series in the mean anomaly, which will also prove useful when transforming the GW signal to the frequency domain. Therefore, we follow [74] and write

$$\hat{H}^{lm} = \mathrm{e}^{-\mathrm{i}m\lambda} \sum_{p=-\infty}^{\infty} N_p^{lm} \, \mathrm{e}^{-\mathrm{i}p\ell}, \qquad (15)$$

where we have separated the mean orbital phase term $\mathrm{e}^{-\mathrm{i}m\lambda}$, since it is not 2π-periodic in ℓ [96], and N_p^{lm} are the Fourier series coefficients, which are defined by

$$N_p^{lm} = \frac{1}{2\pi} \int_{-\pi}^{\pi} \left(\mathrm{e}^{\mathrm{i}m\lambda} \hat{H}^{lm} \right) \mathrm{e}^{\mathrm{i}p\ell} \, \mathrm{d}\ell. \qquad (16)$$

From the mode symmetry of Eq. (8) and Eq. (15), we can deduce that

$$N_p^{l-m} = (-1)^l (N_{-p}^{lm})^*. \qquad (17)$$

Substituting Eq. (15) in Eq. (11), and writing the eccentric anomaly in terms of the argument of periastron $\delta\lambda = \lambda - \ell$, we can finally express the GW waveform as [74]

$$h_{+,\times}(t) = \sum_{l=2}^{\infty} \sum_{m=-l}^{l} \sum_{n=-\infty}^{\infty} \mathcal{A}_{l,m,n}^{+,\times}(t) \, \mathrm{e}^{-\mathrm{i}(n\lambda + (m-n)\delta\lambda)}, \qquad (18)$$

where

$$\mathcal{A}_{l,m,n}^{+,\times}(t) = N_{n-m}^{lm}(t) \mathsf{A}_{l,m}^{+,\times}(t). \qquad (19)$$

In the argument of the exponential of Eq. (18), we have explicitly separated the contributions of the rapidly evolving mean orbital phase λ from the slowly evolving argument of periastron $\delta\lambda$. Finally, the spin-precession effects are captured by the slow time variation of the coefficients $\mathcal{A}_{l,m,n}^{+,\times}(t)$.

C. Newtonian Fourier Mode Amplitudes

In this subsection, and in `pyEFPE`, we consider the amplitudes to leading order in the post-Newtonian (PN) expansion, also called the Newtonian order. The only GW modes that contribute at this Newtonian order are the ones with $l = 2$, $m = \{0, \pm 2\}$, given by [74, 85]

$$\hat{H}^{20} = \sqrt{\frac{2}{3}} \frac{e \cos u}{1 - e \cos u}, \qquad (20\text{a})$$

$$\hat{H}^{22} = \frac{2 \, \mathrm{e}^{-2\mathrm{i}\phi}}{1 - e \cos u} \left(\frac{1 - e^2 + \mathrm{i}e\sqrt{1 - e^2} \sin u}{1 - e \cos u} - \frac{e}{2} \cos u \right), \qquad (20\text{b})$$

where $\hat{H}^{2-2}$ can be obtained from Eq. (20b) by using the property of Eq. (8). For a generic function of u, we can write its Fourier transform with respect to ℓ (Eq. (16)) as the following integral over u

$$\frac{1}{2\pi} \int_{-\pi}^{\pi} f(u(l)) \, \mathrm{e}^{\mathrm{i}p\ell} \, \mathrm{d}\ell = \frac{1}{2\pi} \int_{-\pi}^{\pi} f(u) \, \mathrm{e}^{\mathrm{i}p\ell(u)} \frac{\mathrm{d}\ell}{\mathrm{d}u} \mathrm{d}u,$$

$$= \frac{1}{2\pi} \int_{-\pi}^{\pi} (1 - e \cos u) f(u) \, \mathrm{e}^{\mathrm{i}p(u - e \sin u)} \, \mathrm{d}u. \qquad (21)$$

The coefficients N_p^{20} can be computed by substituting the corresponding mode (Eq. (20a)) in Eq. (21)

$$N_p^{20} = \frac{1}{2\pi} \int_{-\pi}^{\pi} \frac{e}{\sqrt{6}} \left(\mathrm{e}^{iu} + \mathrm{e}^{-iu} \right) \mathrm{e}^{\mathrm{i}p(u - e \sin u)} \, \mathrm{d}u$$

$$= \frac{e}{\sqrt{6}} (J_{p+1}(pe) + J_{p-1}(pe)), \qquad (22)$$

where $J_n(z)$ is the Bessel function of integer order n [105], defined as

$$J_n(z) = \frac{1}{2\pi} \int_{-\pi}^{\pi} \mathrm{e}^{\mathrm{i}(nu - z \sin u)} \, \mathrm{d}u \quad (n \in \mathbb{Z}). \qquad (23)$$

In the $p = 0$ case, we note that the integral of Eq. (22) could have been trivially computed to yield $N_0^{20} = 0$, while in the case $p \neq 0$ we use the recurrence relations of the Bessel functions [105] to write:

$$N_p^{20} = \begin{cases} 0 & , \ p = 0 \\ \sqrt{\frac{2}{3}} J_p(pe) & , \ p \neq 0 \end{cases}, \qquad (24)$$

in agreement with the expression found in [74].

Computing N_p^{22} is more difficult, since substituting Eq. (20a) in Eq. (21) leads to an integral that seems a-priori very complicated. To simplify this integral we begin by using Eq. (1b) for $v(u)$ together with basic trigonometric relations to write

$$e^{-iv(u)} = \frac{\cos u - e - i\sqrt{1 - e^2} \sin u}{1 - e \cos u}. \qquad (25)$$

In Eq. (20b) for $\hat{H}^{22}$, we use Eq. (2) to expand $\phi = \lambda + v - \ell$ together with Eq. (25) to write

$$\hat{H}^{22} = \frac{2 \, e^{-2i\lambda} \, e^{2i\ell}}{1 - e \cos u} \left(\frac{\cos u - e - i\sqrt{1 - e^2} \sin u}{1 - e \cos u} \right)^2$$
$$\times \left(\frac{1 - e^2 + ie\sqrt{1 - e^2} \sin u}{1 - e \cos u} - \frac{e}{2} \cos u \right). \qquad (26)$$

Note that we can always write Eq. (26) as

$$\hat{H}^{22} = e^{-2i\lambda} \, e^{2i\ell} \frac{dF^{22}}{d\ell}, \qquad (27)$$

where the derivative with respect to ℓ is computed as

$$\frac{d}{d\ell} = \frac{du}{d\ell} \frac{d}{du} = \frac{1}{1 - e \cos u} \frac{d}{du}. \qquad (28)$$

The expression of F^{22} can be computed by integration of Eq. (27), where we find

$$F^{22}(u) = \frac{i}{1 - e \cos u} \left(-\sqrt{1 - e^2} + ie \sin u \right.$$
$$\left. + \sqrt{1 - e^2} \cos 2u - i \left(1 - \frac{e^2}{2} \right) \sin 2u \right). \qquad (29)$$

Substituting Eq. (27) in Eq. (16), we have

$$N_p^{22} = \frac{1}{2\pi} \int_{-\pi}^{\pi} \frac{dF^{22}}{d\ell} e^{i(p+2)\ell} \, d\ell,$$
$$= \frac{-i(p+2)}{2\pi} \int_{-\pi}^{\pi} F^{22} e^{i(p+2)\ell} \, d\ell, \qquad (30)$$

where we have used the formula for the Fourier series of the derivative of a function. If we use the same trick as in Eq. (21) to write the integral in terms of u, the combination $(1 - e \cos u)F^{22}(u)$ appears in the integrand. As can be seen in Eq. (29), this is a finite series of trigonometric functions. Therefore, the integral in Eq. (30) can be computed in terms of Bessel functions in the same way

as was done in Eq. (24). Finally, the Fourier coefficients N_p^{22} are given by:

$$N_{j-2}^{22} = j \left(-\sqrt{1 - e^2} J_j(je) + \frac{e}{2}(J_{j+1}(je) - J_{j-1}(je)) \right.$$
$$+ \frac{1}{2} \left(\sqrt{1 - e^2} + \left(1 - \frac{e^2}{2} \right) \right) J_{j-2}(je)$$
$$\left. + \frac{1}{2} \left(\sqrt{1 - e^2} - \left(1 - \frac{e^2}{2} \right) \right) J_{j+2}(je) \right). \qquad (31)$$

We note that Eq. (31) gives a straightforward closed-form analytical expression for the $l = m = 2$ Fourier mode amplitudes. This is in stark contrast with the complicated infinite nested sums of Ref. [74]. In App. A, we demonstrate the level of agreement between the exact expressions in Eq. (31) and the nested sums in [74], finding good agreement. The Bessel functions, which appear in the Fourier mode amplitudes of Eqs. (24, 31), have very efficient implementations [106], available in widely used software packages [107]. Consequently, in the form presented in this section, the Newtonian Fourier mode amplitudes are simple and fast to compute.

D. Fourier modes that have to be included

In order to make the waveform model as efficient as possible, in Eq. (18) we will want to include as few Fourier modes as possible to describe the strain with a given tolerance. To do this, we start by use the orthogonality relations of the tensor spherical harmonics $_{-2}Y^{lm}(\Theta, \Phi)$ and the Wigner D-matrices $D_{m'm}^l(\phi_z, \theta_L, \zeta)$, i.e.

$$\int \frac{d\Omega}{4\pi} {}_{-2}Y^{l_1 m_1} ({}_{-2}Y^{l_2 m_2})^* = \delta_{l_1 l_2} \delta_{m_1 m_2}, \qquad (32a)$$

$$\int \frac{d\Omega}{4\pi} \int_0^{2\pi} \frac{d\zeta}{2\pi} D_{m_1' m_1}^{l_1} (D_{m_2' m_2}^{l_2})^* = \frac{\delta_{l_1 l_2} \delta_{m_1' m_2'} \delta_{m_1 m_2}}{2l + 1} \qquad (32b)$$

together with the GW waveform of Eq. (9), to prove that

$$\langle |h_+|^2 + |h_\times|^2 \rangle = \sum_{l=2}^{\infty} \sum_{m=-l}^{l} |H^{lm}|^2,$$
$$= \sum_{l=2}^{\infty} \left(|H^{l0}|^2 + 2 \sum_{m=1}^{l} |H^{lm}|^2 \right), \qquad (33)$$

where we have used the mode symmetry of Eq. (8). To find out how many Fourier modes have to be included, we compute the average value of $\langle |h_+|^2 + |h_\times|^2 \rangle$ over one orbital cycle, i.e.

$$\|h\|^2 = \int_{-\pi}^{\pi} \frac{d\ell}{2\pi} \langle |h_+|^2 + |h_\times|^2 \rangle,$$

$$= \sum_{l=2}^{\infty} \left(\|H^{l0}\|^2 + 2 \sum_{m=1}^{l} \|H^{lm}\|^2 \right) , \quad (34)$$

where we have defined

$$\|\hat{H}^{lm}\|^2 = \int_{-\pi}^{\pi} \frac{\mathrm{d}\ell}{2\pi} |H^{lm}(\ell)|^2 , \quad (35)$$

$$= \sum_{p=-\infty}^{\infty} |N_p^{lm}|^2 , \quad (36)$$

and in the second line of Eq. (36) we have substituted the Fourier series of $\hat{H}^{lm}$, defined in Eq. (15). In real applications, we include a finite number of terms in the Fourier series of $\hat{H}^{lm}$, inducing an error in the strain which we will want to keep under control.

Restricting ourselves to the Newtonian amplitudes, we can compute the norms of $\|\hat{H}^{20}\|$ and $\|\hat{H}^{22}\|$ in closed form using Eq. (20), together with Eq. (1c)

$$\|\hat{H}^{20}\|^2 = \frac{2}{3} \int_{-\pi}^{\pi} \frac{\mathrm{d}u}{2\pi} \frac{e^2 \cos^2 u}{1 - e \cos u} = \frac{2}{3} \left(\frac{1}{\sqrt{1-e^2}} - 1 \right) , \quad (37a)$$

$$\|\hat{H}^{20}\|^2 = 4 \int_{-\pi}^{\pi} \frac{\mathrm{d}u}{2\pi} \frac{\left| \frac{1-e^2+\mathrm{i}e\sqrt{1-e^2}\sin u}{1-e\cos u} - \frac{e}{2}\cos u \right|^2}{1 - e\cos u},$$

$$= \frac{5}{\sqrt{1-e^2}} - 1 . \quad (37b)$$

Therefore, when only considering the Newtonian amplitudes, using Eqs. (34,37) we have that

$$\|h\|^2 = \frac{4}{3} \left(\frac{4}{\sqrt{1-e^2}} - 1 \right) , \quad (38)$$

$$= 2 \left(\sum_{p_0=1}^{\infty} |N_{p_0}^{20}|^2 + \sum_{p_2=-\infty}^{\infty} |N_{p_2}^{22}|^2 \right) , \quad (39)$$

where we have used that $N_{-p}^{20} = N_p^{20}$. To minimize the number of terms that have to be included in the sums of Eq. (39), we order the mode amplitudes $\{|N_p^{20}|^2, |N_p^{22}|^2\}$ from larger to smaller and take a sufficient number of them such that the error on $\|h\|^2$ is smaller than a given tolerance ϵ_N, i.e.

$$\frac{\|h\|^2 - 2 \left(\sum_{p_0 \in \boldsymbol{p}_0^{\mathrm{sel}}} |N_{p_0}^{20}|^2 + \sum_{p_2 \in \boldsymbol{p}_2^{\mathrm{sel}}} |N_{p_2}^{22}|^2 \right)}{\|h\|^2} < \epsilon_N , \quad (40)$$

where $\boldsymbol{p}_0^{\mathrm{sel}}$ and $\boldsymbol{p}_2^{\mathrm{sel}}$ represent the $(l,m) = (2,0)$ and $(l,m) = (2,\pm2)$ modes with largest norms that have to be selected. In Fig. 1 we show, as a function of eccentricity e, how many Fourier modes are needed to represent the strain with different tolerances. We can observe that for small eccentricities, it is enough to include only one mode, which corresponds to the usual N_0^{22} mode, that
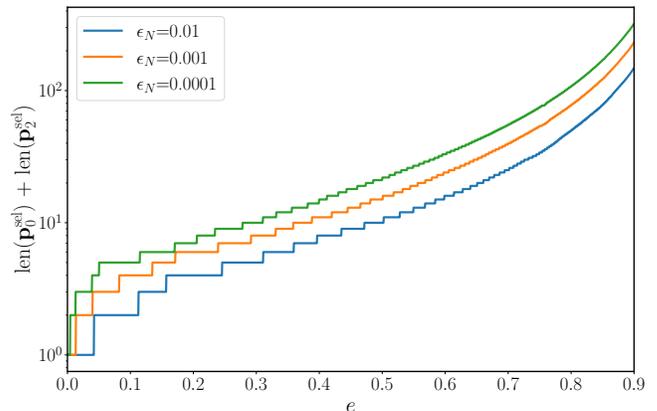

FIG. 1: Number of Fourier modes N_p^{2m} needed to represent the strain h with different tolerances as a function of eccentricity. The number of modes is given by adding the length of the vectors $\boldsymbol{p}_0^{\mathrm{sel}}$ and $\boldsymbol{p}_2^{\mathrm{sel}}$, defined in Eq. (40).

is, the only N_p^{lm} that does not vanish when e goes to 0. As the eccentricity increases, the number of modes we have to include also increases, becoming infinite in the limit $e \to 1$. We also observe that, at a given eccentricity, smaller the tolerances require more modes to be included.

III. SPIN PRECESSION DESCRIPTION

In this section we closely follow Ref. [73] to model the spin-precession (SP) of compact objects in eccentric orbits using a multiple scale analysis (MSA) approach. While the core idea and procedure are based on Ref. [73], we fix a few typos therein and rewrite equations in a simpler form, improving their numerical stability and precision to make pyEFPE more stable and less prone to failures. Whilst we could numerically evolve the full system of equations, e.g. [104], resulting in a more accurate description of the precession dynamics, it can become computationally prohibitive for the low mass binaries seen in ground-based detectors [108] and the long-lived binaries expected in LISA [37]. These limitations become even more pronounced when simultaneously accounting for precession and eccentricity. This motivates our detailed exploration of the MSA system of equations.

The MSA approximation uses that the radiation reaction (RR) time-scale is much longer than the SP time-scale to analytically solve the SP equations in the absence of RR, and then we add the RR by varying some of the constants of the SP solution. In the absence of RR, including leading PN order spin-orbit and spin-spin interactions, the SP equations are given by [72, 73, 109]:

$$\mathcal{D}\hat{\boldsymbol{L}} = -y^6 \left(\boldsymbol{\Omega}_1 + \boldsymbol{\Omega}_2 \right) , \quad (41a)$$

$$\mathcal{D}\boldsymbol{s}_1 = \mu_2 y^5 \boldsymbol{\Omega}_1 , \quad (41b)$$

$$\mathcal{D}\boldsymbol{s}_2 = \mu_1 y^5 \boldsymbol{\Omega}_2 \,, \tag{41c}$$

where we have used the following definitions [73]

$$\mathcal{D} = \frac{M}{(1-e^2)^{3/2}} \frac{d}{dt} \,, \tag{42a}$$

$$y = \frac{(M\omega)^{1/3}}{\sqrt{1-e^2}} \,, \tag{42b}$$

$$\mu_i = \frac{m_i}{M} \,, \tag{42c}$$

$$\boldsymbol{s}_i = \frac{\boldsymbol{S}_i}{\mu_i} \,, \tag{42d}$$

$$L = \frac{\nu}{y} \,, \tag{42e}$$

$$\boldsymbol{\Omega}_i = \left[\frac{1}{2}\mu_i + \frac{3}{2}\left(1 - y\hat{\boldsymbol{L}}\cdot\boldsymbol{s}\right)\right]\hat{\boldsymbol{L}} \times \boldsymbol{s}_i + \frac{1}{2}y\boldsymbol{s}_j \times \boldsymbol{s}_i \,, \tag{42f}$$

and m_i are the individual masses, $\boldsymbol{S}_i$ are the individual spins, $\boldsymbol{L}$ is the Newtonian angular momentum, $M = m_1 + m_2$ is the total mass, e is the orbital eccentricity, y is a PN parameter related to the norm of $\boldsymbol{L}$, ω is the mean orbital angular velocity, μ_i are the dimensionless mass parameters, $\nu = \mu_1\mu_2$ is the symmetric mass ratio, $\boldsymbol{s}_i$ are the reduced individual spins, and $\boldsymbol{s} = \boldsymbol{s}_1 + \boldsymbol{s}_2$ is the total reduced spin.

The SP equations of Eq. (41) contain seven conserved quantities. The norm of the orbital angular momentum L and the three components of the total angular momentum vector $\boldsymbol{J} = \boldsymbol{L} + \mu_1\boldsymbol{s}_1 + \mu_2\boldsymbol{s}_2$ are conserved only when ignoring RR, while the norm of the spin vectors s_1 and s_2 and the effective spin parameter χ_{eff} are also conserved in the presence of RR. Here χ_{eff} is given by [110–112]

$$\chi_{\text{eff}} = \hat{\boldsymbol{L}} \cdot \boldsymbol{s} \,. \tag{43}$$

Taking into account these seven constants of motion, the SP equations of Eq. (41) have only two dynamical variables left. We can go to a non-inertial frame where the z-axis is aligned with $\boldsymbol{J}$, and where the orbital angular momentum $\boldsymbol{L}$ is perpendicular to the y-axis, with $\hat{\boldsymbol{L}} \cdot \hat{\boldsymbol{x}} \geq 0$ [113], i.e.

$$\hat{\boldsymbol{L}} = \sin\theta_L \hat{\boldsymbol{x}} + \cos\theta_L \hat{\boldsymbol{z}} \,, \tag{44}$$

with $\theta_L \in [0, \pi]$. In this J-aligned frame, the angular momenta can all be expressed in terms of one variable, which as in Ref. [73] we choose to be the reduced aligned-spin difference

$$\delta\chi = \hat{\boldsymbol{L}} \cdot (\boldsymbol{s}_1 - \boldsymbol{s}_2) \,. \tag{45}$$

Using the SP equations of Eq. (41), the derivative of $\delta\chi$ can be written as

$$\begin{aligned} \mathcal{D}\delta\chi &= (\mathcal{D}\hat{\boldsymbol{L}}) \cdot (\boldsymbol{s}_1 - \boldsymbol{s}_2) + \hat{\boldsymbol{L}} \cdot (\mathcal{D}\boldsymbol{s}_1 - \mathcal{D}\boldsymbol{s}_2) \,, \\ &= 3(1 - y\chi_{\text{eff}})\left(\hat{\boldsymbol{L}} \times \boldsymbol{s}_1\right) \cdot \boldsymbol{s}_2 \,. \end{aligned} \tag{46}$$

Using the orbital angular momentum in the frame of Eq. (44), and the conserved quantities previously described, we can write Eq. (46) as [73]

$$(\mathcal{D}\delta\chi)^2 = \frac{9}{4}A^2 y^{11}\left(\delta\mu\delta\chi^3 + B\delta\chi^2 + C\delta\chi + D\right) \,, \tag{47}$$

where

$$\delta\mu = \mu_1 - \mu_2 \,, \tag{48}$$

and the coefficients of the cubic polynomial take the following values

$$A = 1 - y\chi_{\text{eff}}, \tag{49a}$$

$$B = \frac{y}{2\nu^2}\left[-2\nu\left(J^2 - L^2 - L\chi_{\text{eff}}\right) + \delta\mu\left(S_1^2 - S_2^2\right) - \delta\mu^2\left(2L^2 + S_1^2 + S_2^2\right)\right] \,, \tag{49b}$$

$$C = \frac{y}{2\nu^2}\left\{\left(1 + \delta\mu^2\right)\chi_{\text{eff}}\left(S_1^2 - S_2^2\right) + 2\delta\mu\left[2L\left(J^2 - L^2 - L\chi_{\text{eff}}\right) - \left(2L + \chi_{\text{eff}}\right)\left(S_1^2 + S_2^2\right) - \nu L\chi_{\text{eff}}^2\right]\right\} \,, \tag{49c}$$

$$\begin{aligned} D = \frac{y}{2\nu^2}\Big\{ &-2\left(J^2 - L^2 - L\chi_{\text{eff}}\right)\left[J^2 - L^2 - L\chi_{\text{eff}} - 2\left(S_1^2 + S_2^2\right) - \nu\chi_{\text{eff}}^2\right] \\ &+ \left(S_1^2 - S_2^2\right)\left[\delta\mu\chi_{\text{eff}}^2 - 2\left(S_1^2 - S_2^2\right)\right] - \chi_{\text{eff}}^2\left(S_1^2 + S_2^2\right)\Big\} \,. \end{aligned} \tag{49d}$$

During the inspiral, the PN parameter y is small ($y \ll 1$) and thus $J \sim L \gg S_{1,2}$. This leads to large numerical cancellations in Eq. (49). To mitigate against this, we define Δ_{J^2} such that

$$J^2 = \left(L + \frac{1}{2}(\chi_{\text{eff}} + \delta X_0)\right)^2 + S_{1\perp,0}^2 + S_{2\perp,0}^2 + \nu\Delta_{J^2} \,, \tag{50}$$

where we have defined

$$\delta X_0 = \delta\mu\,\delta\chi_0\,, \tag{51a}$$

$$S_{i\perp,0}^2 = \|\boldsymbol{S}_{i\perp,0}\|^2 = \left\|\boldsymbol{S}_{i,0} - (\hat{\boldsymbol{L}}_0 \cdot \boldsymbol{S}_{i,0})\hat{\boldsymbol{L}}_0\right\|^2\,, \tag{51b}$$

and the subscript "0" denotes that the value at the initial time is taken. Since δX_0 and $S_{i\perp,0}$ are constants by definition, and J, L and $\chi_{\rm eff}$ are constants of motion of the SP equations, in the absence of RR, Δ_{J^2} is also constant, taking the value

$$\Delta_{J^2} = 2\boldsymbol{s}_{1\perp,0} \cdot \boldsymbol{s}_{2\perp,0}\,. \tag{52}$$

However, when adding the effects of RR, we will see in Sec. IV that Δ_{J^2} slowly varies on the RR time-scale. Substituting Eq. (50) into Eqs. (49), we arrive at the following simpler expressions that avoid large numerical cancellations:

$$B = -\frac{\delta\mu^2}{y} - y\chi_{\rm eff}^2 - \delta X_0 - b_\perp\,, \tag{53a}$$

$$\delta\mu\,C = \delta X_0\left[2\left(\frac{\delta\mu^2}{y} + y\chi_{\rm eff}^2\right) - \delta X_0\right] - c_\perp, \tag{53b}$$

$$\delta\mu^2 D = -\delta X_0^2\left[\frac{\delta\mu^2}{y} + y\chi_{\rm eff}^2 - \delta X_0 - b_\perp\right] + \delta X_0 c_\perp + d_\perp\,. \tag{53c}$$

where we separate in $b_\perp$, $c_\perp$ and $d_\perp$ the part of the coefficients that vanishes in the aligned spin case, where precession should not be present. Explicitly, these are given by

$$b_\perp = y\left(s_{1\perp,0}^2 + s_{2\perp,0}^2 + \Delta_{J^2}\right)\,, \tag{54a}$$

$$c_\perp = -2\delta\mu\left[\delta\mu\Delta_{J^2} + (s_{1\perp,0}^2 - s_{2\perp,0}^2)y\chi_{\rm eff}\right]\,, \tag{54b}$$

$$d_\perp = y\delta\mu^2\left(4s_{1\perp,0}^2 s_{2\perp,0}^2 - \Delta_{J^2}^2\right)\,. \tag{54c}$$

The differential equation of Eq. (47) can be solved analytically in terms of the roots of the cubic polynomial on the right hand side. That is, if we write [73]

$$(\mathcal{D}\delta\chi)^2 = -\frac{1}{y}\left(\frac{3}{2}Ay^6\right)^2$$
$$\times (\delta\chi - \delta\chi_+)(\delta\chi - \delta\chi_-)(\delta\chi_3 - \delta\mu\delta\chi)\,, \tag{55}$$

$$\delta\chi_- \leq \delta\chi_+ \leq \frac{\delta\chi_3}{\delta\mu}\,, \tag{56}$$

then the solution of this equation is [73]

$$\delta\chi = \delta\chi_- + (\delta\chi_+ - \delta\chi_-)\,{\rm sn}^2(\psi_{\rm p}; m)\,, \tag{57}$$
$$\tag{58}$$

where

$$m = \frac{\delta\mu(\delta\chi_+ - \delta\chi_-)}{\delta\chi_3 - \delta\mu\delta\chi_-}\,, \tag{59a}$$

$$\mathcal{D}\psi_{\rm p} = \frac{3Ay^6}{4}\sqrt{\frac{1}{y}(\delta\chi_3 - \delta\mu\delta\chi_-)}\,, \tag{59b}$$

and ${\rm sn}(\psi_{\rm p}; m) = \sin({\rm am}(\psi_{\rm p}; m))$ is the Jacobi elliptic sine function, with ${\rm am}(\psi_{\rm p}; m)$ being the Jacobi amplitude. We use the same conventions for the elliptic functions and integrals as in Ref. [73]. To find the roots of the cubic polynomial, we start computing the coefficients of its depressed cubic as

$$p = \frac{1}{y^2}\left(\frac{B^2}{3} - \delta\mu C\right)\,,$$
$$= \frac{1}{y^2}\left(3p_\parallel^2 + 2p_\perp\right)\,, \tag{60a}$$

$$q = \frac{1}{y^3}\left(\frac{2B^3}{27} - \frac{B\delta\mu C}{3} + \delta\mu^2 D\right)\,,$$
$$= \frac{1}{y^3}\left(-2(p_\parallel^2 + p_\perp)p_\parallel + d_\perp\right)\,, \tag{60b}$$

where it can be shown that $p > 0$. To avoid numerical instabilities, we separate in $p_\parallel$ the terms that are non-zero in the aligned spin case and in $p_\perp$ the ones that vanish. Explicitly, they are given by

$$p_\parallel = \frac{1}{3}\left(\frac{\delta\mu^2}{y} + y\chi_{\rm eff}^2 - 2\delta X_0 + b_\perp\right)\,, \tag{61a}$$

$$p_\perp = \delta X_0 b_\perp + \frac{1}{2}c_\perp\,. \tag{61b}$$

Similarly to [73], the roots of the cubic polynomial of Eq. (55) can be written in terms of

$$Y_3 = 2\sqrt{\frac{p}{3}}\cos\left[\frac{\arg(G)}{3}\right]\,, \tag{62a}$$

$$Y_\pm = 2\sqrt{\frac{p}{3}}\cos\left[\frac{\arg(G) \mp 2\pi}{3}\right]\,, \tag{62b}$$

$$G = -\frac{q}{2} + i\left[\left(\frac{p}{3}\right)^3 - \left(\frac{q}{2}\right)^2\right]^{1/2}$$
$$= -\frac{q}{2} + \frac{i}{y^3}\left[\frac{p_\perp^2(p_\parallel^2 + 8p_\perp)}{27} + (p_\parallel^2 + p_\perp)p_\parallel d_\perp - \frac{d_\perp^2}{4}\right]^{1/2}\,, \tag{62c}$$

$$dY = \frac{B}{3y}\,, \tag{62d}$$

such that

$$\delta\chi_3 = y\left(Y_3 - dY\right)\,, \tag{63a}$$

$$\delta\chi_\pm = \frac{y}{\delta\mu}\left(Y_\pm - dY\right)\,. \tag{63b}$$

Note that in Eq. (62c) we have simplified the square root term to avoid the large numerical cancellations. From
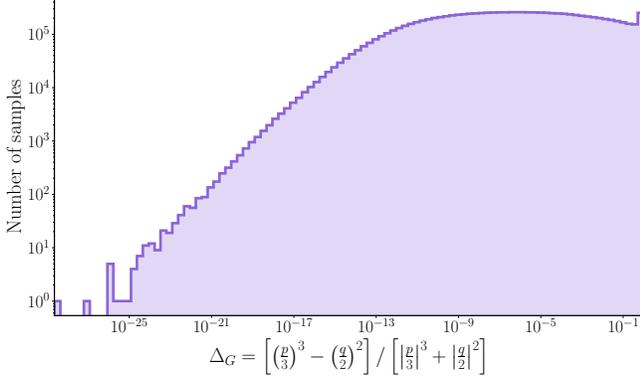
FIG. 2: Histogram of Δ_G computed for 10^7 random samples drawn from a distribution isotropic in spin orientations, uniform in dimensionless spin magnitudes $\chi_i = s_i/\mu_i \in [0,1]$, uniform in mass ratio $q = m_2/m_1 \in [0,1]$ and log-uniform in the PN parameter $y \in [0.001, 6^{-1/2}]$.

Eq. (61) we expect that $|p_\parallel| \gg |p_\perp|$ and $|p_\parallel| \gg d_\perp$, and thus $\left(\frac{p}{3}\right)^3 \sim \left(\frac{q}{2}\right)^2 \sim \mathcal{O}\left(p_\parallel^6\right)$. However, when we compute the difference between these two terms in Eq. (62c), we get $\left(\frac{p}{3}\right)^3 - \left(\frac{q}{2}\right)^2 \sim \mathcal{O}\left(p_\parallel^3 d_\perp\right)$ which is much smaller, and points to a large numerical cancellation happening. To illustrate this point, we show in Fig. 2 the level of cancellation by plotting the distribution of

$$\Delta_G = \left[\left(\frac{p}{3}\right)^3 - \left(\frac{q}{2}\right)^2\right] / \left[\left|\frac{p}{3}\right|^3 + \left|\frac{q}{2}\right|^2\right], \quad (64)$$

for random angular momenta and masses, as described in the figure caption. For $\Delta_G \lesssim 10^{-12}$, which as we observe in Fig. 2 is quite common, we expect the numerical error to have a large impact when using 64 bit floating precision numbers.

Using the quantities defined in Eq. (62), we can simplify Eq. (59) as

$$\mathcal{D}\psi_{\mathrm{p}} = \frac{3Ay^6}{4}\sqrt{Y_3 - Y_-}, \quad (65a)$$

$$m = \frac{Y_+ - Y_-}{Y_3 - Y_-} = \frac{\sin\left[\frac{\arg(G)}{3}\right]}{\cos\left[\frac{\arg(G)}{3} - \frac{\pi}{6}\right]}. \quad (65b)$$

It will also be convenient to write the solution of $\delta\chi$ of Eq. (57) as

$$\delta\chi = \delta\chi_{\mathrm{av}} - \delta\chi_{\mathrm{diff}}\left(1 - 2\mathrm{sn}^2(\psi_{\mathrm{p}}, m)\right), \quad (66)$$

where we have defined

$$\delta\chi_{\mathrm{av}} = \frac{\delta\chi_+ + \delta\chi_-}{2}, \quad (67a)$$

$$\delta\chi_{\mathrm{diff}} = \frac{\delta\chi_+ - \delta\chi_-}{2}. \quad (67b)$$

These variables can be written as:

$$\delta\chi_{\mathrm{av}} = \delta\chi_0 + \frac{p_\parallel - y\sqrt{p/3}\cos\left[\frac{\arg(G)}{3}\right]}{\delta\mu}$$

$$= \delta\chi_0 + \frac{p_\parallel^2 \sin^2\left[\frac{\arg(G)}{3}\right] - (2p_\perp/3)\cos^2\left[\frac{\arg(G)}{3}\right]}{\delta\mu\left(p_\parallel + y\sqrt{p/3}\cos\left[\frac{\arg(G)}{3}\right]\right)}, \quad (68a)$$

$$\delta\chi_{\mathrm{diff}} = \frac{y}{\delta\mu}\sqrt{p}\sin\left[\frac{\arg(G)}{3}\right], \quad (68b)$$

where in the second line of Eq. (68a) we have written $\delta\chi_{\mathrm{av}}$ in a way that avoids large numerical cancellations that can happen when $p_\parallel \gg |p_\perp|$.

To go from the non-inertial precession frame, where the solution of Eq. (47) was found, to the inertial frame, we perform a set of rotations described by the three Euler angles ϕ_z, θ_L and ζ also introduced in Eq. (5). The Euler angles can be computed as

$$\mathcal{D}\phi_z = \frac{1}{\sin^2\theta_L}\left(\mathcal{D}\hat{\boldsymbol{L}}\right)\cdot\left(\hat{\boldsymbol{J}}\times\hat{\boldsymbol{L}}\right), \quad (69a)$$

$$\cos\theta_L = \hat{\boldsymbol{J}}\cdot\hat{\boldsymbol{L}} = \frac{1}{2J}\left(2L + \chi_{\mathrm{eff}} + \delta\mu\delta\chi\right), \quad (69b)$$

$$\mathcal{D}\zeta = -\cos\theta_L\mathcal{D}\phi_z, \quad (69c)$$

where the final equation corresponds to the minimal rotation condition [88, 104]. We can compute Eq. (69a) by substituting all the angular momenta in terms of the solution of Eq. (66), such that

$$\mathcal{D}\phi_z = \frac{Jy^6}{2} + \frac{\mathcal{D}\psi_{\mathrm{p}}}{\nu\sqrt{Y_3 - Y_-}}\left[\frac{N_+}{D_+} + \frac{N_-}{D_-}\right], \quad (70a)$$

$$N_\pm = (J \pm L)(J + L \pm 2\nu\chi_{\mathrm{eff}}) - \delta\mu\left(S_1^2 - S_2^2\right), \quad (70b)$$

$$D_\pm = 2J(1 \pm \cos\theta_L) = 2(J \pm L) \pm \chi_{\mathrm{eff}} \pm \delta\mu\,\delta\chi$$

$$= B_\pm - C_\pm\left[1 - 2\mathrm{sn}^2(\psi_{\mathrm{p}}, m)\right], \quad (70c)$$

$$B_\pm = 2(J \pm L) \pm \chi_{\mathrm{eff}} \pm \delta\mu\,\delta\chi_{\mathrm{av}}, \quad (70d)$$

$$C_\pm = \pm\delta\mu\,\delta\chi_{\mathrm{diff}}. \quad (70e)$$

Eq. (70) can be analytically integrated. To do so, we first show how to integrate a general function in terms of our solution, i.e. we study how to integrate $g(\mathrm{sn}^2(\psi_{\mathrm{p}}(t), m))$ in

$$G(t_0, t_f) = \int_{t_0}^{t_f} g(\mathrm{sn}^2(\psi_{\mathrm{p}}(t), m))\mathrm{d}t,$$

$$= \int_{\psi_{\mathrm{p}}(t_0)}^{\psi_{\mathrm{p}}(t_f)} g(\mathrm{sn}^2(\psi_{\mathrm{p}}, m))\frac{\mathrm{d}t}{\mathrm{d}\psi_{\mathrm{p}}}\mathrm{d}\psi_{\mathrm{p}}. \quad (71)$$

When ignoring radiation reaction, the derivative $\mathrm{d}\psi_{\mathrm{p}}/\mathrm{d}t$ is a constant that can be taken outside of the integral. Furthermore, we can write the integral in terms of the Jacobi amplitude $\varphi = \mathrm{am}(\psi_{\mathrm{p}}; m)$, i.e.

$$\psi_{\mathrm{p}} = \int_0^\varphi \frac{\mathrm{d}\theta}{\sqrt{1 - m\sin^2\theta}} \rightarrow \mathrm{d}\psi_{\mathrm{p}} = \frac{\mathrm{d}\varphi}{\sqrt{1 - m\sin^2\varphi}}, \quad (72)$$

simplifying the integral of Eq. (71) as

$$G(t_0, t_f) = \frac{1}{d\psi_{\rm p}/dt} \int_{\varphi(t_0)}^{\varphi(t_f)} \frac{g(\sin\varphi)}{\sqrt{1 - m\sin^2\varphi}} d\varphi\,. \quad (73)$$

Also, we define the precession average of a function, as the average of the function over one precession cycle, i.e.

$$\langle g\rangle = \frac{1}{T_{\rm p}} G(t_0, t_0 + T_{\rm p})\,, \quad (74)$$

where $T_{\rm p}$ is the precession period, given by

$$T_{\rm p} = \frac{2K(m)}{d\psi_{\rm p}/dt}\,, \quad (75)$$

and $K(m)$ is the Jacobi complete elliptic integral of the first kind. Therefore, the precession average of any function can be computed as

$$\langle g\rangle = \frac{1}{2K(m)} \int_{-\pi/2}^{\pi/2} \frac{g(\sin\varphi)}{\sqrt{1 - m\sin^2\varphi}} d\varphi \quad (76)$$

With these equations, we can integrate $\mathcal{D}\phi_z$ in Eq. (70) analytically, separating the result in a secular part $\phi_{z,0}$ and periodic part $\delta\phi_z$, i.e.

$$\phi_z = \phi_{z,0} + \delta\phi_z, \quad (77a)$$

$$\mathcal{D}\phi_{z,0} = \langle \mathcal{D}\phi_z\rangle$$
$$= \frac{Jy^6}{2} + \frac{3(1 - y\chi_{\rm eff})y^6}{4\nu K(m)}\{P_+ + P_-\}, \quad (77b)$$

$$\delta\phi_z = \int_{t_0}^{t_0+\delta t} \mathcal{D}\phi_z - \langle \mathcal{D}\phi_z\rangle \; dt$$
$$= \frac{1}{\nu\sqrt{Y_3 - Y_-}}\{\delta P_+(\hat{\psi}_{\rm p}) + \delta P_-(\hat{\psi}_{\rm p})\}, \quad (77c)$$

where we have defined

$$P_\pm = \frac{N_\pm}{B_\pm - C_\pm}\Pi\left(\frac{-2C_\pm}{B_\pm - C_\pm}, m\right), \quad (78a)$$

$$\delta P_\pm(\hat{\psi}_{\rm p}) = \frac{N_\pm}{B_\pm - C_\pm}\left\{\Pi\left[\frac{-2C_+}{B_+ - C_+}; {\rm am}(\hat{\psi}_{\rm p}; m); m\right]\right.$$
$$\left. - \frac{\Pi\left(\frac{-2C_+}{B_+ - C_+}, m\right)}{K(m)}\hat{\psi}_{\rm p}\right\}, \quad (78b)$$

where $\Pi(n, m)$ is the complete elliptic integral of the third kind and $\Pi(n; \phi; m)$ is the incomplete elliptic integral of the third kind. t_0 represents the start of a precession cycle and $\delta t \in (0, T_{\rm p}]$ tracks the time within the precession cycle. Consequently, the variable $\hat{\psi}_{\rm p}$ tracks the

phase within the precession cycle and satisfies the following conditions

$$\psi_{\rm p} - \hat{\psi}_{\rm p} = 2nK(m), \text{ for some } n \in \mathbb{Z}\,, \quad (79a)$$
$$-K(m) < \hat{\psi}_{\rm p} \le K(m)\,. \quad (79b)$$

We can perform the same steps for the Euler angle ζ, writing Eq. (69c) in terms of $\delta\chi$ and integrating it analytically, separating the secular part ζ_0 from the periodic part $\delta\zeta$. Doing this we obtain:

$$\zeta = \zeta_0 + \delta\zeta, \quad (80a)$$
$$\mathcal{D}\zeta_0 = -\frac{(2L + \chi_{\rm eff} + \delta\mu\langle\delta\chi\rangle)y^6}{4}$$
$$- \frac{3(L + \nu\chi_{\rm eff})(1 - y\chi_{\rm eff})y^6}{2\nu}$$
$$+ \frac{3(1 - y\chi_{\rm eff})y^6}{4\nu K(m)}\{P_+ - P_-\}, \quad (80b)$$
$$\delta\zeta = \frac{y\sqrt{Y_3 - Y_-}}{3(1 - y\chi_{\rm eff})}\left\{E\left[{\rm am}(\hat{\psi}_{\rm p}; m); m\right] - \frac{E(m)}{K(m)}\hat{\psi}_{\rm p}\right\}$$
$$+ \frac{1}{\nu\sqrt{Y_3 - Y_-}}\{\delta P_+(\hat{\psi}_{\rm p}) - \delta P_-(\hat{\psi}_{\rm p})\}\,. \quad (80c)$$

where we have introduced the precession average of $\delta\chi$, given by

$$\langle\delta\chi\rangle = \delta\chi_{\rm av} - \frac{2\delta\chi_{\rm diff}}{m}\left[\frac{E(m)}{K(m)} - 1 + \frac{m}{2}\right], \quad (81)$$

and $E(m)$ is the complete elliptic integral of the second kind, while $E(\phi; m)$ is the incomplete elliptic integral of the second kind. Notice that for small m

$$\frac{2}{m}\left[\frac{E(m)}{K(m)} - 1 + \frac{m}{2}\right] = -\frac{m}{8} + O(m^2)\,, \quad (82)$$

and this term vanishes in the $m \to 0$ limit. In Eq. (78) we observe that we can have indeterminations in $P_\pm$ and $\delta P_\pm$, which appear in the secular and periodic parts of both ϕ_z (Eq. (77)) and ζ (Eq. (80)). These indeterminations happen under two conditions. First, when $B_+ - C_+ = 0$, where one can show $N_+ = 0$ and there is a 0/0 indetermination. Second, when $B_- + C_- = 0$, $\Pi(-2C_-/(B_- - C_-), m)$ diverges, and one can show $N_- = 0$, leading to a $0 \times \infty$ indetermination. Both scenarios happen because we have $D_\pm = 0$ at some point in the precessional cycle. From Eq. (70c), this occurs when the total and orbital angular momenta, J and L, get aligned ($\cos\theta_L = \pm 1$). This alignment corresponds to a Gimbal lock, which makes the Euler angles ϕ_z and ζ interdependent. To prevent these indeterminations, which would result in computational errors, we impose a minimum value of $D_\pm$, ensuring $D_\pm \ge \epsilon_D$. From Eq. (70c) this corresponds to imposing the constraint

$$B_\pm \mp C_\pm = B_\pm - \delta\mu\delta\chi_{\rm diff} \geq \epsilon_D \,. \qquad (83)$$

To implement this constraint in the code, we choose to update $B_\pm$ as

$$B_\pm \leftarrow \max\left(B_\pm, \delta\mu\delta\chi_{\rm diff} + \epsilon_D\right) \,, \qquad (84)$$

keeping the values of the rest of the variables in Eq. (78) constant. This regularization avoids singularities and indeterminations by effectively turning off precession when the total and orbital angular momenta align during the precessional cycle.

IV. ADDITION OF RADIATION REACTION EFFECTS

In Sec. II and Sec. III we have explored the system ignoring RR, i.e. ignoring how the binary evolves due to the emission of gravitational waves. Taking RR into account, the PN parameter y of Eq. (42b) will increase as the system becomes more compact, while the eccentricity e will decrease, as the system circularizes, reaching a residual eccentricity induced by spin [71, 72]

$$e_{\min}^2 = \frac{5y^4}{304} \left\| \boldsymbol{s}_{1\perp} - \boldsymbol{s}_{2\perp} \right\|^2 \,. \qquad (85)$$

The post-Newtonian evolution equations for the PN parameter y and the squared eccentricity e^2, the mean orbital phase λ and the argument of periastron $\delta\lambda$ can be expressed in the following way:

$$\mathcal{D}y = \nu y^9 \sum_{n \geq 0} a_n\left(y, e^2, \hat{\boldsymbol{L}}, \boldsymbol{s}_1, \boldsymbol{s}_2\right) y^n \,, \qquad (86a)$$

$$\mathcal{D}e^2 = -\nu y^8 \sum_{n \geq 0} b_n\left(y, e^2, \hat{\boldsymbol{L}}, \boldsymbol{s}_1, \boldsymbol{s}_2\right) y^n \,, \qquad (86b)$$

$$\mathcal{D}\lambda = y^3 \,, \qquad (86c)$$

$$\mathcal{D}\delta\lambda = \frac{ky^3}{1+k}, \quad k = y^2 \sum_{n \geq 0} k_n\left(y, e^2, \hat{\boldsymbol{L}}, \boldsymbol{s}_1, \boldsymbol{s}_2\right) y^n \,, \qquad (86d)$$

where k is the periastron advance of Eq. (2). The coefficients a_n, b_n and k_n are obtained from Ref. [72] to 3PN order in the non-spinning part and 2PN in the fully spinning part. We correct some errors in the 2PN and 3PN non-spinning instantaneous terms pointed out in Ref. [114] associated with an incorrect transformation from ADM to harmonic coordinates. We also fix a typo in the coefficient multiplying $(\hat{\boldsymbol{L}} \cdot \boldsymbol{s}_2)^2$ of b_2, where an 111/4 should be replaced by an 111/2 [53]. As it is well known in the literature [115], detectors are highly sensitive to the phase of the binary, and describing it at

2PN can induce strong biases in the recovered parameters. To alleviate this, we add the state-of-the-art 2.5PN and 3PN spin-spin and spin-orbit corrections for aligned-spin eccentric binaries derived in Ref. [53]. The explicit expressions for the evolution equations used can be found in appendix B.

Since no analytical solution is known for the differential equations of Eq. (86), we have to numerically solve them using, for example, Runge-Kutta methods [107, 116]. However, we observe that the PN coefficients depend not only on y and e^2, but also on the angular momenta $\hat{\boldsymbol{L}}, \boldsymbol{s}_1, \boldsymbol{s}_2$, which vary on the SP timescale. Since $\mathcal{D}\psi_{\rm p}, \mathcal{D}\phi_z, \mathcal{D}\zeta \sim O(y^5)$, while $\mathcal{D}\log(y), \mathcal{D}e^2 \sim y^8$, the angular momenta vary much more rapidly than y and e^2. That is, the SP time-scale is much shorter than the RR time-scale. To avoid having to integrate Eqs. (86) on the shorter (and thus more computationally expensive) SP time-scale, we replace the quantities in Eq. (86) that depend on the SP time-scale by their average over one precession cycle, which can analytically be computed with the solution of Sec. III. These averages vary on the RR time-scale, and the differential equations become numerically cheaper to integrate.

A. Spin couplings averaging

The 1.5PN and 2.5PN spin-orbit couplings of App. B can be written in terms of $\chi_{\rm eff}$ and $\delta\chi$. Since $\chi_{\rm eff}$ is constant, we only have to compute $\langle\delta\chi\rangle$, which was already done in Eq. (81). Meanwhile, the 2PN spin-spin couplings can be expressed as linear combinations of

$$\sigma_i^{(1)} = \boldsymbol{s}_i^2, \qquad (87a)$$

$$\sigma_i^{(2)} = \left(\hat{\boldsymbol{L}} \cdot \boldsymbol{s}_i\right)^2, \qquad (87b)$$

$$\sigma_i^{(3)} = \left|\hat{\boldsymbol{L}} \times \boldsymbol{s}_i\right|^2 \cos 2\psi_i, \qquad (87c)$$

where $i \in \{0, 1, 2\}$, $\boldsymbol{s}_0 = \boldsymbol{s}_1 + \boldsymbol{s}_2$ and ψ_i denotes the angle subtended by the periastron line and the projection of $\boldsymbol{s}_i$ onto the orbital plane. We have that $\sigma_{1,2}^{(1)} = s_{1,2}^2$ and $\sigma_0^{(2)} = \chi_{\rm eff}^2$ are conserved, and, as was found in Ref. [73], we have that

$$\left\langle \sigma_i^{(3)} \right\rangle = 0 \quad \text{for } i = \{0, 1, 2\} \,. \qquad (88)$$

The precession average for $\sigma_0^{(1)}$ can be computed in terms of our solution as

$$\left\langle \sigma_0^{(1)} \right\rangle = \left\langle (\boldsymbol{s}_1 + \boldsymbol{s}_2)^2 \right\rangle$$
$$= \left\langle \frac{J^2 - L^2 - \delta\mu\left(\mu_1 s_1^2 - \mu_2 s_2^2\right) - L\left(\chi_{\rm eff} + \delta\mu\delta\chi\right)}{\nu} \right\rangle$$

$$= \chi_{\text{eff}}^2 + s_{1\perp,0}^2 + s_{2\perp,0}^2 + \Delta_{J^2}^2 + \delta\mu\left(\frac{\delta\chi_0 - \langle\delta\chi\rangle}{y}\right). \tag{89}$$

Finally, the square of the component of the spins aligned with the orbital angular momentum $\sigma_{1,2}^{(2)}$ can be written as

$$\left\langle\sigma_{1,2}^{(2)}\right\rangle = \left\langle\left(\hat{\boldsymbol{L}}\cdot\boldsymbol{s}_{1,2}\right)^2\right\rangle = \left\langle\left(\frac{\chi_{\text{eff}}\pm\delta\chi}{2}\right)^2\right\rangle$$

$$= \frac{\chi_{\text{eff}}^2 \pm 2\chi_{\text{eff}}\langle\delta\chi\rangle + \langle\delta\chi^2\rangle}{4}, \tag{90}$$

where we have used that χ_{eff} is conserved, $\langle\delta\chi\rangle$ can be computed from Eq. (81) and we can compute $\langle\delta\chi^2\rangle$ using Eqs. (66,76), obtaining

$$\langle\delta\chi^2\rangle = \langle\delta\chi\rangle^2 + \left(\frac{1}{2} - F_\sigma(m)\right)\delta\chi_{\text{diff}}^2, \tag{91}$$

where we have defined the function

$$F_\sigma(m) = \frac{4}{m^2}\left[\frac{E(m)^2}{K(m)^2} + \frac{2E(m)}{3K(m)}(m-2) + \frac{m^2}{8} - \frac{m}{3} + \frac{1}{3}\right]. \tag{92}$$

We note that in Eq. (92) there is a difference in the sign of F_σ with respect to Ref. [73] due to a typo therein. For small values of m (i.e. $m \ll 1$) we have

$$F_\sigma(m) = \frac{m^2}{256} + O(m^3) \tag{93}$$

and this term vanishes in the $m \to 0$ limit. In App. B 3 we show how the fully spinning spin-spin coefficients are simplified when using the expressions for $\left\langle\sigma_i^{(j)}\right\rangle$ derived in this section.

B. Total angular momentum

Through radiation reaction, the total angular momentum varies due to the radiation of orbital angular momentum, i.e. [73]

$$\mathcal{D}\boldsymbol{J} = (\mathcal{D}L)\hat{\boldsymbol{L}} = \mathcal{D}\left(\frac{\nu}{y}\right)\hat{\boldsymbol{L}} = -\frac{\nu\mathcal{D}y}{y^2}\hat{\boldsymbol{L}}. \tag{94}$$

We can multiply both sides of Eq. (94) by $\boldsymbol{J}$ and use that $\boldsymbol{J}\cdot\hat{\boldsymbol{L}} = J\cos\theta_L$ (Eq. (69b)) to write

$$\mathcal{D}J^2 = -\frac{L\mathcal{D}y}{y}\left(2L + \chi_{\text{eff}} + \delta\mu\delta\chi\right). \tag{95}$$

Using Eq. (50) to write J^2 in terms of Δ_{J^2} (Eq. (50)) we can further simplify this equation as

$$\mathcal{D}\Delta_{J^2} = \delta\mu\frac{\delta\chi_0 - \delta\chi}{y^2}\mathcal{D}y, \tag{96}$$

where $\delta\chi$ varies in the SP time-scale, following Eq. (66). To avoid the computationally costly integration of Eq. (96) on the SP time-scale, we separate in a similar way as in Eq. (77) the secular and periodic parts of Δ_{J^2}, i.e.

$$\Delta_{J^2} = \Delta_{J^2,0} + \delta\Delta_{J^2}, \tag{97a}$$

$$\frac{\mathcal{D}\Delta_{J^2,0}}{\mathcal{D}y} = \delta\mu\frac{\delta\chi_0 - \langle\delta\chi\rangle}{y^2}, \tag{97b}$$

$$\delta\Delta_{J^2} = \frac{4\nu\sqrt{Y_3 - Y_-}}{3(1 - y\chi_{\text{eff}})}y^2\left[\left(\frac{32}{5} + \frac{28}{5}e^2\right) + O(y)\right]$$

$$\times\left\{E[\text{am}(\hat{\psi}_{\text{p}}; m); m] - \frac{E(m)}{K(m)}\hat{\psi}_{\text{p}}\right\}. \tag{97c}$$

Analyzing Eq. (97b), we have that $\mathcal{D}\Delta_{J^2,0}/\mathcal{D}y \sim O(y^0)$. Therefore, $\Delta_{J^2,0}$ is slowly varying through RR and thus simple to numerically integrate. Furthermore, since from the initial conditions $\Delta_{J^2,0}(t_0) \sim O(y^0)$ (Eq. (52)), we have that $\Delta_{J^2,0} \sim O(y^0)$ all throughout the evolution. On the other hand, given that $\sqrt{Y_3 - Y_-} \sim O(y^{-1})$ and that the term in brackets containing the elliptic integrals is $\mathcal{O}(m) \sim O(y^2)$, the periodic part $\delta\Delta_{J^2} \sim O(y^3)$ is much smaller than the secular part $\Delta_{J^2,0}$.

Using that $\delta\Delta_{J^2} \approx 2J_0\delta J/\nu$ to compare Eq. (97c) with the corresponding equations in Ref. [73], we observe that there is a factor of 2 missing in Ref. [73] due to a typo therein.

C. Effects of the evolution of the elliptic parameter

Through radiation reaction the parameter m of Eq. (65b) evolves with time. Since the period of the spin-precession solution (Eq. (66)) is $2K(m)$ in ψ_{p}, the value of ψ_{p} accumulated at different times corresponds to a different number of precession cycles. Because of this, when including RR, Eq. (79) is not valid to find the phase within the precession cycle $\hat{\psi}_{\text{p}}$. To solve this, we define a new phase $\bar{\psi}_p$ that is proportional to the accumulated number of cycles. In particular,

$$\mathcal{D}\bar{\psi}_p = \frac{\pi}{2K(m)}\mathcal{D}\psi_{\text{p}}. \tag{98}$$

From this, we can recover the correct phase of the Jacobi elliptic functions via

$$\hat{\psi}_{\text{p}}(t) = \frac{2K[m(t)]}{\pi}\hat{\bar{\psi}}_p(t), \tag{99}$$

where the angle $\hat{\bar{\psi}}_p$ satisfies the following conditions

$$\bar{\psi}_p - \hat{\bar{\psi}}_p = n\pi, \text{ for some } n \in \mathbb{Z}, \quad (100a)$$

$$-\pi < \hat{\bar{\psi}}_p \le \pi, \quad (100b)$$

and therefore tracks the phase within the precession cycle also when including RR.

V. FOURIER TRANSFORM APPROXIMATION

In the previous sections we laid out the foundations to obtain the time-domain GW polarizations $h_{+,\times}(t)$ emitted by a binary that includes the effects of spin-precession and orbital eccentricity. However, for data-analysis applications such as parameter estimation (PE) or searches, we usually need the frequency-domain polarizations $\tilde{h}_{+,\times}(f)$, obtained with the Fourier transform

$$\tilde{h}(f) = \int_{-\infty}^{\infty} \mathrm{d}t\, h(t)\, \mathrm{e}^{2\pi \mathrm{i} f t}, \quad (101)$$

where for notational simplicity we have dropped the subscripts $+, \times$. In principle, the Fourier Transform of Eq. (101) can be computed numerically by, for example, using the Fast Fourier Transform (FFT). In practice however, using the FFT to compute $\tilde{h}(f)$ is computationally costly and, unless the strain data $h(t)$ is properly conditioned [117–119], it can introduce its own sources of error. Therefore we seek to approximate the frequency-domain strain analytically.

Our starting point is the expression of Eq. (18) for the time-domain GW polarizations $h_{+,\times}(t)$. For notational simplicity we again drop all subscripts and superscripts, i.e.

$$h(t) = A(t)\, \mathrm{e}^{-\mathrm{i}\phi(t)}, \quad (102)$$

where here $A(t) \equiv \mathcal{A}_{l,m,n}^{+,\times}(t)$ is an amplitude that varies in the spin-precession time scale (i.e. $\dot{A}/A \sim \mathcal{O}\left(y^5\right)$) and $\phi(t) \equiv n\lambda(t) + (m-n)\delta\lambda(t)$ represents the phase of the binary, with $\dot{\lambda} \sim \mathcal{O}\left(y^3\right)$ and $\dot{\delta\lambda} \sim \mathcal{O}\left(y^5\right)$. For non-precessing systems one usually neglects the very slow evolution of $A(t)$, and computes the Fourier transform of Eq. (102) by using the Stationary Phase Approximation (SPA) [120–122]. To compute the SPA, we first find the stationary time t_0, as

$$2\pi f = \dot{\phi}(t_0), \quad (103)$$

and Taylor expand the phase around this time

$$\phi(t) \approx \phi(t_0) + (t - t_0)\dot{\phi}(t_0) + \frac{1}{2}(t - t_0)^2 \ddot{\phi}(t_0),$$

$$= \phi(t_0) + 2\pi f(t - t_0) + \frac{1}{2}\frac{(t - t_0)^2}{T_0^2}, \quad (104)$$

where we have defined

$$T_0 = \frac{1}{\sqrt{\left|\ddot{\phi}(t_0)\right|}}. \quad (105)$$

Substituting this approximation in Eq. (101), neglecting the time-dependence of the amplitude (i.e. $A(t) \approx A(t_0)$), and analytically computing the Fresnel integral that appears, we obtain the usual SPA approximation

$$\tilde{h}_{\mathrm{SPA}}(f) = \sqrt{2\pi}T_0 A(t_0)\, \mathrm{e}^{\mathrm{i}(2\pi f t_0 - \phi(t_0) - \pi/4)}. \quad (106)$$

However, in Ref. [71] it was noted that neglecting the time-dependence of the amplitude is not a good approximation for precessing systems and they introduced a correction to the usual SPA which they named the Shifted Uniform Asymptotics (SUA) method, showing its improved performance over the SPA. In the SUA, Eq. (106) becomes

$$\tilde{h}_{\mathrm{SUA}}(f) = \sqrt{2\pi}T_0 A^{\mathrm{corr}}(t_0)\, \mathrm{e}^{\mathrm{i}(2\pi f t_0 - \phi(t_0) - \pi/4)}, \quad (107)$$

where the only difference is that we have made $A(t_0) \to A^{\mathrm{corr}}(t_0)$, defined as

$$A^{\mathrm{corr}}(t_0) = \sum_{k=-k_{\mathrm{max}}}^{k_{\mathrm{max}}} a_{k,k_{\mathrm{max}}} A(t_0 + kT_0), \quad (108)$$

where the constants $a_{k,k_{\mathrm{max}}}$ are found solving the following linear system of equations:

$$\frac{1}{2}a_{0,k_{\mathrm{max}}} + \sum_{k=1}^{k_{\mathrm{max}}} a_{k,k_{\mathrm{max}}} = \frac{1}{2} \quad , p = 0, \quad (109a)$$

$$\sum_{k=1}^{k_{\mathrm{max}}} \frac{(\mathrm{i}\,k^2)^p}{(2p-1)!!} a_{k,k_{\mathrm{max}}} = \frac{1}{2} \quad , 1 \le p \le k_{\mathrm{max}}, \quad (109b)$$

$$a_{-k,k_{\mathrm{max}}} = a_{k,k_{\mathrm{max}}} \quad (109c)$$

This differs from the linear system of Ref. [84] because in order to simplify Eq. (108), we have substituted $\frac{1}{2}a_{k,k_{\mathrm{max}}} \to a_{k,k_{\mathrm{max}}}$ for $|k| \ge 1$, and we have defined $a_{-k,k_{\mathrm{max}}} = a_{k,k_{\mathrm{max}}}$. This simplification was also implicitly done in Refs. [72–74], but all of them have a typo where the factor of $1/2$ in the right hand side of Eq. (109b) is missing.

VI. WAVEFORM IMPLEMENTATION

In this section we aim to bring together all the previous results of the paper to compute the frequency domain waveform, detailing the actual numerical implementation used in our waveform approximant.

A. Solving the dynamics

As previously discussed, to describe the dynamics of our eccentric-precessing binary system, we have used the quasi-Keplerian approximation to describe the eccentric orbits and have described with the MSA approximation how these orbits precess due to spin effects. Finally, we take into account the effect of radiation reaction as a slow perturbation of the quasi-Keplerian and MSA parameters. This leads to the following equations of motion that need to be integrated

$$\mathcal{D}y = y^9 \sum_{n \geq 0} \langle a_n \rangle y^n, \tag{110a}$$

$$\mathcal{D}e^2 = y^8 \sum_{n \geq 0} \langle b_n \rangle y^n, \tag{110b}$$

$$\mathcal{D}\lambda = y^3, \tag{110c}$$

$$\mathcal{D}\delta\lambda = \frac{ky^3}{1+k}, \quad k = y^2 \sum_{n \geq 0} \langle k_n \rangle y^n, \tag{110d}$$

$$\mathcal{D}\Delta_{J^2,0} = \delta\mu \frac{\delta\chi_0 - \langle \delta\chi \rangle}{y^2} \mathcal{D}y, \tag{110e}$$

$$\mathcal{D}\bar{\psi}_p = \frac{3(1 - y\chi_{\mathrm{eff}})y^6}{4} \frac{\pi}{2K(m)} \sqrt{Y_3 - Y_-}, \tag{110f}$$

$$\mathcal{D}\phi_{z,0} = \frac{Jy^6}{2} + \frac{3(1 - y\chi_{\mathrm{eff}})y^6}{4\nu K(m)} (P_+ + P_-), \tag{110g}$$

$$\begin{aligned} \mathcal{D}\zeta_0 = &-\frac{(2L + \chi_{\mathrm{eff}} + \delta\mu \langle \delta\chi \rangle)y^6}{4} \\ &- \frac{3(L + \nu\chi_{\mathrm{eff}})(1 - y\chi_{\mathrm{eff}})y^6}{2\nu} \\ &+ \frac{3(1 - y\chi_{\mathrm{eff}})y^6}{4\nu K(m)} (P_+ - P_-), \end{aligned} \tag{110h}$$

where all the quantities have been previously defined, and to avoid the solution to depend on the spin-precession time-scale we neglect the contribution of $\delta\Delta_{J^2}$ in all of the equations. Given some initial conditions, e.g. as will be described in Sec. VI B, the system of coupled ordinary differential equations of Eq. (110) can be numerically integrated. To do this we write it as

$$\frac{\mathrm{d}\mathcal{V}}{\mathrm{d}t} = \boldsymbol{F}(\mathcal{V}), \tag{111}$$

where we have defined

$$\mathcal{V} \equiv \{y, e^2, \lambda, \delta\lambda, \Delta_{J^2,0}, \bar{\psi}_p, \phi_{z,0}, \zeta_0\}. \tag{112}$$

We integrate Eq. (111) using adaptive Runge-Kutta methods, which automatically estimate the time-steps needed to keep the error under a specified tolerance. In particular, we use an explicit Runge-Kutta of order 5(4) [123], where the error is controlled assuming accuracy of the fourth-order method, but steps are taken using the fifth-order accurate formula. The result of this 5(4) Runge-Kutta can be expressed as a sequence of times $\{t_j\}$ between each of which we construct a quartic interpolation polynomial of $\mathcal{V}$ [124], i.e.

$$\mathcal{V}_i(t) = \mathcal{V}_i(t_j) + \sum_{k=1}^{4} Q_{i,j,k}(t - t_j)^k, \quad t_j \leq t \leq t_{j+1}. \tag{113}$$

Writing the solution as in Eq. (113) will prove useful, as it allows for easy computation of the derivatives of $\mathcal{V}$, which are for example required when using the SPA (or SUA).

B. Initial conditions

As previously mentioned, to integrate the equations of motion of Eq. (110) we need to give initial conditions for all of the components of $\mathcal{V}$. However, many of these variables used in the model have a difficult astrophysical interpretation. Therefore, we initialize our system using the more physically relevant variables specified in table I and then convert them to the variables of our model.

Some of the parameters in table I are directly used by our model, such as the component masses $m_{1,2}$, the component quadrupole parameters $q_{1,2}$, the initial eccentricity e_0, the luminosity distance d_L and the initial mean orbital phase λ_0. Others can be easily related, such as the initial mean anomaly ℓ_0, with the initial argument of periastron $\delta\lambda_0$ using Eq. (3), i.e.

$$\delta\lambda_0 = \lambda_0 - \ell_0, \tag{114}$$

Or the initial $l = m = 2$ quasi-circular GW frequency $f_0^{\mathrm{GW},22} = 2f_0^{\mathrm{orb}} = \omega/\pi$ with the initial PN parameter y_0 using Eq. (42b), i.e.

$$y_0 = \frac{\left(\pi M f_0^{\mathrm{GW},22}\right)^{1/3}}{\sqrt{1 - e_0^2}}. \tag{115}$$

To apply the adaptive Runge-Kutta we also need to specify a maximum time t_f up to which we integrate the equations of motion of Eq. (110). In practice however, it is more convenient to specify the endpoint of integration in terms of a maximum frequency $f_f^{\mathrm{GW},22}$, usually related to the frequency up to which we are analyzing some data, or the frequency up to which we trust the PN approximation used in the inspiral. In this last case, for late times, we could hybridize with a different approximant that is better suited for the merger-ringdown stages of the binary, such as a phenomenological model [125], an effective one body model [63, 126] or a numerical relativity (NR) surrogate model [66, 127]. In terms of the PN parameter y, we stop the integration when

Parameter	Description
m_1	Mass of primary object
m_2	Mass of secondary object
q_1	quadrupole parameter of primary object ($q_1 = 1$ for a black hole)
q_2	quadrupole parameter of secondary object ($q_2 = 1$ for a black hole)
e_0	Initial orbital time-eccentricity in ADM coordinates
$\chi_{1x,0}, \chi_{1y,0}, \chi_{1z,0}$	Initial dimensionless spin vector of primary object ($\boldsymbol{\chi}_1 = \boldsymbol{s}_1/\mu_1 = \boldsymbol{S}_1/\mu_1^2$)
$\chi_{2x,0}, \chi_{2y,0}, \chi_{2z,0}$	Initial dimensionless spin vector of secondary object ($\boldsymbol{\chi}_2 = \boldsymbol{s}_2/\mu_2 = \boldsymbol{S}_2/\mu_2^2$)
ι_0	Initial inclination, i.e. the angle between initial orbital angular momentum $\hat{\boldsymbol{L}}_0$ and vector from binary to observer $\hat{\boldsymbol{N}}$
d_L	Initial luminosity distance from binary to observer
λ_0	Initial mean orbital phase
ℓ_0	Initial mean anomaly
$f_0^{\mathrm{GW},22}$	Initial frequency of the $l = m = 2$ quasi-circular GW mode. It is twice the initial orbital frequency ($f_0^{\mathrm{GW},22} = 2f_0^{\mathrm{orb}}$)
$f_f^{\mathrm{GW},22}$	Final frequency of the $l = m = 2$ quasi-circular GW mode.

TABLE I: Table listing the parameters required to evaluate the model together with a short description for each.

$$y = y_f = \frac{\left(\pi M f_f^{\mathrm{GW},22}\right)^{1/3}}{\sqrt{1 - e^2(t_f)}} \,. \qquad (116)$$

To impose this condition in an adaptive Runge-Kutta, every time a new time-step t_{j+1} is proposed, we use the interpolation polynomial of Eq. (112) to check if $y(t) = y_f$ is satisfied at any point of the interval $t \in (t_j, t_{j+1}]$. If it is, we terminate the Runge-Kutta and define the final time as the first solution $y(t_f) = y_f$. In the quasi-circular case, we stop trusting the PN approximation for frequencies above that of the Minimum Energy Circular Orbit (MECO) [125, 128]. This point is hard to estimate, as it requires finding where the PN energy $E_{\mathrm{PN}}(f)$ has its first minimum. Therefore, a stopping point that is more commonly chosen is the frequency of the Innermost Stable Circular Orbit (ISCO) [129], above which circular orbits of test particles around Schwarzschild are unstable, plunging to the central black hole. In terms of the PN parameter, this happens at

$$y_{\mathrm{ISCO}} = 6^{-1/2} \,. \qquad (117)$$

As is usually done in PN approximants, the time is chosen such that $t = 0$ corresponds to the coalescence time [113]. In the eccentric case, this time is hard to analytically compute to high PN orders. Therefore, for simplicity we use the 0PN time to coalescence τ_c, that can computed as described in appendix C, where in Eq. (C5) we obtain

$$\tau_c(y,e) = \frac{5}{256} \frac{M}{\nu y^8} \frac{F(e)}{\sqrt{1 - e^2}} \,, \qquad (118)$$

with $F(e)$ being an $\mathcal{O}(1)$ function defined by Eq. (C6) and shown in Fig. 19. When we start the Runge-Kutta integration of the equations of motion, we set use Eq. (118) to set the initial time, i.e.

$$t_0 = -\tau_c(y_0, e_0) \,. \qquad (119)$$

However, as previously described, when the Runge-Kutta integration terminates, we obtain a value of t_f such that $y(t_f) = y_f$, that will slightly deviate from $-\tau_c(y_f, e_f)$, given that we ignore PN corrections in our initial guess of the coalescence time. Therefore, after finishing the Runge-Kutta integration, we shift the time of the whole solution as

$$t \to t - t_f - \tau_c(y_f, e_f). \qquad (120)$$

Setting the initial conditions on the angular momenta and orientation of the binary requires more choices of conventions. Throughout our description of the problem we use three different reference frames [113]

- The N-frame: This is the inertial frame with respect to which the GW polarizations are measured. By definition it places the unit vector $\hat{\boldsymbol{N}}$ pointing from the binary to the observer in the $\hat{\boldsymbol{Z}}$ axis. To fix the remaining orientation of this frame, we choose it such that the initial orbital angular momentum $\boldsymbol{L}_0$ is on the $\hat{\boldsymbol{X}} - \hat{\boldsymbol{Z}}$ plane.

- The J-frame: This is the frame in which the binary motion is described. By definition, it places the total angular momentum $\boldsymbol{J}$ in the $\boldsymbol{z}$ axis. To fix the remaining orientation of this frame, we again choose the initial orbital angular momentum $\boldsymbol{L}_0$ to be on the $\hat{\boldsymbol{x}} - \hat{\boldsymbol{z}}$ plane. As seen in Eq. (94), the direction of $\boldsymbol{J}$ varies in the radiation reaction time-scale, making the J-frame non-inertial. However, in this work we are neglecting the evolution of $\hat{\boldsymbol{J}}$ (i.e. we are doing $\hat{\boldsymbol{J}}(t) = \hat{\boldsymbol{J}}_0$), and we therefore consider the J-frame to be inertial. While this is usually a very good approximation, it can fail in systems exhibiting strong nutational resonances or transitional precession [130].

- The L-frame: This is the non-inertial frame in which the effects of precession on the waveform are minimized [86, 88]. The Euler Angles $(\phi_z, \theta_L, \zeta)$ are defined such that they rotate the $\boldsymbol{L}$-frame to the $\boldsymbol{J}$-frame, i.e. for any vector $\boldsymbol{v}$

$$\begin{pmatrix} v_{x,J} \\ v_{y,J} \\ v_{z,J} \end{pmatrix}_J = \hat{R}_z(\phi_z)\hat{R}_y(\theta_L)\hat{R}_z(\zeta) \begin{pmatrix} v_{x',L} \\ v_{y',L} \\ v_{z',L} \end{pmatrix}_L \,, \qquad (121)$$

where $(\boldsymbol{v})_J$ and $(\boldsymbol{v})_L$ means that the vector is measured in the J-frame and L-frames respectively and $\hat{R}_{\hat{\boldsymbol{u}}}(\alpha)$ are the usual rotation matrices of an angle α around the rotation axis $\hat{\boldsymbol{u}}$.

The orientation of the binary is determined by the initial inclination ι_0, defined as the angle between the initial orbital angular momentum $\hat{\boldsymbol{L}}_0$ and the vector from binary to observer $\hat{\boldsymbol{N}}$, therefore

$$(\hat{\boldsymbol{L}}_0)_N = \begin{pmatrix} \cos\iota_0 \\ 0 \\ \sin\iota_0 \end{pmatrix}, \qquad (122)$$

As is usually done in GW modeling, the input spins are given in terms of the L-frame dimensionless spin vectors $\boldsymbol{\chi}_i = \boldsymbol{S}_i/\mu_i^2$ of the component objects, such that $|\chi_i| \leq 1$ for sub-extremal Kerr Black Holes. The spins are specified in Cartesian components such that $\chi_{iz,0}$ is the component parallel to the orbital angular momentum (i.e. $\chi_{iz,0} = \hat{\boldsymbol{L}}_0 \cdot \boldsymbol{\chi}_{i,0}$). With our conventions, the total angular momentum in the N-frame is given by

$$\begin{aligned} (\boldsymbol{J}_0)_N &= \hat{R}_y(\iota_0)(\boldsymbol{L}_0 + \boldsymbol{S}_{1,0} + \boldsymbol{S}_{2,0})_L \\ &= \begin{pmatrix} \cos\iota_0 & 0 & \sin\iota_0 \\ 0 & 1 & 0 \\ -\sin\iota_0 & 0 & \cos\iota_0 \end{pmatrix} \begin{pmatrix} S_{1x,0} + S_{2x,0} \\ S_{1y,0} + S_{2y,0} \\ \frac{\nu}{y} + S_{1z,0} + S_{2z,0} \end{pmatrix}. \end{aligned} \qquad (123)$$

If we define (θ_{JN}, ϕ_{JN}) as the spherical angles[1] of the unit vector pointing in the direction of the initial total angular momentum $\boldsymbol{J}_0$, we can bring this vector to the z axis applying $\hat{R}_y(-\theta_{JN})\hat{R}_z(-\phi_{JN})$. This almost corresponds to the rotation that transforms from the N to the J frames. We have to add the additional requirement that $(\hat{\boldsymbol{L}}_0)_J$ is in the $x-z$ plane of the J frame. To impose this we compute the spherical angles $(\theta_{LJN}, \phi_{LJN})$ of the unit vector $\hat{R}_y(-\theta_{JN})\hat{R}_z(-\phi_{JN})(\hat{\boldsymbol{L}}_0)_N$, and then, the rotation from the N frame to the J frame is given by

$$\hat{R}_{NJ} = \hat{R}_z(-\phi_{LJN})\hat{R}_y(-\theta_{JN})\hat{R}_z(-\phi_{JN}). \qquad (124)$$

Using this, we can define the angles $(\Theta_{\rm p}, \Phi_{\rm p})$ that were vaguely introduced in Eq. (4) as the spherical angles of the unit vector from the observer to the binary in the J frame, i.e. $(-\hat{\boldsymbol{N}})_J$. Therefore, $(\Theta_{\rm p}, \Phi_{\rm p})$ are defined by

$$\begin{pmatrix} \sin\Theta_{\rm p}\cos\Phi_{\rm p} \\ \sin\Theta_{\rm p}\cos\Phi_{\rm p} \\ \cos\Theta_{\rm p} \end{pmatrix} = \hat{R}_{NJ}\begin{pmatrix} 0 \\ 0 \\ -1 \end{pmatrix}. \qquad (125)$$

---

[1] We can express any unit vector using two spherical angles (θ, ϕ) as $\hat{\boldsymbol{v}} = (\sin\theta\cos\phi, \sin\theta\sin\phi, \cos\theta)$.

To integrate the equations of motion of Eq. (110), we also have to find the value of initial value of $\Delta_{J^2,0}$. To do this, we first compute the initial value of Δ_{J^2}, which is given by Eq. (51). To find the initial value of $\Delta_{J^2,0}$ we numerically solve for it using

$$\Delta_{J^2}(t_0) = \Delta_{J^2,0}(t_0) + \delta\Delta_{J^2}(t_0; \Delta_{J^2,0}(t_0)), \qquad (126)$$

where we have made explicit that $\delta\Delta_{J^2}$ (given by Eq. (97c)) is being evaluated assuming $\Delta_{J^2} = \Delta_{J^2,0}$, to be consistent with what is later done in the evolution equations. To evaluate $\delta\Delta_{J^2}(t_0)$ we also need the initial value of the precession phase $\psi_{\rm p,0}$, this can be computed for each value of $\Delta_{J^2,0}$ assumed by solving Eq. (66) using $\delta\chi(t_0) = \delta\chi_0$, i.e.

$$\psi_{\rm p,0} = \pm F\left(\frac{1}{2}\arccos\left(\frac{\delta\chi_{\rm av} - \delta\chi_0}{\delta\chi_{\rm diff}}\right); m_0\right), \qquad (127)$$

where $F(\phi; m)$ is the incomplete elliptic integral of the first kind. To choose the correct sign of $\psi_{\rm p,0}$ we look at the derivative of $\mathcal{D}\delta\chi$, which in terms of the MSA solution is given by

$$\mathcal{D}\delta\chi = 2\delta\chi_{\rm diff}\sin(2{\rm am}(\psi_{\rm p}; m))\mathcal{D}\psi_{\rm p}. \qquad (128)$$

Since $\mathcal{D}\psi_{\rm p} \geq 0$ and $\delta\chi_{\rm diff} \geq 0$, in order for Eq. (128) to have the same sign for $\mathcal{D}\delta\chi$ as Eq. (46), we have to choose

$$\text{sign}(\psi_{\rm p,0}) = \text{sign}\left(\left(\hat{\boldsymbol{L}} \times \boldsymbol{s}_1\right) \cdot \boldsymbol{s}_2\right). \qquad (129)$$

Finally, to integrate the equations of motion of Eq. (110) we are only missing the initial values of the average Euler angles $\phi_{z,0}$ and ζ_0. Given that $\hat{\boldsymbol{L}}_0$ is on the $x-z$ plane of the J-frame, the initial value of ϕ_z satisfies $\phi_z(t_0) = 0$, and thus

$$\phi_{z,0}(t_0) = -\delta\phi_z(t_0), \qquad (130)$$

which can be computed with Eq. (77c). A choice for the initial value of the Euler angle ζ corresponds to a choice of the initial L-frame with respect to which the input spins are measured. For simplicity, we set $\zeta(t_0) = 0$, i.e.

$$\zeta_0(t_0) = -\delta\zeta(t_0), \qquad (131)$$

which can be computed with Eq. (80c).

C. Computing the waveform

Using the initial conditions of Sec. VI B we first integrate the equations of motion of Eq. (110) using and adaptive Runge-Kutta of order 5(4). This gives us a grid of times $\{t_j\}_{j=0}^{N_{\rm RK}}$, between each of which all the dynamical variables are described by an interpolation polynomial of the form of Eq. (113).

The first thing we do is, for each segment $[t_j, t_{j+1}]$, find the Fourier modes that have to be included in the amplitudes given a user defined tolerance ϵ_N. This is found following the procedure described in Sec. II D, obtaining a set of Fourier modes with $\{(n_i, m_i)\}_{i=1}^{N_F}$ (Eq. (18)). Given that we are only considering the Newtonian amplitudes, m_i can only be 2, 0 or -2. Therefore, at each segment of the Runge-Kutta we have N_F modes, each having a GW phase

$$
\begin{aligned}
\phi_i(t) &= n_i\lambda(t) + (m_i - n_i)\delta\lambda(t) \\
&= \phi_i(t_j) + \sum_{k=1}^{4} Q_{\phi,i,j,k}(t - t_j)^k, \quad t_j \le t \le t_{j+1},
\end{aligned}
\tag{132}
$$

where we have defined

$$
\phi_i(t_j) = n_i\mathcal{V}_\lambda(t_j) + (m_i - n_i)\mathcal{V}_{\delta\lambda}(t_j), \tag{133a}
$$
$$
Q_{\phi,i,j,k} = n_i Q_{\lambda,j,k} + (m_i - n_i)Q_{\delta\lambda,j,k}. \tag{133b}
$$

Given an input frequency f, we then have to compute for each mode the corresponding stationary time t_i^{SPA} solving Eq. (103). Substituting Eq. (132) in Eq. (103), we have that t_i^{SPA} is the solution to

$$
\omega = \omega_i(t_j) + \sum_{k=1}^{3} Q_{\omega,i,j,k}(t_i^{\text{SPA}} - t_j)^k, \quad t_j \le t \le t_{j+1}.
\tag{134}
$$

where we have defined $\omega = 2\pi f$, $\omega_i(t_j) = Q_{\omega,i,j,1}$ and $Q_{\omega,i,j,k} = (1+k)Q_{\phi,i,j,1+k}$. In a Runge-Kutta, the time-steps are chosen such that the difference between the polynomial of Eq. (113) and the true solution, remains very small. In practice, this means that each time interval is by construction sufficiently short that the solution therein is smooth and the contribution of each term in the sum of Eq. (113) is much smaller than the previous. In this context, we can invert Eq. (134) using series reversion [105]

$$
\begin{aligned}
t_i^{\text{SPA}}(\omega) &= t_j + \sum_{k=1}^{N_{\text{sr}}} Q_{t,i,j,k}(\omega - \omega_i(t_j))^k, \\
&\text{with} \quad \omega_i(t_j) \le \omega \le \omega_i(t_{j+1}),
\end{aligned}
\tag{135}
$$

where a series reversion order of $N_j \ge 4$ is expected to give good results in our case, and the coefficients $Q_{t,i,j,k}$ are computed with usual series reversion tables [105]. The formulas used are explicitly shown in App. D.

Using Eq. (135) we can, for any input frequency, easily and efficiently compute the SPA time corresponding to each mode that contributes at that frequency. From Eq. (132), we can see that this effectively means that we neglect the modes with $n < 0$ and with $n =$

$0, m = \{0, -2\}$, as these have monotonously decreasing GW phases and negative frequencies, which means they have no stationary time. These negative frequency modes are needed to make the time-domain polarizations real, but can be neglected when computing the frequency-domain modes.

The SPA duration scale T_i^{SPA} can be very easily computed taking the second derivative of $\phi_i(t)$ (Eq. (132)) and substituting it in Eq. (105). With this, we can use Eq. (18) and the SUA approximation introduced in Sec. V, to compute the GW polarizations as

$$
\begin{aligned}
\tilde{h}_{+,\times}(f) &= \sum_i \sqrt{2\pi} T_i^{\text{SPA}} e^{i\left(2\pi f t_i^{\text{SPA}} - \phi(t_i^{\text{SPA}}) - \pi/4\right)} \\
&\times \sum_{k=-k_{\max}}^{k_{\max}} a_{k,k_{\max}} \mathcal{A}_{2,m_i,n_i}^{+,\times}\left(t_i^{\text{SPA}} + k T_i^{\text{SPA}}\right).
\end{aligned}
\tag{136}
$$

where we have made explicit that only $l = 2$ contributes, since we are using the Newtonian amplitudes, and the sum over i represents the sum over the Fourier modes that contribute at a given frequency.

The only piece missing now is how to compute the amplitudes $\mathcal{A}_{2,m,n}^{+,\times}(t)$, defined in Eq. (19). Doing this is straightforward, with the solution of the Runge-Kutta (Eq. (113)) we can obtain the dynamical variables of the binary at each amplitude evaluation time t. With these, we can exactly compute the amplitudes using the results in Secs. II and III.

D. Amplitude interpolation

Evaluating the amplitudes in Eq. (136) is computationally very expensive, since, as seen in Secs. II and III we have to compute many Bessel functions to determine the amplitudes of the Fourier modes N_{n-m}^{lm} (Eqs. (31) and (24)), elliptic functions and integrals to compute the periodic variation of the Euler angles $\delta\phi_z$ (Eq. (77c)) and $\delta\zeta$ (Eq. (80c)), and we have to evaluate the Wigner D-matrices themselves, which for $l = 2$, $m = \{0, \pm2\}$ are given in appendix E. Furthermore, as seen in Eq. (136), with the SUA approximation we have to evaluate the amplitudes $2k_{\max} + 1$ times per stationary time.

To avoid the computation of the amplitudes to dominate the runtime, we note that they are relatively slow-varying functions of time, and therefore, we can interpolate them. Writing the amplitudes of Eq. (19) explicitly we have

$$
\mathcal{A}_{2,m_i,n_i}^{+,\times} = N_{n_i - m_i}^{2,m_i}(t) \mathsf{A}_{2,m_i}^{+,\times}(t).
\tag{137}
$$

Here, we distinguish two terms, the first term $(N_{n_i-m_i}^{2,m_i}(t)$, defined in Eq. (16)) is related with the amplitude of each Fourier mode, and it varies on the radiation reaction time-scale. The second term $(\mathsf{A}_{2,m_i}^{+,\times}(t)$, defined

in Eq. (14)) is related with how the amplitude evolves as the binary precesses and its frequency increases. Therefore, $\mathsf{A}_{2,m_i}^{+,\times}(t)$ varies on the spin-precession time-scale and, as we see in Eq. (137), it only depends on the m_i of each mode, which can be 0, 2 or −2.

Given the differences between the two terms of Eq. (137), it makes sense to interpolate them separately. We start with $N_{n_i-m_i}^{2,m_i}(t)$. As seen in Sec. VI C, which modes to include is chosen at each interval of the Runge-Kutta. Furthermore, as seen in Eqs. (24) and (31), these amplitudes only depend on the eccentricity $e(t)$. If at each segment of the Runge-Kutta the eccentricity $e^2(t)$ is well approximated by a polynomial like Eq. (113), we can then expect that $N_{n_i-m_i}^{2,m_i}(e^2(t))$ can also be accurately represented like this, i.e.

$$N_{n_i-m_i}^{2,m_i}(t) = \sum_{k=0}^{4} Q_{N,i,j,k} \left(t - (t_j - k_{\max} T_i^{\mathrm{SPA}}) \right)^k,$$
$$\text{with} \quad t_j - k_{\max} T_i^{\mathrm{SPA}} \le t \le t_{j+1} + k_{\max} T_i^{\mathrm{SPA}}, \tag{138}$$

where we have slightly expanded the Runge-Kutta segment to take into account that we have to perform the SUA time-shifts. To find the coefficients $Q_{N,i,j,k}$ we evaluate $N_{n_i-m_i}^{2,m_i}(t)$ in $N_{\mathrm{fit}} = 5 + N_{\mathrm{extra}}$ Chebyshev nodes of the second kind [116, 131] between $t_j - k_{\max} T_i^{\mathrm{SPA}}$ and $t_{j+1} + k_{\max} T_i^{\mathrm{SPA}}$, i.e.

$$t_q^{\mathrm{fit}} = t_{\mathrm{start}} + \sin^2\left(\frac{q}{2(N_{\mathrm{fit}} - 1)} \right) \Delta t, \quad q = 0, \dots, N_{\mathrm{fit}} - 1, \tag{139}$$

where $t_{\mathrm{start}} = t_j - k_{\max} T_i^{\mathrm{SPA}}$ and $\Delta t = t_{j+1} - t_j + 2k_{\max} T_i^{\mathrm{SPA}}$. We then fit the polynomial of Eq. (138) to these points. Note that we add N_{extra} points more than strictly needed for interpolation. For small values of N_{extra} (e.g. 1 or 2), this makes the polynomial fitting more robust and accurate at small additional computational cost.

Next we interpolate the "precession" amplitudes $\mathsf{A}_{2,m}^{+,\times}(t)$. We only need to interpolate them for $m = \{0, 2\}$, since using Eq. (13) we have that $\mathsf{A}_{2,-2}^{+,\times} = (\mathsf{A}_{2,2}^{+,\times})^*$. These precession amplitudes are oscillating functions of time. Part of it is due to the Euler angles $(\phi_z, \theta_L, \zeta)$ oscillating in each precession cycle, having a period of π in $\bar{\psi}_p$. The other part of the oscillation is due to the secular evolution of the Euler angles that enter the Wigner matrices, i.e. $D_{m',m}^l \propto e^{-i(m'\phi_{z,0}+m\zeta_0)}$. This oscillation has a period of 2π in $(m'\phi_{z,0}+m\zeta_0)$. To accurately interpolate the precession amplitudes, we need to evaluate them at least a few times per cycle. To guarantee this, we define

$$\Delta\varphi_{\mathrm{p},j}(t) = \sum_{k=1}^{4} Q_{\varphi_{\mathrm{p}},j,k}(t - t_j)^k, \quad t_j \le t \le t_{j+1}, \tag{140a}$$

$$Q_{\varphi_{\mathrm{p}},j,k} = Q_{\bar{\psi}_{\mathrm{p}},j,k} + \mathrm{sign}(Q_{\phi_{z0},j,1})Q_{\phi_{z0},j,k} \tag{140b}$$

where the $\mathrm{sign}(Q_{\phi_{z0},j,1})$ factor is introduced in case $\phi_{z,0}$ is decreasing in a segment. Then, we can make sure that the amplitudes $\mathsf{A}_{2,m}^{+,\times}(t)$ are being evaluated more than N_{p} times per cycle if in each Runge-Kutta time segment we pick interpolation times $t_{j,q}^{\mathrm{interp}}$ such that

$$\Delta\varphi_{\mathrm{p},j}(t_{j,q}^{\mathrm{interp}}) = \frac{\pi}{N_{\mathrm{p}}} q, \quad q = 0, \dots, \left\lfloor \frac{N_{\mathrm{p}}}{\pi} \Delta\varphi_{\mathrm{p},j}(t_{j+1}) \right\rfloor, \tag{141}$$

where $\lfloor \cdot \rfloor$ denotes the floor operation and Eq. (141) can, in the same way as Eq. (134), be solved using the series reversion procedure described in appendix D. Then, we interpolate the amplitudes $\mathsf{A}_{2,m}^{+,\times}(t)$ in the grid of points $\{t_{j,q}^{\mathrm{interp}}\}$. In particular, we choose to do a cubic spline interpolation [107, 116] as it will represent oscillatory functions with high accuracy without needing too many interpolation points per cycle N_{p}.

VII. TESTING AND VALIDATION

For the pyEFPE waveform approximant to be useful in the analysis of GW detector data, it has to satisfy two conditions. First and foremost, it has to accurately describe the GW emission of the system that is being modeled, to guarantee the validity of scientific statements derived from it. However, it also has to be computationally efficient for its application to the data to be technically feasible. In this section we will test how well both conditions are satisfied.

We start by checking that pyEFPE gives the expected waveform phenomenology. To this end, in Fig. 3 we show a sample waveform for a highly-eccentric system with masses consistent with a binary neutron star (BNS)[2], with the parameters listed in the figure caption. Given the very high initial eccentricity ($e_0 = 0.7$) and the tolerance in the amplitude of $\epsilon_N = 10^{-3}$, as seen in Fig. 1, at initial times (low frequencies) we have up to 40 Fourier modes contributing. When computing the amplitude of the frequency-domain waveform, these Fourier modes interfere with each other, and because of this, the GW polarizations of Fig. 3 present very rapid oscillations. However, as the system inspirals, the eccentricity rapidly decreases [134], until only the Fourier mode with $l = m = n = 2$ contributes, and we obtain the smooth amplitudes observed at later times. The system of Fig. 3 is chosen to be initially edge-on (i.e. $\iota_0 = \pi/2$) to maximize the effect of precession on the $\times$ polarization of the $l = m = 2$ GW mode. Indeed, in Fig. 3 we can see how,

---

[2] Note that while the masses are consistent with a BNS, the current model neglects tidal effects.
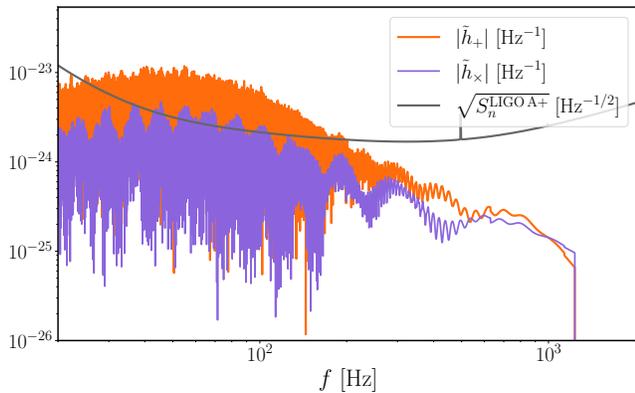
FIG. 3: Frequency domain polarizations for a highly-eccentric binary with masses consistent with a BNS: $m_1 = 2.4 M_\odot$, $m_2 = 1.2$, $q_1 = q_2 = 1$, $e_0 = 0.7$, $\boldsymbol{\chi}_{1,0} = \{-0.44, -0.26, 0.48\}$, $\boldsymbol{\chi}_{2,0} = \{-0.31, 0.01, -0.84\}$, $\iota_0 = \pi/2$, $d_L = 100$ Mpc, $\lambda_0 = \ell_0 = 0$, $f_0^{\mathrm{GW},22} = 10$ Hz and $f_f^{\mathrm{GW},22} = f_{\mathrm{ISCO}}^{\mathrm{GW},22}$ (for the definition of all these parameters see table I). The waveform is computed between $f_{\mathrm{low}} = 20$ Hz and $f_{\mathrm{high}} = 4096$ Hz with a frequency resolution of $\Delta f = 1/128$ Hz. Furthermore, the amplitude tolerance is taken to be $\epsilon_N = 10^{-3}$ (Eq. (40)) and for the SUA we use $k_{\mathrm{max}} = 3$. We also show the square root of the Advanced LIGO A+ PSD [132, 133]. With this PSD, the optimal SNRs of the plus and cross polarizations are 34.8 and 15.7, respectively.

on top of the rapid oscillations previously mentioned, the amplitude of the $\times$ polarization has a slow modulation which is due to spin-precession.

The physics at play in the binary are clearer when looking at the time-domain polarizations. To determine these, we compute the inverse Fast Fourier Transform (iFFT) of the frequency-domain polarizations in Fig. 3, obtaining the result shown in Fig. 4. In the top panel we observe that, even though the segment duration is $T = 128$ s (since the frequency resolution in Fig. 3 is $\Delta f = 1/128$ Hz), the waveform is different from zero only for $(t - t_c) > -\tau_c$, with $\tau_c = 66.1$ s being the coalescence time of the system from the chosen initial frequency $f_0^{\mathrm{GW},22} = 10$ Hz. In the top panel of Fig. 4 we also observe how the signal slowly evolves due to radiation reaction, increasing in frequency and amplitude and decreasing in eccentricity. In this panel we can also clearly observe the modulation of the $\times$ amplitude due to spin-precession, that makes the inclination vary with time, and when the system is edge-on ($\iota = \pi/2$), the $\times$ polarization vanishes. To better observe this effect, in the middle panel we zoom into a precession cycle. Here we can start to discern how the waveform is composed of a series of spikes that correspond to a burst of GWs emitted each time the binary passes through periastron. We also see how the phase of each burst is different at each periastron passage, having a periodic variation due to the effect of periastron advance. In the bottom panel we zoom into one of these periastron advance cycles to more

clearly see the periodic change in phase and the characteristic shape of each GW burst, that requires many Fourier modes to be described.

A. Waveform comparisons

In this sub-section we will test the accuracy and computational speed of pyEFPE. Given that there are no widely available waveforms that include both orbital eccentricity and spin-precession, we will check that pyEFPE reduces to the correct limits when we turn one (or both) of these effects. Instead of working with the two polarizations, h_+ and $h_\times$, we compare the strains h along a given direction forming an angle of ψ with the polarization frame, i.e.

$$h = \cos(2\psi) h_+ + \sin(2\psi) h_\times \,, \qquad (142)$$

where ψ is the polarization angle. As is standard practice, to measure how similar two strains h_1 and h_2 are, we compute their match $\mathcal{M}$ [120, 135] as

$$\mathcal{M}(h_1, h_2) = \frac{\langle h_1, h_2 \rangle}{\sqrt{\langle h_1, h_1 \rangle \langle h_2, h_2 \rangle}} \,, \qquad (143)$$

where we have introduced the noise-weighted inner product $\langle \cdot, \cdot \rangle$, defined by the overlap integral [120, 135]

$$\langle a, b \rangle = 4 \mathrm{Re} \left\{ \int_{f_{\mathrm{min}}}^{f_{\mathrm{max}}} \frac{\tilde{a}^*(f) \tilde{b}(f)}{S_n(f)} \mathrm{d}f \right\} \,, \qquad (144)$$

where $S_n(f)$ is the one-sided noise Power Spectral Density (PSD) of the detector. Unless otherwise specified, we use the projected PSD for LIGO A+ [132, 133], shown in Fig. 3. Given that $\langle \cdot, \cdot \rangle$ is an inner product, by the Cauchy–Schwarz inequality we have that $\mathcal{M} \leq 1$, with $\mathcal{M} = 1$ only if $\tilde{h}_1 \propto \tilde{h}_2$. Therefore, to measure the difference between two waveforms, we use the mismatch $\mathcal{MM}$, defined as

$$\mathcal{MM}(h_1, h_2) = 1 - \mathcal{M}(h_1, h_2) \,. \qquad (145)$$

When comparing different waveform approximants, it is sometimes hard to choose both waveforms to represent the same physical system due to differences in conventions, for example in the reference orbital phase ϕ_0, the reference time t_0, the polarization angle ψ or rigid rotations of the in-plane spins by an angle ϕ_S. Since the variables previously mentioned have small astrophysical importance, it is standard practice to minimize the mismatch over them when comparing different waveform models. Therefore, we define

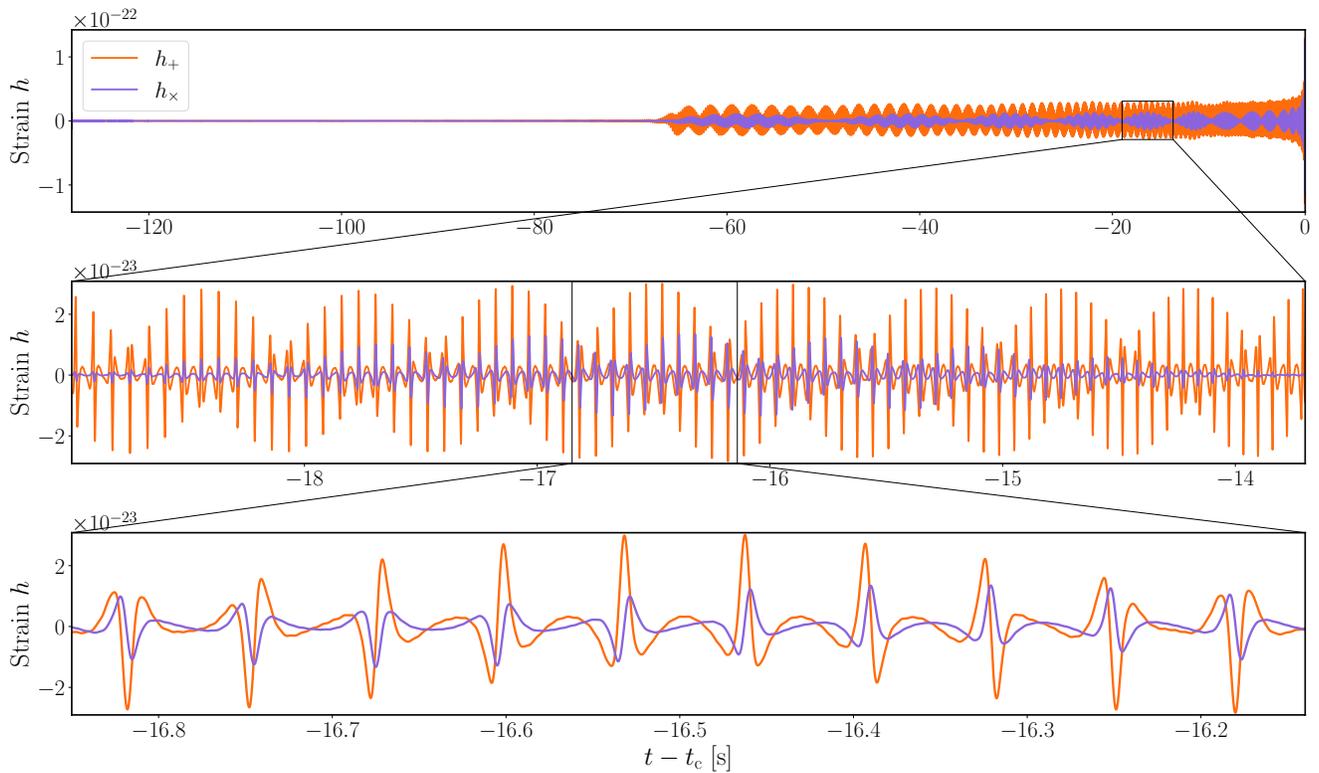$$\overline{\mathcal{MM}}(h_1, h_2) = \min_{\phi_0, t_0, \psi, \phi_S} \mathcal{MM}(h_1, h_2) \,. \qquad (146)$$

FIG. 4: Time-domain polarizations for the same highly eccentric BNS-like system of Fig. 3. We obtain the time-domain waveform by doing the iFFT of the frequency-domain polarization shown in Fig. 3, using that $\tilde{h}(-f) = \tilde{h}^*(f)$. In the top panel we show the full time-domain waveform, while in the middle and bottom panels we zoom into a precession cycle and a periastron advance cycle respectively.

Following Ref. [136], we analytically optimize over the polarization angle ψ and numerically optimize over the reference time t_0 using the FFT. To numerically optimize over the reference phase ϕ_0 and the rotation angle of the spins ϕ_S we use a brute force method.

As is conventional, we approximate the frequency integrals of Eq. (144) by summing over the Fourier frequencies assuming a segment of duration T [137], i.e.

$$\langle a, b \rangle = 4\mathrm{Re} \left\{ \sum_{k=\lceil f_{\min}/\Delta f \rceil}^{\lfloor f_{\max}/\Delta f \rfloor} \frac{\tilde{a}^*(k\Delta f)\tilde{b}(k\Delta f)}{S_n(k\Delta f)} \Delta f \right\}, \tag{147}$$

where

$$\Delta f = \frac{1}{T}, \tag{148}$$

is the frequency resolution of the FFT. The segment duration T is chosen such that it contains the full signal studied. For the mismatch computations performed in this section, we use $f_{\min} = f_0^{\mathrm{GW},22} = 20$ Hz. To compute the duration of the signals, an upper bound is given by [121]

$$\tau_c \lesssim \frac{5}{256} \left(\frac{G\mathcal{M}_c}{c^3} \right)^{-5/3} \left(\pi f_0^{\mathrm{GW},22} \right)^{-8/3}, \tag{149}$$

where, as seen in Eq. (C8), for systems with large eccentricities the duration is significantly shorter [134], and we have introduced the chirp mass $\mathcal{M}_c$,

$$\mathcal{M}_c = \frac{(m_1 m_2)^{3/5}}{(m_1 + m_2)^{1/5}}. \tag{150}$$

In table II we show the different segment durations considered in this section with their corresponding chirp mass ranges. When testing the waveforms, we take random samples uniformly distributed in each chirp mass range. We always sample uniformly in mass ratio $q = m_2/m_1 \in [0.05, 1]$, the cosine of the reference inclination $\cos \iota_0 \in [-1, 1]$, the reference phase $\phi_0 = \lambda_0 \in [0, 2\pi]$ and the polarization angle $\psi \in [0, \pi]$. In all of the comparisons we evaluate our model assuming black holes (i.e. $q_1 = q_2 = 1$) and simulating the pyEFPE dynamics to the ISCO (i.e. $f_f^{\mathrm{GW},22} = f_{\mathrm{ISCO}}^{\mathrm{GW},22}$). The distributions of the spins and eccentricities as well as maximum integration frequency $f_{\max}$ will be different for the different comparisons that will be considered.

T [s]	$\mathcal{M}_c$ [$M_\odot$]	
	Min.	Max.
4	12	20
8	8	12
16	5	8
32	3.3	5
64	2.2	3.3
128	1.4	2.2
256	0.95	1.4

TABLE II: Segment durations T studied in this section and the chirp mass range used for each one.

Finally, unless otherwise specified, we use an amplitude tolerance of $\epsilon_N = 10^{-3}$ (see Eq. (40)), for the SUA we use $k_{\max} = 3$ (see Eq. (108)), and interpolate the amplitudes using $N_{\mathrm{extra}} = 2$ (see Eq. (139)) and $N_{\mathrm{p}} = 40$ (see Eq. (141)). These are the default values of `pyEFPE`, as they are found to be a good compromise between accuracy and computational efficiency. For the different waveforms we compare with, we use their publicly available `lalsuite` [138] implementation.

1. Amplitude Interpolation

We start comparing `pyEFPE` with and without interpolating the amplitudes as described in Sec. VI D. For the amplitude interpolation to be useful, it has to accurately represent the exact waveform as well as speed up the evaluation of the model. To test the accuracy of the interpolation, we compute the mismatch between the exact and interpolated waveforms using Eq. (145). We do not minimize the mismatch over any parameter, since, given a set of parameters, the interpolated and exact versions of `pyEFPE` should represent the same system. To measure the speedup, we just compute the ratio between the runtime of `pyEFPE` with the exact and interpolated amplitudes, i.e.

$$\text{Speedup} = \frac{T_{\mathrm{R,exact}}}{T_{\mathrm{R,interpolated}}} . \tag{151}$$

In Fig. 5 we show the distribution of mismatches and speedups for 2000 samples at each segment duration (and corresponding chirp mass range) of table II. For the distribution of the spins, we have chosen isotropic orientations and uniform spin magnitudes $\chi_i \in [0, 0.9]$, while for the eccentricity we have chosen a uniform distribution $e_0 \in [0, 0.7]$.

In Fig. 5 we observe that the mismatches are usually very small with the 95% quantile being below 10^{-6} in all cases. However, there is a small tail extending to mismatches of up to $\sim 10^{-2}$. These high mismatches correspond to systems where the MSA approximation develops a discontinuity that makes the interpolation of the amplitudes fail. These discontinuities can happen because
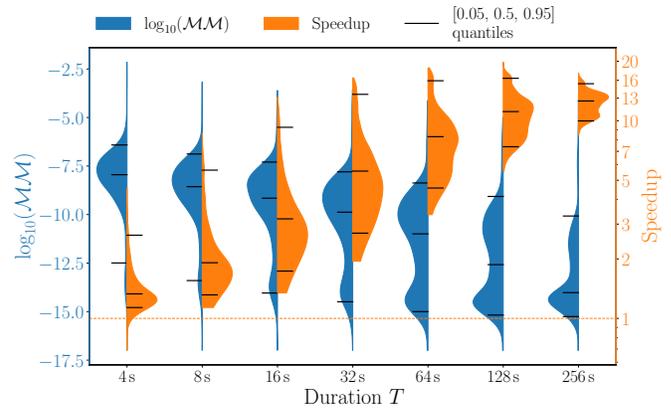
FIG. 5: Violin plots showing the distribution of the mismatches (left part, Eq. (145)) and Speedup (right part, Eq. (151)) when comparing `pyEFPE` with and without amplitude interpolation as a function of the segment duration T or, equivalently, the chirp mass $\mathcal{M}_c$ range as specified in table II. Each distribution consists of 2000 random samples drawn from the distributions as described in Sec. VII A 1.

of very abrupt transitional precession or because we pass through a point with $|\cos\theta_L| = 1$, which causes a physical discontinuity in $\mathcal{D}\phi_z$ and $\mathcal{D}\zeta$ (see Eq. (70)) that then becomes a spurious discontinuity in $\delta\phi_z$ and $\delta\zeta$ when doing the MSA (see Eq. (77c) and Eq. (80c)).

In Fig. 6 we show an example of such a discontinuity by plotting the exact and interpolated $\mathsf{A}_{2,2}^{+,\times}$ amplitudes for the case with the largest mismatch of the $T = 256\,$s samples, having the parameters listed in the caption. While it is hard to interpolate such narrow features in the amplitudes, these deviations are not a concern, since they happen where the MSA approximation fails and the model is not expected to be accurate.

Going back to Fig. 5, we observe that, the larger the segment duration, the larger the speedup, going from $\sim$ 1-2 for the $T = 4\,$s set to $\sim$ 10-15 for the $T = 256\,$s set. The reason for this increase is that, even though the speedup of interpolating the amplitudes is always ~ 20, shorter waveforms evaluate the amplitudes in fewer points and it represents a smaller fraction of the code runtime. For the same reason, within each segment duration there is a large spread of speedups, as samples with high eccentricity have a large amount of Fourier modes contributing, needing more amplitude evaluations, and benefiting more from the interpolation speeedup. Instead, for waveforms with few amplitude evaluations, the runtime is dominated by the adaptive Runge-Kutta used to integrate the equations of motion of Eq. (110). We observe that for some of the waveforms with durations of $T = 4\,$s, the speedup can even be smaller than 1, due to the overhead of setting up the amplitude interpolation.

While the model's runtime heavily depends on the hardware it runs on, it is useful to give an idea of the computational cost of the waveform and determine if it
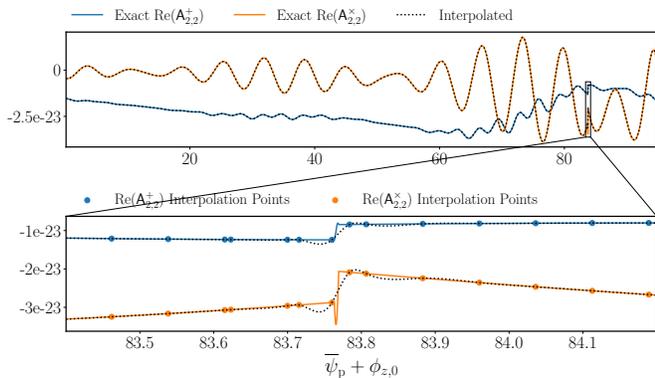
FIG. 6: Real part of the exact and interpolated $\mathsf{A}_{2,2}^{+,\times}$ amplitudes (Eq. (14)) for the sample with the largest mismatch of the $T = 256\,\mathrm{s}$ distribution shown in Fig. 5, having $\mathcal{MM} = 8.8 \cdot 10^{-5}$. We plot it as a function of $\overline{\psi}_{\mathrm{p}} + \phi_{z,0}$, since this is the variable we are doing a semi-regular grid interpolation on (see Eq. (140)). In the bottom panel we zoom into the amplitude discontinuity that is making the interpolation inaccurate and plot the interpolation points. The parameters of the sample shown are $m_1 = 1.656 M_\odot$, $m_2 = 1.331 M_\odot$, $e_0 = 0.596$, $\boldsymbol{\chi}_{1,0} = \{-0.092, -0.741, 0.501\}$, $\boldsymbol{\chi}_{2,0} = \{0.358, -0.118, 0.260\}$, $\iota_0 = 1.478\,\mathrm{rad}$, $\lambda_0 = 1.199\,\mathrm{rad}$, $\ell_0 = 0.716\,\mathrm{rad}$ and is located at $d_L = 10\,\mathrm{Mpc}$.

is suitable for data analysis applications. A typical number of waveform evaluations N_{wf} in GW parameter estimation (PE) is $N_{\mathrm{wf}} \sim \mathcal{O}\left(10^8\right)$. Therefore, if the mean waveform evaluation time is T_{wf} and the analysis is parallelized on N_{cores}, the PE runtime is

$$T_{\mathrm{PE}} = 1.8\,\mathrm{days} \left(\frac{N_{\mathrm{wf}}}{10^8}\right) \left(\frac{T_{\mathrm{wf}}}{0.1\,\mathrm{s}}\right) \left(\frac{64}{N_{\mathrm{cores}}}\right), \quad (152)$$

assuming the waveform evaluation dominates the computational cost of PE, which is usually the case. With Eq. (152) we have an estimate of the waveform runtime necessary for PE to be computationally feasible, usually requiring that $T_{\mathrm{wf}} \lesssim 1\,\mathrm{s}$, for PE analyses to finish in a time-scale of weeks.

In Fig. 5, we show, for the same samples as in Fig. 7, the pyEFPE runtimes on a single core of an *Intel Core i7-1185G7* laptop processor. As expected, we observe that, for longer duration signals the runtime is larger, as the waveform has to be sampled at more frequencies, and for the smaller masses the Runge-Kutta integrates over longer times. For the interpolated version of pyEFPE we see that the waveform evaluation is mostly under $\sim 0.1\,\mathrm{s}$ for $T \leq 32\,\mathrm{s}$ and under $\sim 0.5\,\mathrm{s}$ for $T \leq 32\,\mathrm{s}$, meaning that PE studies are computationally feasible in a time-scale of days. However, without the amplitude interpolation, each waveform evaluation can take more than $1\,\mathrm{s}$ for $T \geq 64\,\mathrm{s}$, leading to PE analyses entering time-scales of weeks to months. Therefore, the amplitude interpolation will be crucial to make PE studies computationally feasible.
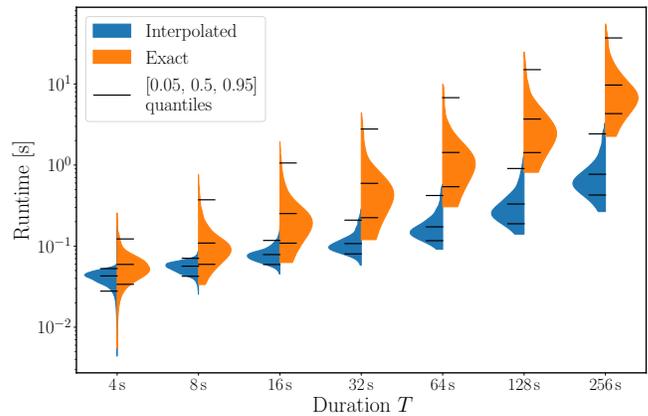
FIG. 7: Violin plots showing the distribution of the pyEFPE runtime with interpolated amplitudes (left part) and exact amplitudes (right part) as a function of the segment duration T or, equivalently, the chirp mass $\mathcal{M}_c$ range as specified in table II. The runtime distributions shown, use the same samples as in Fig. 5, and were computed on a single core of an *Intel Core i7-1185G7* laptop processor.

2. Comparison with quasi-circular spin-aligned models

To validate pyEFPE, we start by comparing it with other PN inspiral waveforms in the simplest scenario of quasi-circular orbits and spins aligned with the orbital angular momentum, minimizing precession effects. Therefore, we fix $e = \chi_{i\perp,0} = 0$ for all samples tested and choose uniform distributions for the spin components aligned with the orbital angular momentum $\chi_{iz,0} \in [-0.9, 0.9]$. To avoid boundary effects, we perform the overlap integrals of Eq. (144) up to a frequency of $f_{\max} = 0.8 f_{\mathrm{ISCO}}$. Unless otherwise specified, for the PN models we take the same PN orders as for pyEFPE, i.e. 3PN for the spinning and non-spinning parts of the phasing and 0PN for the amplitude.

The first model we compare with is SpinTaylorT4 [138–141], a time-domain quasi-circular precessing model that integrates the same PN evolution equations as pyEFPE in the $e \rightarrow 0$ limit [139]. However, to account for precession, instead of the MSA approximation it numerically solves the quasi-circular version of the precession equations of Eq (41), taking into account corrections up to 3PN (instead of the 2PN order used by pyEFPE). In Fig. 8 we observe that, in spite of their differences, the mismatches between pyEFPE and SpinTaylorT4 are very small, with the bulk of the distributions being below values of $\overline{MM} \lesssim 10^{-3}$, and mismatches becoming smaller as the signals become longer. These small mismatches are mostly due to SpinTaylorT4 being converted to the frequency-domain using an FFT, whereas pyEFPE uses the SUA to obtain the frequency-domain waveform. We can also see that the mismatch distributions have very long tails extending to $\overline{MM} \sim 10^{-1}$, corresponding to systems
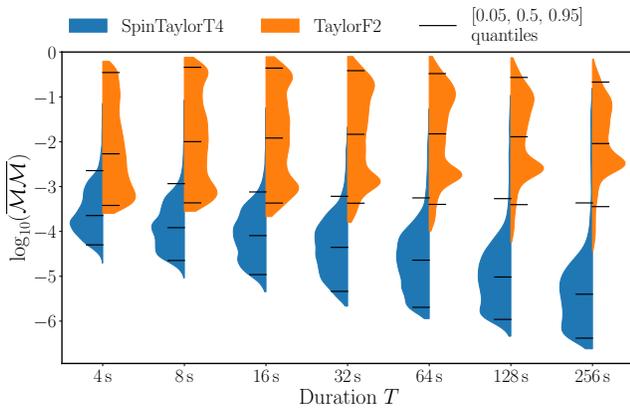
FIG. 8: Violin plots showing the distribution of the mismatch $\overline{\mathcal{MM}}$ (Eq. (146)) between `pyEFPE` and `SpinTaylorT4` (left part) and `TaylorF2` (right part) in the aligned spin case as a function of the segment duration T, or equivalently the chirp mass $\mathcal{M}_c$ range as specified in table II. Each distribution shown consists of 10000 random samples drawn from the distributions described in the text.

FIG. 9: Scatter plot of the mismatches between `pyEFPE` and `TaylorF2` as a function of the effective inspiral spin parameter $\chi_{\rm eff}$ and mass ratio q. The samples shown correspond to the same 10000 samples in the $T = 256\,{\rm s}$ distribution of Fig. 8.

that have

$$\left(\frac{\delta\mu}{y}\right)^2 - 2\delta\chi_0\frac{\delta\mu}{y} + |\boldsymbol{s}_{1,0} + \boldsymbol{s}_{2,0}|^2 \leq 0\,, \qquad (153)$$

for some $y \in [y_0, y_f]$. When this happens, $p_\parallel$ in Eq. (61a) becomes smaller than 0 and, even in the zero-initial perpendicular spin case where $p_\perp = q_\perp = 0$, we have that $\arg(G) = \pi$ and the elliptic parameter in Eq. (65b) becomes $m = 1$. The resulting effect is to make the non-precessing configuration unstable under small perturbations, as also seen in Refs. [142, 143]. Since we have numerical errors, when Eq. (153) is satisfied, this instability is realized and both the `pyEFPE` and `SpinTaylorT4` waveforms become precessing. However, they do so in different ways leading to the relatively large mismatches observed. Given that in nature we never expect the perfectly aligned-spin configuration $\chi_{1\perp,0} = \chi_{2\perp,0} = 0$ to be exactly achieved, these cases are not a cause of concern.

In Fig. 8 we also compare against `TaylorF2` [138, 139, 141, 144], the widely-used frequency-domain quasi-circular non-precessing model. We observe that in this case, the mismatches are significantly higher than in the `SpinTaylorT4` case. This is a well known issue when comparing PN approximants [145, 146]. The difference between the `SpinTaylorT4` family of approximants `pyEFPE` belongs to, and `TaylorF2` is in how we write the evolution equations [139], having at 3PN that

$$(\mathcal{D}y)^{\rm T4} = \nu y^9 \left(a_0 + \sum_{n=2}^{6} a_n y^n\right)\,, \qquad (154a)$$

$$(\mathcal{D}y)^{\rm F2} = \nu y^9 a_0 \frac{1}{1 - \sum_{n=2}^{6} c_n y^n}\,, \qquad (154b)$$

where the Taylor series of both agree up to $\mathcal{O}\left(y^{15}\right)$. The problem is that, for extreme mass ratios (i.e. $q = m_2/m_1 \to 0$) and effective spin parameters (i.e. $|\chi_{\rm eff}| \to 1$), the difference between these two expressions for $\mathcal{D}y$ can become significant [145], especially at large values of y. This trend can clearly be seen in Fig. 9, where we show the mismatch between `pyEFPE` and `TaylorF2` for the samples with $T = 256\,{\rm s}$ as a function of $\chi_{\rm eff}$ and q. In agreement with Ref. [145], we observe that the mismatch grows for small mass ratios and large moduli of the effective spin parameter. On top of this ordered trend, we also observe that there are some samples with $q \sim 1$ and $\chi_{\rm eff} \sim 0$ having mismatches all over the place. These are samples satisfying Eq. (153) for which `pyEFPE` dynamically acquires precession.

3. Comparison with quasi-circular precessing models

Now that we have validated that `pyEFPE` reduces to the expected limits in the quasi-circular spin-aligned case, we will test its behaviour in the generic spin case, where the effect of spin-precession is present. Therefore, we still fix $e = 0$ for all samples tested, but now use isotropic distributions in the component spin directions and uniform distributions in the component spin magnitudes $\chi_i \in [0, 0.9]$.

In Fig. 10 we compare `pyEFPE` with `SpinTaylorT4` in this precessing case, again integrating up to $f_{\rm max} = 0.8f_{\rm ISCO}$, using the 0PN amplitudes and 3PN non-spinning terms in the evolution equations. However, we now consider two different cases, one where the spinning part of the evolution equations is taken to 2PN (labeled "2PN Spin") and other where they are taken to 3PN (labeled "3PN Spin"). However, in the "3PN Spin" case, while the precession equations of `SpinTaylorT4` include corrections up to 3PN, the `pyEFPE` ones, given in Eq. (41),
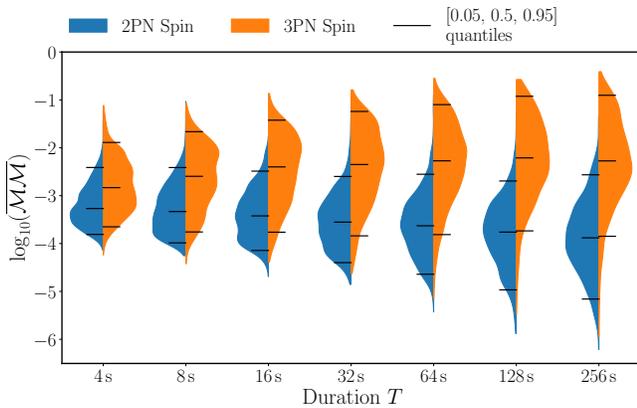
FIG. 10: Violin plots showing the distribution of the mismatch $\overline{\mathcal{MM}}$ (Eq. (146)) between two configurations of `pyEFPE` and `SpinTaylorT4` in the precessing spin case as a function of the segment duration T, or equivalently the chirp mass $\mathcal{M}_c$ range as specified in table II. The configuration "2PN Spin", in the left part of the violins, corresponds to taking the precession and spinning part of the evolution equations equations of both approximants at 2PN. The "3PN Spin" configuration, in the right part of the violins, corresponds to taking the precession at 2PN for `pyEFPE` and 3PN for `SpinTaylorT4`, and the spinning part of the evolution equations at 3PN for both. Each distribution shown consists of 2000 random samples drawn from the distributions described in the text.

FIG. 11: Violin plots showing the distribution of the mismatch $\overline{\mathcal{MM}}$ (Eq. (146)) between `pyEFPE` and `IMRPhenomXP` in the precessing spin case as a function of the segment duration T, or equivalently the chirp mass $\mathcal{M}_c$ range as specified in table II. In the left part of the violins we compute the mismatch (Eq. (144)) up to $f_{\max} = 0.8 f_{\mathrm{MECO}}$, while in the right side we only compute it up to $f_{\max} = 0.2 f_{\mathrm{MECO}}$. The MECO frequency is obtained with the phenomenological fit introduced in Ref. [144]. When $f_{\max} = 0.2 f_{\mathrm{MECO}}$ we do not show mismatches for $T \leq 16\,\mathrm{s}$ (i.e. $\mathcal{M}_c \leq 8 M_\odot$), since some samples have $f_{\max} < f_{\min}$. Each distribution shown consists of 2000 random samples drawn from the distributions described in the text.

are limited to 2PN, where the MSA approximation is known.

For the "2PN Spin" case, we find very small mismatches, similar to the ones observed in the 3PN aligned spin case of Fig. 8, given us confidence in the fact that the MSA approximation is excellently describing the exact solution of the 2PN precession, also when including radiation reaction effects. In a similar way to the aligned spin case, the difference between `SpinTaylorT4` and `pyEFPE` is mostly due to the difference between computing the frequency domain waveform with the FFT and the SUA respectively. However, in this non-aligned spin case, there will be additional small differences between the two models coming from the residual eccentricity discussed in Eq. (85), which is neglected in `SpinTaylorT4`.

For the "3PN Spin" case of Fig. 10, the mismatches are bigger than for the "2PN Spin", growing for longer signals. This is due to `SpinTaylorT4` including higher PN information in the precession equations. While these small corrections in the precession frequencies are not important for short signals that have few precession cycles, it can accumulate over the many precession cycles of long, leading to the mismatches observed in Fig. 10. However, even for the longest signals studied in the "3PN Spin" case, the mismatches still satisfy $\overline{\mathcal{MM}} \lesssim 10^{-1}$, indicating that the use of the 2PN precession equations may be adequate for current GW detectors [147], though a detailed investigation on accuracy requirements should be conducted. However, improvements to the precession

description will be important for future GW detectors such as LISA [37], the Einstein Telescope [148, 149], or Cosmic Explorer [150], where signals are expected to be louder and longer.

In Fig. 11 we compare `pyEFPE` against `IMRPhenomXP` [125, 138], one of the most widely used models in GW data analysis. `IMRPhenomXP` is a precessing frequency-domain phenomenological inspiral-merger-ringdown (IMR) model obtained by twisting up the aligned-spin model `IMRPhenomXAS` [144]. The inspiral part of `IMRPhenomXAS`, used to generate the waveform at frequencies bellow the MECO ($f \lesssim f_{\mathrm{MECO}}$) is based on `TaylorF2` at 3.5PN, augmented adding pseudo-PN coefficients to pseudo-6PN in the phase and pseudo-4.5PN in the amplitude. The pseudo-PN coefficients mimic the expected analytical structure of higher PN orders and are fitted to `SEOBNRv4` [151] and NR [152]. The Euler angles to rotate `IMRPhenomXP` are derived using a PN expansion within the MSA framework described in Ref. [82] for the quasi-circular limit of the 2PN precessing equations used in `pyEFPE` (Eq. (41)).

Therefore, the comparison with `IMRPhenomXP` is specially relevant, as it is fitted to EOB and NR, more closely representing the exact GW emission of a binary than the PN approximants. Since `pyEFPE` is an inspiral model, we only compare it with the inspiral part of `IMRPhenomXP`. To take as much of the inspiral as possible while avoiding any effects from the merger-ringdown, we
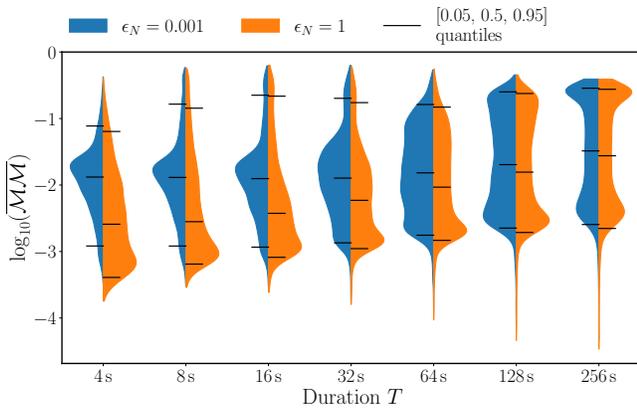
FIG. 12: Violin plots showing the distribution of the mismatch $\overline{\mathcal{MM}}$ (Eq. (146)) between `pyEFPE` and `TaylorF2Ecc` in the aligned spin eccentric case as a function of the segment duration T, or equivalently the chirp mass $\mathcal{M}_c$ range as specified in table II. In the left part of the violins we show the mismatches with the default configuration of `pyEFPE`, that has $\epsilon_N = 10^{-3}$, including as many Fourier modes as necessary to reach that amplitude tolerance. In the right part of the violins, we show the mismatches with `pyEFPE` using $\epsilon_N = 1$, considering only the leading-order Fourier mode. For the eccentricities $e \leq 0.15$ considered here, this corresponds to the $l = m = n = 2$ mode modeled by `TaylorF2Ecc`. Each distribution consists of 10,000 random samples drawn from the distributions described in the text.

first use a maximum frequency to compute mismatches of $f_{\max} = 0.8 f_{\text{MECO}}$, where f_{MECO} is computed with the phenomenological fit introduced in Ref. [144]. The parameters are drawn from the same distribution as in Fig. 10. However, we observe that in this case the mismatches are significantly bigger, specially for longer signals. This is mostly due to the much higher pseudo-PN-order information contained in `IMRPhenomXP`. Nonetheless, as we will see in Sec. VII B 2, `pyEFPE` still describes this waveform with enough accuracy to obtain compatible parameter estimation results. To reduce the effect of these higher pseudo-PN-order corrections, that are most relevant at high frequencies, we also compute mismatches to a very conservative lower maximum frequency of $f_{\max} = 0.2 f_{\text{MECO}}$. In this case, we observe much smaller mismatches. The results of Fig. 11 highlight the importance of adding more PN (or pseudo-PN) information to the phasing and amplitude of `pyEFPE`, especially if we want to describe high SNR systems all the way to the beginning of the merger-ringdown phase. This is left as future work.

4. Comparison with eccentric-spin-aligned models

In this section we restrict ourselves to comparisons with spin-aligned eccentric waveforms. In particular, we compare `pyEFPE` with `TaylorF2Ecc` [138, 153], a
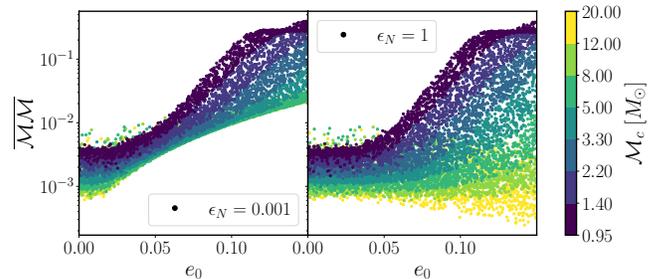
FIG. 13: Scatter plot of the mismatches between `pyEFPE` and `TaylorF2Ecc` as a function of the initial eccentricity e_0 and chirp mass $\mathcal{M}_c$. We plot a subset of the samples shown in Fig. 12 satisfying $q \in [0.5, 1]$ and $\chi_{iz,0} \in [-0.15, 0.15]$. In the left panel we show the same $\epsilon_N = 10^{-3}$ `pyEFPE` configuration shown in the left violins of Fig. 12, while in the right panel we show the $\epsilon_N = 1$ configuration shown in the right violins.

frequency-domain spin-aligned inspiral model that in the quasi-circular limit (i.e. $e \to 0$) reduces to `TaylorF2`. This model has a more limited description of eccentricity than `pyEFPE`, since it only considers the leading order eccentricity contribution to the phasing equations of Eq. (86), which are $\mathcal{O}\left(e^2\right)$ and it neglects all eccentricity corrections to the amplitude, which start at $\mathcal{O}\left(e\right)$. Therefore, `TaylorF2Ecc` is only valid for small eccentricities, in contrast with `pyEFPE`, that is valid for arbitrarily large eccentricities. Because of this, for the mismatches shown in Fig. 12 we consider small initial eccentricities, uniformly distributed with $e_0 \in [0, 0.15]$. As in Sec. VII A 2 we use $f_{\max} = 0.8 f_{\text{ISCO}}$. However, to avoid mismatches being dominated by the PN differences appearing at large spins that were discussed in that section, we use a smaller spin range of $\chi_{iz,0} \in [-0.3, 0.3]$. We test two different tolerances for the `pyEFPE` amplitudes, the default one used in the rest of this work, of $\epsilon_N = 10^{-3}$, and a value of $\epsilon_N = 1$, that guarantees we are only including the leading Fourier mode, that for the low eccentricities considered corresponds to the same $l = m = n = 2$ mode modeled by `TaylorF2Ecc`.

In Fig. 12 we see that the mismatches are generally small. However, they grow as the waveforms become longer. Also, while the case with $\epsilon_N = 10^{-3}$ generally has larger mismatches than the $\epsilon_N = 1$ case, the difference is more important for small mass systems. To better understand these trends, in Fig. 13 we show some of the mismatches of Fig. 12 as a function of initial eccentricity e_0 and chirp mass $\mathcal{M}_c$. To reduce the scatter not due to these two variables, we take the samples of Fig. 12 that satisfy $q \in [0.5, 1]$ and $\chi_{iz,0} \in [-0.15, 0.15]$.

If, as in the right panel of Fig. 13 where $\epsilon_N = 1$, we compare the same Fourier mode of `pyEFPE` and `TaylorF2Ecc`, we observe that for smaller chirp masses (i.e. longer signals), the mismatches start growing at smaller eccentricities and are generally larger. The reason being that, when `TaylorF2Ecc` neglects $\mathcal{O}\left(e^4\right)$ contributions to the phasing of the binary, it is ignoring

phase terms starting at 0PN, that rapidly grow as $Mf_{\min}$ decreases. At fixed eccentricity, the n-PN the contribution to the phase scales as $(Mf_{\min})^{-(5-2n)/3}$, so neglecting any eccentricity term up to 2PN order leads to problems for very low mass systems.

In the left panel of Fig. 13, where $\epsilon_N = 10^{-3}$, we again observe that including the necessary Fourier modes in `pyEFPE`, leads to larger mismatches with `TaylorF2Ecc`. Differences between the two waveforms appear at lower eccentricities than when $\epsilon_N = 1$, since the leading higher order Fourier modes are of order $\mathcal{O}(e)$, compared to the $\mathcal{O}(e^4)$ corrections neglected in the phase. We observe that this effect is specially relevant for systems with larger masses, since they have shorter durations and thus less time to get rid of the eccentricity, having a sizable eccentricity for a bigger fraction of the inspiral than smaller mass systems.

B.   Parameter Estimation

We now directly test `pyEFPE` in GW parameter estimation (PE). Given a GW event candidate, identified by a modeled [28, 154–158] or unmodeled [159–161] search, we want to determine the properties of the system that could have generated the observed strain $d(t)$ in the detector, assuming some signal model with parameters $\boldsymbol{\theta}$. We use Bayesian inference [162, 163] to compute the posterior probability of the signal parameters given the data and a signal model, $p(\boldsymbol{\theta}|d)$, using Bayes' theorem

$$p(\boldsymbol{\theta}|d) = \frac{\mathcal{L}(d|\boldsymbol{\theta})\pi(\boldsymbol{\theta})}{\mathcal{Z}} \tag{155}$$

where $\pi(\boldsymbol{\theta})$ is the prior on the parameters $\boldsymbol{\theta}$, $\mathcal{L}(d|\boldsymbol{\theta})$ is the likelihood, and $\mathcal{Z}$ the evidence or marginalized likelihood. Assuming stationary Gaussian noise, the likelihood reduces to the Whittle likelihood [163, 164]

$$\mathcal{L}(d|\boldsymbol{\theta}) \propto \exp\left\{-\frac{1}{2}\sum_{i=1}^{N}\langle h_i(\boldsymbol{\theta}) - d_i | h_i(\boldsymbol{\theta}) - d_i\rangle_i\right\}$$
$$\propto \exp\left\{\sum_{i=1}^{N}\left(\langle h_i(\boldsymbol{\theta})|d_i\rangle_i - \frac{1}{2}\langle h_i(\boldsymbol{\theta})|h_i(\boldsymbol{\theta})\rangle_i\right)\right\}, \tag{156}$$

where d_i and h_i represent the measured data (including noise) and the GW signal in the i-th detector. Similarly, $\langle\cdot|\cdot\rangle_i$ is the noise weighted inner product, already introduced in Eqs. (144,147), with the i subscript denoting that the PSD of the i-th detector is used. Finally, in Eq. (155) we have introduced the evidence $\mathcal{Z}$, which is a constant which ensures that the posterior probability $p(\boldsymbol{\theta}|d)$ is normalized, i.e.,

$$\mathcal{Z} = \int \mathcal{L}(d|\boldsymbol{\theta})\pi(\boldsymbol{\theta})\mathrm{d}\boldsymbol{\theta}. \tag{157}$$

The evidence $\mathcal{Z}$ measures the expected value of the likelihood in the prior and is used for Bayesian model comparison [165].

Due to the complexity of the integral in Eq. (157), we use Markov chain Monte Carlo (MCMC) methods to obtain the posterior samples. Here, we perform PE using `bilby` [166–168], and in particular, its implementation of the `dynesty` [169] nested sampling algorithm.

To test the PE performance of `pyEFPE` and avoid confounding factors from random noise realizations, we perform zero-noise injections, equivalent to averaging the posterior over infinite Gaussian noise realizations [170]. Therefore, we set the detector strain in Eq. (156) to

$$d_i = h_i^{\mathrm{inj}}(\boldsymbol{\theta}_{\mathrm{inj}}), \tag{158}$$

where h^{inj} and $\boldsymbol{\theta}_{\mathrm{inj}}$ represent the injected model and parameters respectively. We inject our mock signals into the LIGO-Hanford (H1), LIGO-Livingston (L1) and the Virgo detectors, assuming the LIGO A+ and Virgo AdV+ sensitivities projected for O5 [132, 133]. We analyze data from a minimum frequency of $f_{\min} = 20$ Hz, which we also use as the initial frequency for `pyEFPE` (i.e. $f_0^{\mathrm{GW},22} = f_{\min} = 20$ Hz), meaning that the initial eccentricity e_0 is measured at 20Hz. Finally, for the internal configuration of `pyEFPE` we use the default values, also used in the mismatch studies in Sec. VII A.

We choose broad uninformative priors that are uniform in component masses, component spin magnitudes, coalescence time, and isotropic in location in the sky and binary and spin orientations. The distance prior is set assuming uniform probability in source volume, using the *Planck15* cosmology [171]. Finally, when the system is eccentric we use flat priors in the initial eccentricity $e_0 \in [0, 0.4]$ and mean anomaly $\ell_0 \in [0, 2\pi]$.

1.   `pyEFPE` *injection – recovery*

To validate the reliability of PE with the `pyEFPE` approximant, we start by testing whether an injection of `pyEFPE` with specific parameters results in posterior distributions that are compatible with the injected values. To this end, we consider a precessing NSBH-like signal with detector-frame component masses $m_1 = 10M_\odot$ and $m_2 = 1.6M_\odot$ with moderate initial eccentricity $e_0 = 0.2$ defined at a reference frequency of 20 Hz, and recover the signal parameters with `pyEFPE`. We analyze 32 s of data up to a maximum frequency of 300 Hz, taken to be below the Schwarzschild ISCO frequency, i.e., $f_{\max} \approx 0.8f_{\mathrm{ISCO}}$. In Fig. 14 we show the posterior distributions obtained for the most important intrinsic parameters, together with their injected values. More details on the injected signal and posterior distributions for all parameters are given in App. F. In Fig. 14, we quantify the presence of spin-induced orbital precession in terms of the widely used effective precession spin parameter [172], defined as
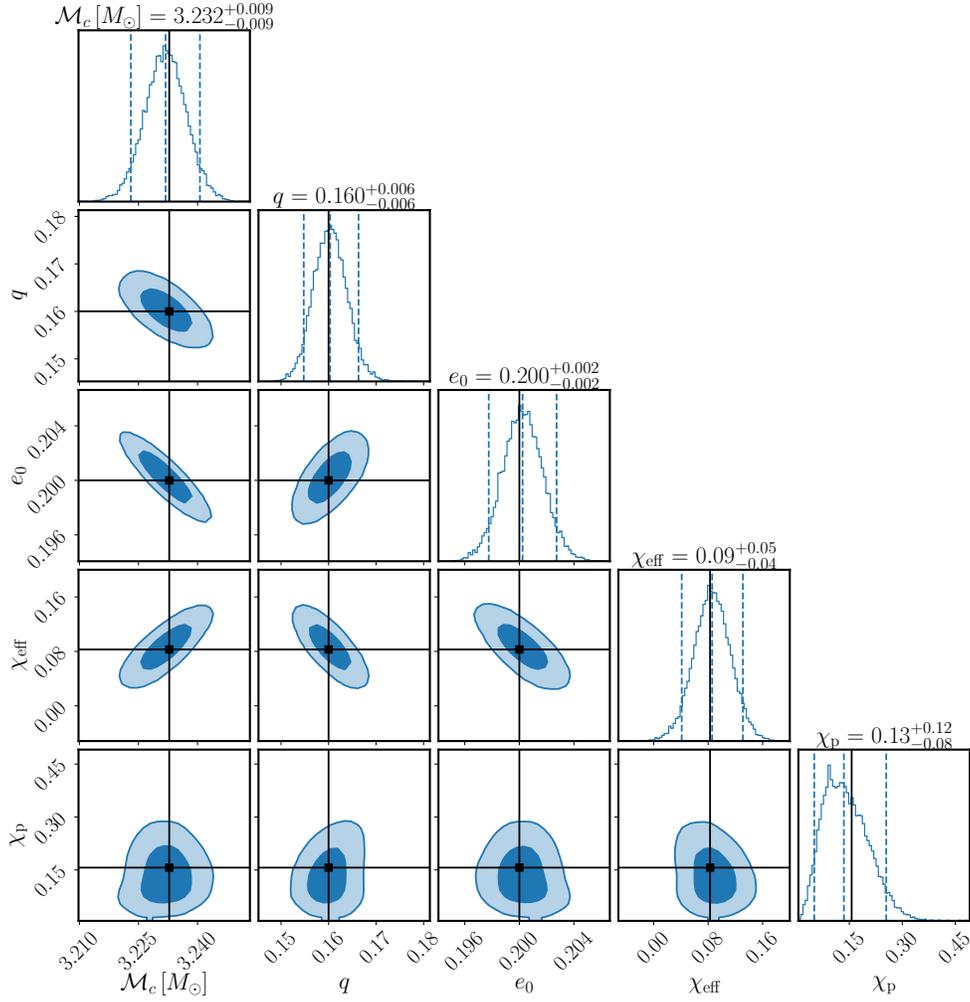
FIG. 14: Corner plot showing the joint posterior distributions of the most important intrinsic parameters of the `pyEFPE` injection-recovery study. Specifically, the plot displays the chirp mass $\mathcal{M}_c$, mass ratio q, initial eccentricity e_0, effective inspiral spin parameter χ_{eff} and effective precession spin parameter χ_{p}. The diagonal panels display the marginal distributions for each parameter, along with the median and 90% confidence interval. The off-diagonal panels show the bivariate correlations between pairs of parameters, with the contours representing the 50% and 90% confidence regions. The black lines mark the values of the injected parameters.

$$\chi_{\mathrm{p}} = \max\left\{\chi_{1\perp,0}, \frac{q(4q+3)}{4+3q}\chi_{2\perp,0}\right\}, \qquad (159)$$

where $\chi_{i\perp,0} = \sqrt{\chi_{ix,0}^2 + \chi_{iy,0}^2}$ is the initial magnitude of the in-plane spin. Firstly, we note that the estimated posteriors are in excellent agreement with the injected values. Secondly, despite the moderate SNR (≈ 19.7) of the injected signal, the intrinsic parameters are very well constrained. While a more detailed investigation into the behavior of PE for eccentric precessing inspirals is outside of the scope of this paper, and left for future work, we suggest a simple, intuitive explanation for this: As discussed in Refs. [115, 121] for quasi-circular binaries, the signal and template waveform must remain in phase for the mismatch to be small. Consequently, each param-

eter θ can be inferred with an accuracy approximately corresponding to the change $\Delta\theta$ that shifts the number of GW cycles in the sensitivity band by order unity. A similar argument extends to each Fourier mode of an eccentric signal. From Eq. (18) it follows that in order to maintain a high match, parameters that cause the phase $n\lambda + (m-n)\delta\lambda$ to vary by more than one cycle need to be excluded. This effectively "measures" the accumulated orbital and periastron advance phases, λ and $\delta\lambda$, with $\mathcal{O}(1)$ precision. Therefore, if these phases are large, the parameters they depend on can be inferred with high accuracy. At leading PN order, the evolutions of λ and $\delta\lambda$ are given by (see App. B)

$$\frac{\mathrm{d}\lambda}{\mathrm{d}y} = \frac{5}{32\nu}\frac{y^{-6}}{1+7e^2/8}, \qquad (160a)$$

$$\frac{\mathrm{d}\delta\lambda}{\mathrm{d}y} = \frac{15}{32\nu}\frac{y^{-4}}{1 + 7e^2/8}\,. \tag{160b}$$

Neglecting $\mathcal{O}\left(e^2\right)$ terms, and integrating from y_0 to coalescence, the accumulated phases are

$$\lambda = \frac{1}{32\nu}y_0^{-5}\left(1 + \mathcal{O}\left(e_0^2\right)\right) \tag{161a}$$

$$\approx \frac{1}{32}\left(\frac{G\mathcal{M}_c\pi f_{\min}}{c^3}\right)^{-5/3}, \tag{161b}$$

$$\delta\lambda = \frac{5}{32\nu}y_0^{-3}\left(1 + \mathcal{O}\left(e_0^2\right)\right) \tag{161c}$$

$$\approx \frac{5}{32}\nu^{-2/5}\left(\frac{G\mathcal{M}_c\pi f_{\min}}{c^3}\right)^{-1}. \tag{161d}$$

For typical parameter values the approximate number of accumulated orbital cycles $\mathcal{N}_{\mathrm{orb}}$ and periastron advance cycles $\mathcal{N}_{\mathrm{ecc}}$ are given by

$$\mathcal{N}_{\mathrm{orb}} = \frac{\lambda}{2\pi} \approx 3500\left(\frac{\mathcal{M}_c}{M_\odot}\right)^{-5/3}\left(\frac{f_{\min}}{20\,\mathrm{Hz}}\right)^{-5/3}, \tag{162a}$$

$$\mathcal{N}_{\mathrm{ecc}} = \frac{\delta\lambda}{2\pi} \approx 140\left(\frac{\nu}{1/4}\right)^{-2/5}\left(\frac{\mathcal{M}_c}{M_\odot}\right)^{-1}\left(\frac{f_{\min}}{20\,\mathrm{Hz}}\right)^{-1}. \tag{162b}$$

For the injected binary system, this yields $\mathcal{N}_{\mathrm{orb}} = 497$ and $\mathcal{N}_{\mathrm{ecc}} = 58$. Therefore, from Eq. (162a), $\mathcal{M}_c$ can be determined with sub-percent level accuracy from tracking the orbital phase λ with $\mathcal{O}\left(1\right)$ precision. Likewise, since $\delta\lambda$ is proportional to $\nu^{-2/5}$ (Eq. (162b)), the symmetric mass ratio can be determined with percent level accuracy if we measure $\delta\lambda$ with $\mathcal{O}\left(1\right)$ precision, as is the case when higher-order Fourier modes are observed.

In Fig. 14 we also find that $\mathcal{M}_c$, q, e_0 and χ_{eff} are correlated as they dominate the phase evolution of the binary during the inspiral. On the other hand, χ_{p} seems to be largely uncorrelated with the other parameters, since the effect of precession approximately decouples from the inspiral rate [89], modulating the amplitude with little secular impact on the phase. It is particularly noteworthy that e_0 and χ_p do not seem to be strongly correlated, suggesting that eccentricity and precession can be independently constrained. Both effects produce amplitude modulations (see e.g. Fig. 4), with eccentricity modulations occurring on the orbital timescale. For high-mass systems, where only the final inspiral cycles and the merger-ringdown are observed, the orbital and spin-precession time-scales are of similar order, and the effects of eccentricity and precession might be more difficult to disentangle [26]. However, for low-mass binaries, we find that the orbital and spin-precession time-scales are cleanly separated, suggesting that the two effects are distinguishable. Furthermore, as previously argued, for low-mass systems with many cycles in the detector sensitivity band, eccentricity is primarily constrained by its impact on the binary phase, while precession leaves the phase largely unaffected [89].

2. Precessing quasi-circular injection

Next, we assess whether pyEFPE accurately recovers the parameters of a precessing, quasi-circular binary, in particular $e_0 = 0$. For the injection we use the inspiral-merger-ringdown waveform model IMRPhenomXP [125, 144] described in Sec. VII A 3

In particular, we perform two binary black hole (BBH) IMRPhenomXP injections with detector-frame masses of $m_1 = 10M_\odot$ and $m_2 = 5M_\odot$, consistent with the low mass end of the observed BBH population [11]. We analyze 16 s of data up to a maximum frequency of 250 Hz, i.e. $f_{\max} \approx 0.85 f_{\mathrm{ISCO}}$. All parameters of the two injections are identical except for the luminosity distance, allowing us to explore signals with different SNRs. The "low SNR" injection has $d_L = 2000$ Mpc and an SNR of 12.7, typical of the bulk of events observed by GW detectors [6], while the "high SNR" has $d_L = 1000$ Mpc and SNR of 25.5. We recover each zero-noise injection with three different signal models:

- IMRPhenomXP, which is the same model as used for the injection, and therefore gives the baseline result.

- pyEFPE with a flat prior for the initial eccentricity $e_0 \in [0, 0.4]$.

- pyEFPE, where we fix the initial eccentricity $e_0 = 0$, to more closely resemble the configuration of the IMRPhenomXP run and to isolate differences pertaining to differences in the non-eccentric sector.

Figure 15 shows the posterior distributions of the most important intrinsic parameters, together with the injected values, for both SNRs and all three waveform models. We refer the reader to appendix F for the complete results. We find that the posterior distributions generally agree with the injected values. However, even in the IMRPhenomXP recovery, the posteriors are not Gaussian distributions centered at the injected values, and exhibit noticeable biases. These deviations arise from prior effects and correlations between parameters [121, 173, 174]. Nevertheless, the overall shape of the posteriors is broadly consistent between the different approximants, with small differences in the inferred values of $\mathcal{M}_c$ and χ_{eff} that become more noticeable at higher SNR (right panel).

The most striking difference we observe concerns the chirp mass recovered by pyEFPE, which is significantly lower than the injected value. However, this is expected since the chirp mass and eccentricity are degenerate, both appearing at 0PN order in the phase. This degeneracy can be captured by an eccentric chirp mass $\mathcal{M}_c^{\mathrm{ecc}}$ [175], which at $\mathcal{O}\left(e_0^2\right)$ can be computed as [3]

————

[3] Note that Ref. [175] defines $\mathcal{M}_c^{\mathrm{ecc}} = \mathcal{M}_c/\left(1 - \frac{157}{24}e_0^2\right)^{3/5}$. This

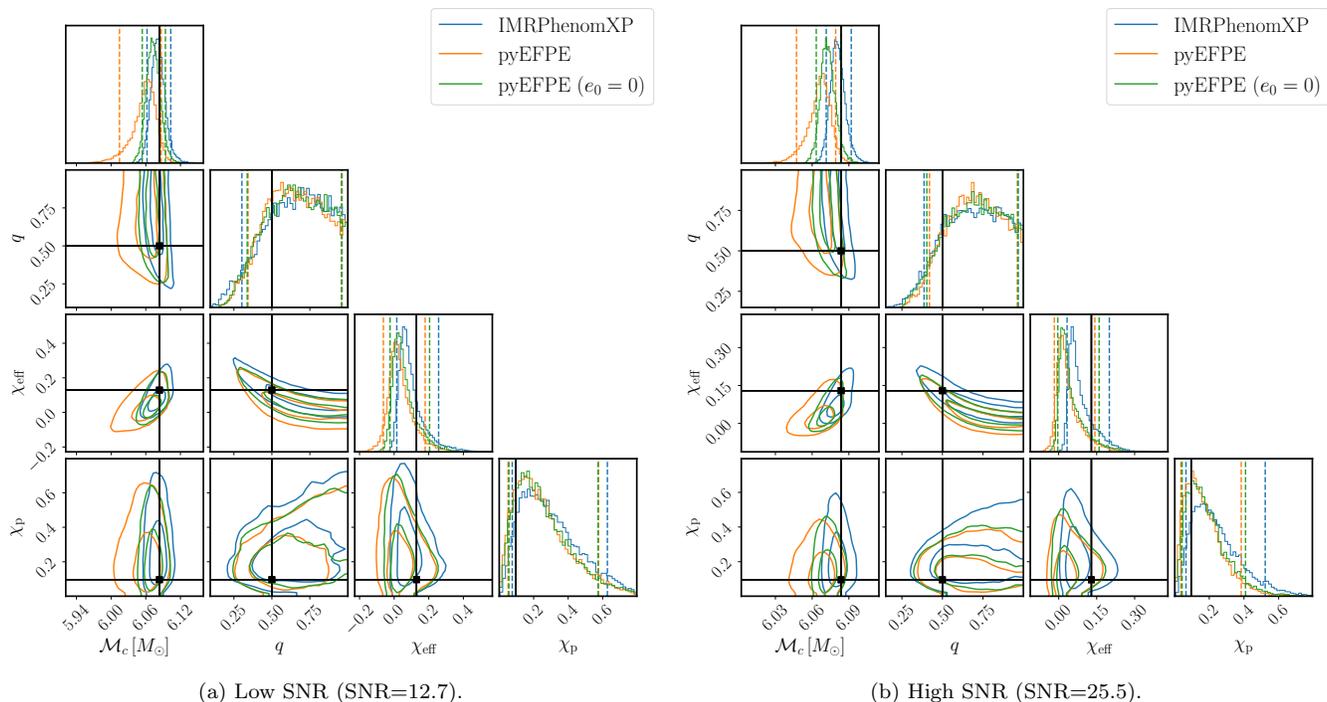(a) Low SNR (SNR=12.7).

(b) High SNR (SNR=25.5).

FIG. 15: Corner plot showing the joint posterior distributions of the most important intrinsic parameters of the `IMRPhenomXP` injection recovered with `IMRPhenomXP`, `pyEFPE` and `pyEFPE` with $e_0 = 0$ for the low SNR case (left panel) and high SNR case (right panel). Specifically, the plot displays the chirp mass $\mathcal{M}_c$, mass ratio q effective inspiral spin parameter χ_{eff} and effective precession spin parameter χ_{p}. In each corner plot, the diagonal panels display the marginal distributions for each parameter, along with the 90% confidence interval. The off-diagonal panels show the bivariate correlations between pairs of parameters, with the contours representing the 50% and 90% confidence regions. The black lines mark the values of the injected parameters.

$$\mathcal{M}_c^{\mathrm{ecc}} = \left(1 + \frac{157}{40} e_0^2\right)\mathcal{M}_c. \qquad (163)$$

Figure 16 shows the posteriors for the eccentric chirp mass $\mathcal{M}_c^{\mathrm{ecc}}$, the regular chirp mass $\mathcal{M}_c$ and the initial eccentricity e_0 for the `pyEFPE` low and high SNR injections. We observe that the eccentricity posteriors for both runs strongly support a quasi-circular binary ($e_0 = 0$), and have tails extending to $e_0 < 0.09$ and $e_0 < 0.06$ for the low and high SNR case, respectively. The aforementioned anti-correlation between e_0 and $\mathcal{M}_c$ is evident in the 2D posterior: To fit the injected signal, non-zero eccentricity is compensated by a lower chirp mass, ultimately leaving the injected chirp mass outside of the 1D 90% credible interval. On the other hand, when using the eccentric chirp mass of Eq. (163), this degeneracy is significantly reduced and the recovered median value of $\mathcal{M}_c^{\mathrm{ecc}}$ agrees with the injected value.

Going back to Fig. 15, we again observe that, even in the case where the initial eccentricity is fixed to $e_0 = 0$,

the `pyEFPE` $\mathcal{M}_c$ and χ_{eff} posteriors still differ slightly from the `IMRPhenomXP` ones, specially in the high SNR case. These disagreements are due to differences in the models that, as discussed in Sec. VII A 3, lead to differences in their predictions. To explore these waveform systematics in more detail, we perform two more analyses on both injections, using the `SpinTaylorT4` waveform with different amounts of PN information. In both analyses the amplitude of the GWs is modeled at 0PN and the spinning terms of the equations of motion are taken to 3PN, the maximum available in the `lalsuite` [138] implementation used. However, in one run we limit the non-spinning terms to 3PN, the same order used in `pyEFPE`, and in the other to the maximum 3.5PN allowed in `lalsuite`.

In Fig. 17 we show the posteriors for $\mathcal{M}_c$ and χ_{eff} for the four quasi-circular analyses. Looking at the low SNR case in Fig. 17a, the `pyEFPE` run with $e_0 = 0$ and the `SpinTaylorT4` run at 3PN agree very well with each other, while the `IMRPhenomXP` run and the `SpinTaylorT4` run at 3.5PN are also in very good agreement with each other. This highlights the importance of including higher-order PN terms in the waveform. For the high SNR case shown in Fig. 17b, the `pyEFPE` run with $e_0 = 0$ and the `SpinTaylorT4` run at 3PN, and the `IMRPhenomXP` run and the `SpinTaylorT4` run at 3.5PN

---

definition is problematic, since it has a divergence at $e_0 = \sqrt{24/157} \approx 0.39$. Given that it was derived using formulas accurate up to $\mathcal{O}(e^2)$, it is preferable to use the $\mathcal{O}(e_0^2)$ expansion of Eq. (163).
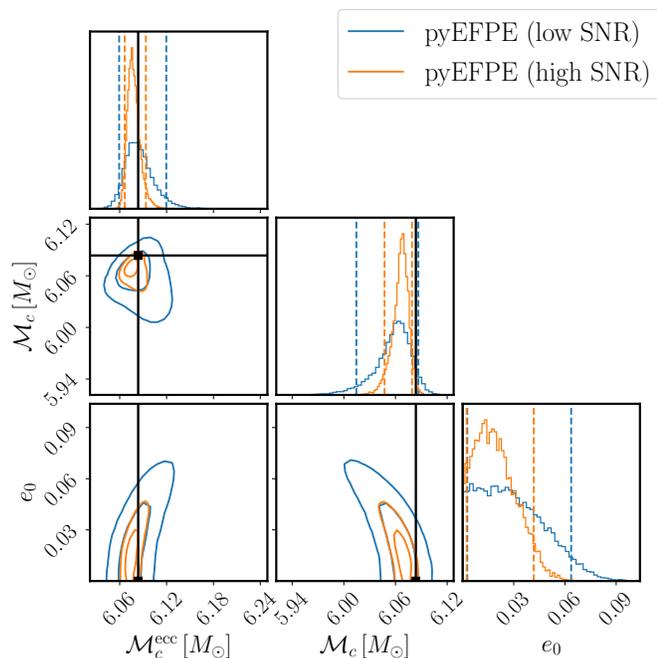
FIG. 16: Corner plot showing the joint and marginalised 1D posterior distributions of the eccentric chirp mass $\mathcal{M}_c^{\text{ecc}}$, chirp mass $\mathcal{M}_c$ and initial eccentricity e_0 for the `IMRPhenomXP` injection recovered with `pyEFPE` for the low SNR (blue) and high SNR (orange) cases. The dashed vertical lines mark the 90% confidence interval. The contours for the 2D posteriors represent the 50% and 90% confidence regions. The black lines mark the injected values.

are still clustered into pairs, however, we note that in this case there are bigger differences due to small differences in the models discussed in Sec. VII A 3. The most important differences are: i) the different PN information included in the precession equations of each model (3PN for `SpinTaylorT4` and 2PN for `pyEFPE`), ii) the difference between the SUA and FFT to compute the frequency-domain waveforms and iii) the residual eccentricity of Eq. (85) taken into account by `pyEFPE`.

VIII.   CONCLUSION

In this paper we have introduced `pyEFPE`, a post-Newtonian waveform model for the inspiral of spin-precessing compact binaries on eccentric orbits. `pyEFPE` improves upon previous EFPE models available in the literature [72–74] by i) introducing closed-form analytical expressions for the Newtonian Fourier mode amplitudes (Sec. II), ii) improving the numerical stability of the MSA approximation (Sec. III), iii) extending the PN information in the equations of motion (Sec. IV and Appendix B) and iv) providing an optimized and simple numerical implementation (Sec. VI). In addition, we introduced a scheme to interpolate the slow-varying waveform amplitudes, enabling a speedup of the waveform generation by

a factor of $\sim \mathcal{O}(20)$ with minimal loss of accuracy, making the model well-suited for real data analysis applications. The `pyEFPE` waveform will be made publicly available at https://github.com/gmorras/pyEFPE, with a `Python` implementation designed to be easy to modify and use to make it as useful as possible for the scientific community.

In Sec. VII, we thoroughly validated the `pyEFPE` waveform: First, we checked the phenomenology of inspiral waveforms with spin-precession and orbital eccentricity. As no other widely available frequency-domain waveform model includes both effects, we then performed mismatch comparisons between `pyEFPE` and other waveforms in the quasi-circular limit (`SpinTaylorT4`, `IMRPhenomXP`, and `TaylorF2`) and the eccentric, spin-aligned limit (`TaylorF2Ecc`), finding good agreement overall. Finally, we demonstrated the efficacy of `pyEFPE` to perform full Bayesian inference on simulated GW data in current ground-based GW detector networks, and to recover the parameters of signals described by `pyEFPE` and `IMRPhenomXP`. This makes `pyEFPE` a powerful tool for GW science, enabling the study of inspiral signals with both spin-precession and orbital eccentricity, which are considered critical features for understanding the formation and evolution of compact binaries [9, 12, 18]. Integrating `pyEFPE` into LISA data analysis pipelines [176–179] will be a key goal, with the inference of stellar mass binaries and intermediate mass ratio inspirals being core components of the global fit [37]. Whilst only a handful of stellar mass binaries are expected [180], LISA may be able to resolve a handful of low-redshift sources with high precision, providing valuable insight into the degree of orbital eccentricity and spin-precession in the population at low frequencies.

While `pyEFPE` represents a significant advancement in waveform modeling, it still omits several physical effects present in the inspiral of compact binaries, such as higher-order modes [125], mode asymmetries [102, 181] or tidal effects [182–186]. Additionally, as highlighted in Sec. VII, higher-order PN terms in the equations of motion are required to accurately describe very high SNR signals, particularly for binaries with highly unequal mass ratios or large anti-aligned spins. We leave the incorporation of these effects into `pyEFPE` for future work.

The final major component missing in `pyEFPE` is the merger-ringdown phase of the waveform, where the PN expansion is no longer applicable. As demonstrated in recent phenomenological models (see e.g. Refs. [125, 144]), the merger-ringdown regime can be accurately modeled by fitting physically motivated ansätze to numerical relativity simulations. Integrating such a calibrated model into `pyEFPE`'s description of the inspiral phase would represent a significant step toward constructing a computationally efficient inspiral-merger-ringdown waveform model for spin-precessing, eccentric binaries. In this regard, `pyEFPE` offers a new avenue towards the construction of complete and computationally efficient inspiral-merger-ringdown waveforms for compact binaries with
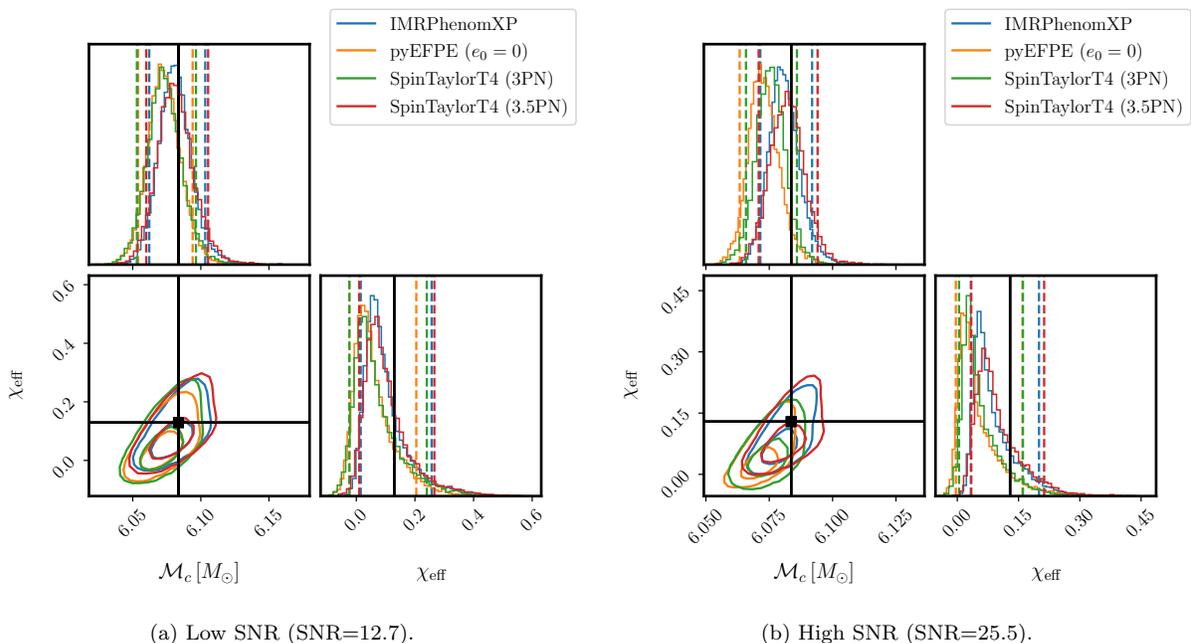
(a) Low SNR (SNR=12.7).

(b) High SNR (SNR=25.5).

FIG. 17: Corner plot showing the joint posterior distributions of the chirp mass $\mathcal{M}_c$ and effective inspiral spin parameter χ_{eff} for the `IMRPhenomXP` injection recovered with `IMRPhenomXP`, `pyEFPE` with $e_0 = 0$, and `SpinTaylorT4` taking up to 3PN and 3.5PN terms in the non-spinning part of the evolution equations. In the left panel we plot the low SNR case and in the right panel the high SNR case. In each corner plot, the diagonal panels display the marginal distributions for each parameter, along with the 90% confidence interval. The off-diagonal panel shows the bivariate correlations between the two parameters, with the contours representing the 50% and 90% confidence regions. The black lines mark the values of the injected parameters.

orbital eccentricity and spin precession.

Appendix A: Comparison of Newtonian Fourier Mode Amplitudes

In Sec. II, we outlined a derivation of the Newtonian Fourier mode amplitudes in terms of exact closed-form analytical expressions involving Bessel functions, denoted $N_j^{22,\text{ex.}}$. A solution for the Fourier mode amplitudes was previously derived in [74], based on nested series expansions that build on earlier work in [48, 73]. We denote the amplitudes estimated this way as $N_j^{22,\text{pert.}}$, where we explicitly follow the recommended truncation of the summation as outlined in [74]. In Fig. 18 we demonstrate agreement between the two methods, with the maximum relative errors being $\sim \mathcal{O}(10^{-2})$. As would be expected, the errors degrade with eccentricity, as ever more terms in the series are required to accurately reproduce the exact solution. Likewise, the apparent discontinuities as a function of j are due to the finite truncation of the nested summation operations.
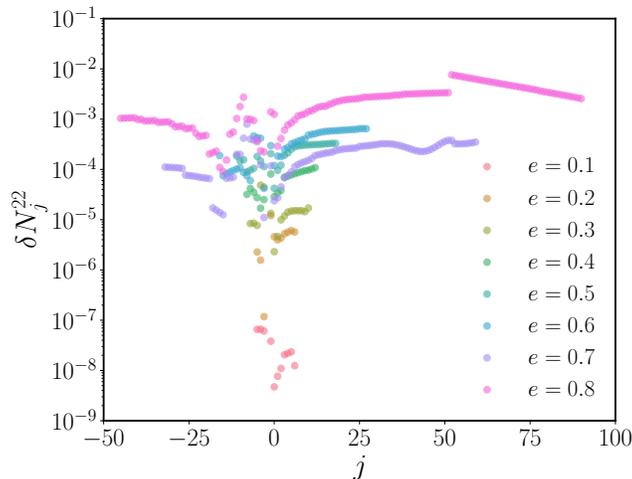
FIG. 18: Here we show the relative error between the exact solution $N_j^{22,\text{ex.}}$, corresponding to Eq. (31), and the perturbative solution $N_j^{22,\text{pert.}}$ derived in [74], where $\delta N_j^{22} = |(N_j^{22,\text{ex.}} - N_j^{22,\text{pert.}})/N_j^{22,\text{ex.}}|$. We explore the approximation error over the range of j required to accurately reconstruct the Fourier mode amplitudes for a range of eccentricities.

Appendix B: Expressions for the evolution equations

In this work we use harmonic coordinates (HC) and the covariant Tulczyjew-Dixon spin-supplementary condition [187, 188].

1. Evolution of y and e^2

We obtain the non-spinning evolution of y and e^2 from the evolution of $x = (1 - e^2)y^2 = (M\omega)^{2/3}$ and e, given in Ref. [189]. As was noted in Ref. [114], Ref. [189] has an error in the expression for de/dt, coming from the fact that they obtained it by just transforming the eccentricity from ADM to harmonic coordinates (i.e. $e^{\text{ADM}} \to e^{\text{HC}}$), but one also has to transform $de^{\text{ADM}}/dt \to de^{\text{HC}}/dt$, since the derivative is not gauge invariant. Note that we do not take the formulas for dx/dt from Ref. [114], as although they indicate these are given in harmonic coordinates, there appears to be a discrepancy, potentially involving the use of ADM expressions instead. When using the updated formulae, the expressions for a_4 and a_6 simplify, since there are now no terms proportional to $1/(1 - e^2)$.

We use the approximation of the enhancement functions presented in Ref. [72], written in a way that improves convergence, due to the inclusion of factors of $\sqrt{1 - e^2}$. Similarly, as in Ref. [72], we include in the 3PN enhancement functions κ_i only the terms proportional to $\log(n)$, as the other ones are in finite number and can be combined with non-tail terms.

For the spinning contributions, we use the 1.5PN and 2PN fully-spinning terms from Ref. [72], correcting a typo found when comparing with Ref. [53], where we note that in the coefficient of b_4^{SS} multiplying $(\hat{\boldsymbol{L}} \cdot \boldsymbol{s}_2)^2$, an $111/4$ should be replaced by an $111/2$. For eccentric-spin-aligned binaries, the spin-spin and spin-orbit phasing coefficients to 3PN were recently found in Ref. [53]. We include these coefficients in our waveform model, making it accurate up to 3PN in spin, ignoring the perpendicular-in-spin contributions to the 3PN spin-spin terms.

We write the evolution equations for y and e^2 as

$$\mathcal{D}y = \nu y^9 \left(a_0 + \sum_{n=2}^{6} a_n y^n \right), \tag{B1a}$$

$$\mathcal{D}e^2 = -\nu y^8 \left(b_0 + \sum_{n=2}^{6} b_n y^n \right), \tag{B1b}$$

At 3PN order, the non-spinning (NS) part of the coefficients is given by:

$$a_0 = \frac{32}{5} + \frac{28}{5}e^2\,, \tag{B2a}$$

$$a_2 = -\frac{1486}{105} - \frac{88}{5}\nu + \left(\frac{12296}{105} - \frac{5258}{45}\nu\right)e^2 + \left(\frac{3007}{84} - \frac{244}{9}\nu\right)e^4\,, \tag{B2b}$$

$$a_3^{\mathrm{NS}} = \frac{128\pi}{5}\phi_y\,, \tag{B2c}$$

$$a_4^{\mathrm{NS}} = \frac{34103}{2835} + \frac{13661}{315}\nu + \frac{944}{45}\nu^2 + \left(-\frac{489191}{1890} - \frac{209729}{630}\nu + \frac{147443}{270}\nu^2\right)e^2 + \left(\frac{2098919}{7560} - \frac{2928257}{2520}\nu + \frac{34679}{45}\nu^2\right)e^4$$
$$+ \left(\frac{53881}{2520} - \frac{7357}{90}\nu + \frac{9392}{135}\nu^2\right)e^6 + \frac{1 - \sqrt{1 - e^2}}{\sqrt{1 - e^2}}\left[16 - \frac{32}{5}\nu + \left(266 - \frac{532}{5}\nu\right)e^2 + \left(-\frac{859}{2} + \frac{859}{5}\nu\right)e^4\right.$$
$$\left. + \left(-65 + 26\nu\right)e^6\right]\,, \tag{B2d}$$

$$a_5^{\mathrm{NS}} = \pi\left(-\frac{4159}{105}\psi_y - \frac{756}{5}\nu\zeta_y\right)\,, \tag{B2e}$$

$$a_6^{\mathrm{NS}} = \frac{16447322263}{21829500} - \frac{54784}{525}\gamma_E + \frac{512}{15}\pi^2 + \left(-\frac{56198689}{34020} + \frac{902}{15}\pi^2\right)\nu + \frac{541}{140}\nu^2 - \frac{1121}{81}\nu^3 + \left[\frac{33232226053}{10914750}\right.$$
$$- \frac{392048}{525}\gamma_E + \frac{3664}{15}\pi^2 + \left(-\frac{588778}{1701} + \frac{2747}{40}\pi^2\right)\nu - \frac{846121}{1260}\nu^2 - \frac{392945}{324}\nu^3\right]e^2 + \left[-\frac{227539553251}{58212000} - \frac{93304}{175}\gamma_E\right.$$
$$+ \frac{872}{5}\pi^2 + \left(\frac{124929721}{12960} - \frac{41287}{960}\pi^2\right)\nu + \frac{148514441}{30240}\nu^2 - \frac{2198212}{405}\nu^3\right]e^4 + \left[-\frac{300856627}{67375} - \frac{4922}{175}\gamma_E + \frac{46}{5}\pi^2\right.$$
$$+ \left(\frac{1588607}{432} - \frac{369}{80}\pi^2\right)\nu + \frac{12594313}{3780}\nu^2 - \frac{44338}{15}\nu^3\right]e^6 + \left(-\frac{243511057}{887040} + \frac{4179523}{15120}\nu + \frac{83701}{3780}\nu^2 - \frac{1876}{15}\nu^3\right)e^8$$
$$+ \frac{1 - \sqrt{1 - e^2}}{\sqrt{1 - e^2}}\left\{-\frac{616471}{1575} + \left(\frac{9874}{315} - \frac{41}{30}\pi^2\right)\nu + \frac{632}{15}\nu^2 + \left[\frac{2385427}{1050} + \left(-\frac{274234}{45} + \frac{4223}{240}\pi^2\right)\nu + \frac{70946}{45}\nu^2\right]e^2\right.$$
$$+ \left[\frac{8364697}{4200} + \left(\frac{1900517}{630} - \frac{32267}{960}\pi^2\right)\nu - \frac{47443}{90}\nu^2\right]e^4 + \left[-\frac{167385119}{25200} + \left(\frac{4272491}{504} - \frac{123}{160}\pi^2\right)\nu - \frac{43607}{18}\nu^2\right]e^6$$
$$+ \left(-\frac{65279}{168} + \frac{510361}{1260}\nu - \frac{5623}{45}\nu^2\right)e^8\right\} + \frac{1284}{175}\kappa_y$$
$$+ \left(\frac{54784}{525} + \frac{392048}{525}e^2 + \frac{93304}{175}e^4 + \frac{4922}{175}e^6\right)\log\left[\frac{1 + \sqrt{1 - e^2}}{8y\left(1 - e^2\right)^{3/2}}\right]\,, \tag{B2f}$$

$$b_0 = \frac{608}{15}e^2 + \frac{242}{15}e^4\,, \tag{B2g}$$

$$b_2 = \left(-\frac{1878}{35} - \frac{8168}{45}\nu\right)e^2 + \left(\frac{59834}{105} - \frac{7753}{15}\nu\right)e^4 + \left(\frac{13929}{140} - \frac{3328}{45}\nu\right)e^6\,, \tag{B2h}$$

$$b_3^{\mathrm{NS}} = \frac{788\pi e^2}{3}\phi_e\,, \tag{B2i}$$

$$b_4^{\mathrm{NS}} = \left(-\frac{949877}{945} + \frac{18763}{21}\nu + \frac{1504}{5}\nu^2\right)e^2 + \left(-\frac{3082783}{1260} - \frac{988423}{420}\nu + \frac{64433}{20}\nu^2\right)e^4 + \left(\frac{23289859}{7560} - \frac{13018711}{2520}\nu\right.$$
$$+ \frac{127411}{45}\nu^2\right)e^6 + \left(\frac{420727}{1680} - \frac{362071}{1260}\nu + \frac{1642}{9}\nu^2\right)e^8 + \sqrt{1 - e^2}\left[\left(\frac{2672}{3} - \frac{5344}{15}\nu\right)e^2 + \left(2321 - \frac{4642}{5}\nu\right)e^4\right.$$
$$\left. + \left(\frac{565}{3} - \frac{226}{3}\nu\right)e^6\right]\,, \tag{B2j}$$

$$b_5^{\mathrm{NS}} = \pi\left(-\frac{55691}{105}\psi_e - \frac{610144}{315}\nu\zeta_e\right)e^2\,, \tag{B2k}$$

$$b_6^{\mathrm{NS}} = \left[\frac{61669369961}{4365900} - \frac{2633056}{1575}\gamma_E + \frac{24608}{45}\pi^2 + \left(\frac{50099023}{56700} + \frac{779}{5}\pi^2\right)\nu - \frac{4088921}{1260}\nu^2 - \frac{61001}{243}\nu^3\right]e^2$$

$$+ \left[\frac{66319591307}{21829500} - \frac{9525568}{1575} \gamma_E + \frac{89024}{45} \pi^2 + \left(\frac{28141879}{450} - \frac{139031}{480} \pi^2 \right) \nu - \frac{21283907}{1512} \nu^2 - \frac{86910509}{9720} \nu^3 \right] e^4$$

$$+ \left[-\frac{1149383987023}{58212000} - \frac{4588588}{1575} \gamma_E + \frac{42884}{45} \pi^2 + \left(\frac{11499615139}{453600} - \frac{271871}{960} \pi^2 \right) \nu + \frac{61093675}{2016} \nu^2 - \frac{2223241}{90} \nu^3 \right] e^6$$

$$+ \left[\frac{40262284807}{4312000} - \frac{20437}{175} \gamma_E + \frac{191}{5} \pi^2 + \left(-\frac{5028323}{280} - \frac{6519}{320} \pi^2 \right) \nu + \frac{24757667}{1260} \nu^2 - \frac{11792069}{1215} \nu^3 \right] e^8$$

$$+ \left(\frac{302322169}{887040} - \frac{1921387}{5040} \nu + \frac{41179}{108} \nu^2 - \frac{386792}{1215} \nu^3 \right) e^{10} + \sqrt{1-e^2} \left\{ \left[-\frac{22713049}{7875} + \left(-\frac{11053982}{945} + \frac{8323}{90} \pi^2 \right) \nu \right. \right.$$

$$+ \frac{108664}{45} \nu^2 \bigg] e^2 + \left[\frac{178791374}{7875} + \left(-\frac{38295557}{630} + \frac{94177}{480} \pi^2 \right) \nu + \frac{681989}{45} \nu^2 \right] e^4 + \left[\frac{5321445613}{189000} \right.$$

$$+ \left(-\frac{26478311}{756} + \frac{2501}{1440} \pi^2 \right) \nu + \frac{450212}{45} \nu^2 \bigg] e^6 + \left[\frac{186961}{168} - \frac{289691}{252} \nu + \frac{3197}{9} \nu^2 \right] e^8 \bigg\} + \frac{1460336}{23625} \left(1 - \sqrt{1-e^2} \right)$$

$$+ \frac{428}{1575} e^2 \kappa_e + \left(\frac{2633056}{1575} e^2 + \frac{9525568}{1575} e^4 + \frac{4588588}{1575} e^6 + \frac{20437}{175} e^8 \right) \log \left[\frac{1 + \sqrt{1-e^2}}{8y \left(1-e^2 \right)^{3/2}} \right], \tag{B2l}$$

where the tail terms are given by [72]

$$\phi_y = \left(1 - e^2 \right)^{7/2} \tilde{\phi}$$
$$= 1 + \frac{97}{32} e^2 + \frac{49}{128} e^4 - \frac{49}{18432} e^6 - \frac{109}{147456} e^8 - \frac{2567}{58982400} e^{10} + \mathcal{O} \left(e^{12} \right), \tag{B3a}$$

$$\phi_e = \frac{192 \left(1 - e^2 \right)^{9/2}}{985 e^2} \left(\sqrt{1-e^2} \phi - \tilde{\phi} \right)$$
$$= 1 + \frac{5969}{3940} e^2 + \frac{24217}{189120} e^4 + \frac{623}{4538880} e^6 - \frac{96811}{363110400} e^8 - \frac{5971}{4357324800} e^{10} + \mathcal{O} \left(e^{12} \right), \tag{B3b}$$

$$\psi_y = \left(1 - e^2 \right)^{9/2} \left(-\frac{8064}{4159} \sqrt{1-e^2} \phi + \frac{4032}{4159} \tilde{\phi} + \frac{8191}{4159} \tilde{\psi} \right)$$
$$= 1 - \frac{207671}{8318} e^2 - \frac{8382869}{266176} e^4 - \frac{8437609}{4791168} e^6 + \frac{10075915}{306634752} e^8 - \frac{38077159}{15331737600} e^{10} + \mathcal{O} \left(e^{12} \right), \tag{B3c}$$

$$\zeta_y = \left(1 - e^2 \right)^{7/2} \left[\frac{160 \left(1 - e^2 \right)^{3/2}}{567} \phi + \left(-\frac{176}{567} + \frac{80}{567} e^2 \right) \tilde{\phi} + \frac{583 \left(1 - e^2 \right)}{567} \tilde{\zeta} \right]$$
$$= 1 + \frac{113002}{11907} e^2 + \frac{6035543}{762048} e^4 + \frac{253177}{571536} e^6 - \frac{850489}{877879296} e^8 - \frac{1888651}{10973491200} e^{10} + \mathcal{O} \left(e^{12} \right), \tag{B3d}$$

$$\psi_e = \frac{16382 \left(1 - e^2 \right)^{9/2}}{55691 e^2} \left[\left(\frac{9408}{8191} - \frac{14784}{8191} e^2 \right) \sqrt{1-e^2} \phi + \left(-\frac{9408}{8191} + \frac{4032}{8191} e^2 \right) \tilde{\phi} + \left(1 - e^2 \right) \left(\sqrt{1-e^2} \psi - \tilde{\psi} \right) \right]$$
$$= 1 - \frac{9904271}{891056} e^2 - \frac{101704075}{10692672} e^4 - \frac{217413779}{513248256} e^6 + \frac{35703577}{6843310080} e^8 - \frac{3311197679}{9854366515200} e^{10} + \mathcal{O} \left(e^{12} \right), \tag{B3e}$$

$$\zeta_e = \frac{12243 \left(1 - e^2 \right)^{9/2}}{76268 e^2} \left[-\frac{16 \left(1 - e^2 \right)^{3/2}}{53} \phi + \left(\frac{16}{53} - \frac{80}{583} e^2 \right) \tilde{\phi} + \left(1 - e^2 \right) \left(\sqrt{1-e^2} \zeta - \tilde{\zeta} \right) \right]$$
$$= 1 + \frac{11228233}{2440576} e^2 + \frac{37095275}{14643456} e^4 + \frac{151238443}{1405771776} e^6 - \frac{118111}{611205120} e^8 - \frac{407523451}{26990818099300} e^{10} + \mathcal{O} \left(e^{12} \right), \tag{B3f}$$

$$\kappa_y = -\frac{934088 \left(1 - e^2 \right)^5}{33705} \left(\tilde{\kappa} - \tilde{F} \right)$$
$$= 244 \log 2 \left(e^2 - \frac{18881}{1098} e^4 + \frac{6159821}{39528} e^6 - \frac{16811095}{19764} e^8 + \frac{446132351}{123525} e^{10} \right) - 243 \log 3 \left(e^2 - \frac{39}{4} e^4 + \frac{2735}{64} e^6 \right.$$
$$+ \frac{25959}{512} e^8 - \frac{638032239}{409600} e^{10} \bigg) - \frac{48828125 \log 5}{5184} \left(e^6 - \frac{83}{8} e^8 + \frac{12637}{256} e^{10} \right) - \frac{4747561509943 \log 7}{33177600} e^{10} + \mathcal{O} \left(e^{12} \right), \tag{B3g}$$

$$\kappa_e = -\frac{5604528 \left(1 - e^2 \right)^6}{3745 e^2} \left[\sqrt{1-e^2} \left(\kappa - F \right) - \left(\tilde{\kappa} - \tilde{F} \right) \right]$$

$$=6536\log 2\left(1-\frac{22314}{817}e^2+\frac{7170067}{19608}e^4-\frac{10943033}{4128}e^6+\frac{230370959}{15480}e^8-\frac{866124466133}{8823600}e^{10}\right)$$

$$-6561\log 3\left(1-\frac{49}{4}e^2+\frac{4369}{64}e^4+\frac{214449}{512}e^6-\frac{623830739}{81920}e^8+\frac{76513915569}{1638400}e^{10}\right)$$

$$-\frac{48828125\log 5}{64}\left(e^4-\frac{293}{24}e^6+\frac{159007}{2304}e^8-\frac{6631171}{27648}e^{10}\right)-\frac{4747561509943\log 7}{245760}\left(e^8-\frac{259}{20}e^{10}\right)+\mathcal{O}\left(e^{12}\right).$$

$$\text{(B3h)}$$

The spin-orbit (SO) terms can be found in Refs. [53, 72], and in terms of $\chi_{\rm eff}$ (Eq. 43) and $\delta\chi$ (Eq. 45) they are given by:

$$a_3^{\rm SO}=\left(-\frac{752}{15}-138e^2-\frac{611}{30}e^4\right)\chi_{\rm eff}+\left(-\frac{152}{15}-\frac{154}{15}e^2+\frac{17}{30}e^4\right)\delta\mu\delta\chi\,,\qquad\text{(B4a)}$$

$$a_5^{\rm SO}=\left[-\frac{5861}{45}+\frac{4004}{15}\nu+\left(-\frac{968539}{630}+\frac{259643}{135}\nu\right)e^2+\left(-\frac{4856917}{2520}+\frac{943721}{540}\nu\right)e^4+\left(-\frac{64903}{560}+\frac{5081}{45}\nu\right)e^6\right.$$

$$+\frac{e^2}{\sqrt{1-e^2}}\left(-\frac{1416}{5}+\frac{1652}{15}\nu+\left(\frac{2469}{5}-\frac{5761}{30}\nu\right)e^2+\left(\frac{222}{5}-\frac{259}{15}\nu\right)e^4\right)\Bigg]\chi_{\rm eff}$$

$$+\left[-\frac{21611}{315}+\frac{632}{15}\nu+\left(-\frac{55415}{126}+\frac{36239}{135}\nu\right)e^2+\left(-\frac{72631}{360}+\frac{12151}{108}\nu\right)e^4+\left(\frac{909}{560}-\frac{143}{45}\nu\right)e^6\right.$$

$$+\frac{e^2}{\sqrt{1-e^2}}\left(-\frac{472}{5}+\frac{236}{15}\nu+\left(\frac{823}{5}-\frac{823}{30}\nu\right)e^2+\left(\frac{74}{5}-\frac{37}{15}\nu\right)e^4\right)\Bigg]\delta\mu\delta\chi\,,\qquad\text{(B4b)}$$

$$a_6^{\rm SO}=-\frac{3008}{15}\pi\theta_{y\chi}\chi_{\rm eff}-\frac{592}{15}\pi\theta_{y\delta}\delta\mu\delta\chi\,,\qquad\text{(B4c)}$$

$$b_3^{\rm SO}=e^2\left(-\frac{3272}{9}-\frac{26263}{45}e^2-\frac{812}{15}e^4\right)\chi_{\rm eff}+e^2\left(-\frac{3328}{45}-\frac{1993}{45}e^2+\frac{23}{15}e^4\right)\delta\mu\delta\chi\,,\qquad\text{(B4d)}$$

$$b_5^{\rm SO}=e^2\left[-\frac{13103}{35}+\frac{289208}{135}\nu+\left(-\frac{548929}{63}+\frac{61355}{6}\nu\right)e^2+\left(-\frac{6215453}{840}+\frac{1725437}{270}\nu\right)e^4+\left(-\frac{87873}{280}+\frac{13177}{45}\nu\right)e^6\right.$$

$$+\sqrt{1-e^2}\left(-1184+\frac{4144}{9}\nu+\left(-\frac{13854}{5}+\frac{16163}{15}\nu\right)e^2+\left(-\frac{626}{5}+\frac{2191}{45}\nu\right)e^4\right)\Bigg]\chi_{\rm eff}$$

$$+e^2\left[-\frac{32857}{105}+\frac{52916}{135}\nu+\left(-\frac{1396159}{630}+\frac{126833}{90}\nu\right)e^2+\left(-\frac{203999}{280}+\frac{56368}{135}\nu\right)e^4+\left(\frac{5681}{1120}-\frac{376}{45}\nu\right)e^6\right.$$

$$+\sqrt{1-e^2}\left(-\frac{1184}{3}+\frac{592}{9}\nu+\left(-\frac{4618}{5}+\frac{2309}{15}\nu\right)e^2+\left(-\frac{626}{15}+\frac{313}{45}\nu\right)e^4\right)\Bigg]\delta\mu\delta\chi\,,\qquad\text{(B4e)}$$

$$b_6^{\rm SO}=e^2\left(-\frac{92444}{45}\pi\theta_{e\chi}\chi_{\rm eff}-\frac{19748}{45}\pi\theta_{e\delta}\delta\mu\delta\chi\right),\qquad\text{(B4f)}$$

where we have introduced the following enhancement functions, related to the spin-orbit tail terms,

$$\theta_{y\chi}=1+\frac{21263}{3008}e^2+\frac{52387}{12032}e^4+\frac{253973}{1732608}e^6-\frac{82103}{13860864}e^8+\mathcal{O}\left(e^{10}\right),\qquad\text{(B5a)}$$

$$\theta_{y\delta}=1+\frac{1897}{592}e^2-\frac{461}{2368}e^4-\frac{42581}{340992}e^6-\frac{3803}{1363968}e^8+\mathcal{O}\left(e^{10}\right),\qquad\text{(B5b)}$$

$$\theta_{e\chi}=1+\frac{377077}{92444}e^2+\frac{7978379}{4437312}e^4+\frac{5258749}{106495488}e^6+\mathcal{O}\left(e^8\right),\qquad\text{(B5c)}$$

$$\theta_{e\delta}=1+\frac{37477}{19748}e^2+\frac{95561}{947904}e^4-\frac{631523}{22749696}e^6+\mathcal{O}\left(e^8\right).\qquad\text{(B5d)}$$

For the spin-spin (SS) part, we take the 2PN fully-spinning contributions from Ref. [72], given in terms of the following function

$$\sigma(a,b,c,a_1+a_2q,b_1+b_2q,c_1+c_2q)=a\boldsymbol{s}^2+b\left(\hat{\boldsymbol{L}}\cdot\boldsymbol{s}\right)^2+c\left|\hat{\boldsymbol{L}}\times\boldsymbol{s}\right|^2\cos 2\psi$$

$$+ \sum_{i=1}^{2} \left[(a_1 + a_2 q_i)\, \boldsymbol{s}_i^2 + (b_1 + b_2 q_i) \left(\hat{\boldsymbol{L}} \cdot \boldsymbol{s}_i \right)^2 + (c_1 + c_2 q_i) \left| \hat{\boldsymbol{L}} \times \boldsymbol{s}_i \right|^2 \cos 2\psi_i \right],$$

(B6)

where q_i is the quadrupole parameter, defined in such a way that $q_i = 1$ for black holes. The 2PN fully-spinning contribution to the evolution equations of y and e^2 are

$$
a_4^{\mathrm{SS}} = \sigma \left(-\frac{84}{5} - \frac{228}{5}e^2 - \frac{33}{5}e^4, \frac{242}{5} + \frac{654}{5}e^2 + \frac{381}{20}e^4, -\frac{447}{10}e^2 - \frac{93}{10}e^4, \frac{88}{5} - 16q + \left(48 - \frac{216}{5}q \right)e^2 + \left(\frac{69}{10} - \frac{63}{10}q \right)e^4, \right.
$$
$$
\left. -\frac{244}{5} + 48q + \left(-132 + \frac{648}{5}q \right)e^2 + \left(-\frac{96}{5} + \frac{189}{10}q \right)e^4, (1-q)\left(\frac{447}{10}e^2 + \frac{93}{10}e^4 \right) \right),
$$

(B7a)

$$
b_4^{\mathrm{SS}} = \sigma \left(\frac{2}{3} - \frac{1961}{15}e^2 - \frac{2527}{12}e^4 - \frac{157}{8}e^6, -\frac{2}{3} + \frac{5623}{15}e^2 + \frac{2393}{4}e^4 + \frac{447}{8}e^6, -\frac{5527}{30}e^2 - \frac{10117}{30}e^4 - \frac{5507}{160}e^6, \right.
$$
$$
-\frac{4}{3} + \left(\frac{682}{5} - \frac{1876}{15}q \right)e^2 + \left(\frac{1337}{6} - \frac{595}{3}q \right)e^4 + \left(\frac{83}{4} - \frac{37}{2}q \right)e^6, \frac{4}{3} + \left(-\frac{5618}{15} + \frac{1876}{5}q \right)e^2
$$
$$
\left. + \left(-\frac{1203}{2} + 595q \right)e^4 + \left(-\frac{225}{4} + \frac{111}{2}q \right)e^6, \left(\frac{2764}{15} - \frac{921}{5}q \right)e^2 + \left(\frac{1687}{5} - \frac{5056}{15}q \right)e^4 + \left(\frac{551}{16} - \frac{172}{5}q \right)e^6 \right).
$$

(B7b)

The next spin-spin contribution enters at 3PN, for which we consider only the aligned-spin (AS) part, derived in Ref. [53]. To simplify the equations we introduce the following parameters.

$$\delta q_S = q_1 + q_2 - 2\,,$$
(B8a)
$$\delta q_A = q_1 - q_2\,,$$
(B8b)

which measure the symmetric and anti-symetric deviations from the quadrupole parameters of a binary black hole. In terms of these new variables, the 3PN aligned spin-spin coefficients are

$$
a_6^{\mathrm{SS,AS}} = \left\{ \frac{30596}{105} + \frac{2539\delta q_S}{105} + \frac{443\delta q_A \delta\mu}{30} + \left(-\frac{688}{5} - \frac{172\delta q_S}{5} \right)\nu + \left[\frac{115078}{45} + \frac{21317\delta q_S}{60} + \frac{3253\delta q_A \delta\mu}{60} \right. \right.
$$
$$
+ \left(-\frac{3962}{3} - \frac{1981\delta q_S}{6} \right)\nu \right]e^2 + \left[\frac{4476649}{2520} + \frac{133703\delta q_S}{420} + \frac{481\delta q_A \delta\mu}{48} + \left(-\frac{53267}{45} - \frac{53267\delta q_S}{180} \right)\nu \right]e^4
$$
$$
+ \left[\frac{17019}{140} + \frac{29831\delta q_S}{1120} + \frac{29\delta q_A \delta\mu}{160} + \left(-\frac{1343}{15} - \frac{1343\delta q_S}{60} \right)\nu \right]e^6 + \frac{1 - \sqrt{1-e^2}}{\sqrt{1-e^2}} \left(-\frac{244}{15} - \frac{52\delta q_S}{15} - \frac{4\delta q_A \delta\mu}{15} \right.
$$
$$
+ \left(\frac{16}{5} + \frac{4\delta q_S}{5} \right)\nu + \left[\frac{6283}{30} + \frac{1339\delta q_S}{30} + \frac{103\delta q_A \delta\mu}{30} + \left(-\frac{206}{5} - \frac{103\delta q_S}{10} \right)\nu \right]e^2 + \left[-\frac{48007}{120} - \frac{10231\delta q_S}{120} \right.
$$
$$
\left. - \frac{787\delta q_A \delta\mu}{120} + \left(\frac{787}{10} + \frac{787\delta q_S}{40} \right)\nu \right]e^4 + \left[-\frac{183}{20} - \frac{39\delta q_S}{20} - \frac{3\delta q_A \delta\mu}{20} + \left(\frac{9}{5} + \frac{9\delta q_S}{20} \right)\nu \right]e^6 \right) \right\}\chi_{\mathrm{eff}}^2
$$
$$
+ \left\{ \left(\frac{3134}{15} + \frac{443\delta q_S}{15} \right)\delta\mu + \left(\frac{5078}{105} - \frac{344\nu}{5} \right)\delta q_A + \left[\left(\frac{30421}{45} + \frac{3253\delta q_S}{30} \right)\delta\mu + \left(\frac{21317}{30} - \frac{1981\nu}{3} \right)\delta q_A \right]e^2 \right.
$$
$$
+ \left[\left(-\frac{111}{5} + \frac{481\delta q_S}{24} \right)\delta\mu + \left(\frac{133703}{210} - \frac{53267\nu}{90} \right)\delta q_A \right]e^4 + \left[\left(-\frac{149}{40} + \frac{29\delta q_S}{80} \right)\delta\mu + \left(\frac{29831}{560} - \frac{1343\nu}{30} \right)\delta q_A \right]e^6
$$
$$
+ \frac{1 - \sqrt{1-e^2}}{\sqrt{1-e^2}} \left(\left(-\frac{104}{15} - \frac{8\delta q_S}{15} \right)\delta\mu + \left(-\frac{104}{15} + \frac{8\nu}{5} \right)\delta q_A + \left[\left(\frac{1339}{15} + \frac{103\delta q_S}{15} \right)\delta\mu + \left(\frac{1339}{15} - \frac{103\nu}{5} \right)\delta q_A \right]e^2 \right.
$$
$$
\left. + \left[\left(-\frac{10231}{60} - \frac{787\delta q_S}{60} \right)\delta\mu + \left(-\frac{10231}{60} + \frac{787\nu}{20} \right)\delta q_A \right]e^4 + \left[\left(-\frac{39}{10} - \frac{3\delta q_S}{10} \right)\delta\mu + \left(-\frac{39}{10} + \frac{9\nu}{10} \right)\delta q_A \right]e^6 \right) \right\}\chi_{\mathrm{eff}}\delta\chi
$$
$$
+ \left\{ \frac{39}{5} + \frac{2539\delta q_S}{105} + \frac{443\delta q_A \delta\mu}{30} + \left(-\frac{1163}{15} - \frac{172\delta q_S}{5} \right)\nu + \left[\frac{659}{15} + \frac{21317\delta q_S}{60} + \frac{3253\delta q_A \delta\mu}{60} \right. \right.
$$
$$
+ \left(-\frac{2399}{15} - \frac{1981\delta q_S}{6} \right)\nu \right]e^2 + \left[\frac{1769}{90} + \frac{133703\delta q_S}{420} + \frac{481\delta q_A \delta\mu}{48} + \left(\frac{2021}{72} - \frac{53267\delta q_S}{180} \right)\nu \right]e^4 + \left[\frac{19}{10} \right.
$$

$$
\begin{aligned}
&+ \frac{29831\delta q_S}{1120} + \frac{29\delta q_A\delta\mu}{160} + \left(-\frac{3}{10} - \frac{1343\delta q_S}{60}\right)\nu\bigg]e^6 + \frac{1-\sqrt{1-e^2}}{\sqrt{1-e^2}}\left(-\frac{4}{15} - \frac{52\delta q_S}{15} - \frac{4\delta q_A\delta\mu}{15}\right. \\
&+ \left(\frac{32}{15} + \frac{4\delta q_S}{5}\right)\nu + \left[\frac{103}{30} + \frac{1339\delta q_S}{30} + \frac{103\delta q_A\delta\mu}{30} + \left(-\frac{412}{15} - \frac{103\delta q_S}{10}\right)\nu\right]e^2 + \left[-\frac{787}{120} - \frac{10231\delta q_S}{120}\right. \\
&\left.- \frac{787\delta q_A\delta\mu}{120} + \left(\frac{787}{15} + \frac{787\delta q_S}{40}\right)\nu\right]e^4 + \left[-\frac{3}{20} - \frac{39\delta q_S}{20} - \frac{3\delta q_A\delta\mu}{20} + \left(\frac{6}{5} + \frac{9\delta q_S}{20}\right)\nu\right]e^6\bigg)\bigg\}\delta\chi^2\,, \quad\text{(B9a)}
\end{aligned}
$$

$$
\begin{aligned}
b_6^{\mathrm{SS,AS}} =& e^2\bigg\{\frac{1468414}{945} + \frac{2852\delta q_S}{105} + \frac{3461\delta q_A\delta\mu}{30} + \left(-\frac{57844}{45} - \frac{14461\delta q_S}{45}\right)\nu + \left[\frac{47715853}{3780} + \frac{1464091\delta q_S}{840} + \frac{11007\delta q_A\delta\mu}{40}\right. \\
&+ \left(-\frac{21865}{3} - \frac{21865\delta q_S}{12}\right)\nu\bigg]e^2 + \left[\frac{4255831}{504} + \frac{166844\delta q_S}{105} + \frac{2941\delta q_A\delta\mu}{48} + \left(-\frac{222533}{45} - \frac{222533\delta q_S}{180}\right)\nu\right]e^4 \\
&+ \left[\frac{414027}{1120} + \frac{365363\delta q_S}{4480} + \frac{511\delta q_A\delta\mu}{640} + \left(-\frac{1287}{5} - \frac{1287\delta q_S}{20}\right)\nu\right]e^6 + \sqrt{1-e^2}\left(\frac{49532}{45} + \frac{10556\delta q_S}{45} + \frac{812\delta q_A\delta\mu}{45}\right. \\
&+ \left(-\frac{3248}{15} - \frac{812\delta q_S}{15}\right)\nu + \left[\frac{140117}{60} + \frac{29861\delta q_S}{60} + \frac{2297\delta q_A\delta\mu}{60} + \left(-\frac{2297}{5} - \frac{2297\delta q_S}{20}\right)\nu\right]e^2 \\
&+ \left.\left[\frac{3721}{180} + \frac{793\delta q_S}{180} + \frac{61\delta q_A\delta\mu}{180} + \left(-\frac{61}{15} - \frac{61\delta q_S}{60}\right)\nu\right]e^4\right)\bigg\}\chi_{\mathrm{eff}}^2 \\
&+ e^2\bigg\{\left(\frac{176426}{135} + \frac{3461\delta q_S}{15}\right)\delta\mu + \left(\frac{5704}{105} - \frac{28922\nu}{45}\right)\delta q_A + \left[\left(\frac{387212}{135} + \frac{11007\delta q_S}{20}\right)\delta\mu\right. \\
&+ \left(\frac{1464091}{420} - \frac{21865\nu}{6}\right)\delta q_A\bigg]e^2 + \left[\left(\frac{2562}{5} + \frac{2941\delta q_S}{24}\right)\delta\mu + \left(\frac{333688}{105} - \frac{222533\nu}{90}\right)\delta q_A\right]e^4 \\
&+ \left[\left(-\frac{33}{32} + \frac{511\delta q_S}{320}\right)\delta\mu + \left(\frac{365363}{2240} - \frac{1287\nu}{10}\right)\delta q_A\right]e^6 + \sqrt{1-e^2}\left(\left(\frac{21112}{45} + \frac{1624\delta q_S}{45}\right)\delta\mu\right. \\
&+ \left(\frac{21112}{45} - \frac{1624\nu}{15}\right)\delta q_A + \left[\left(\frac{29861}{30} + \frac{2297\delta q_S}{30}\right)\delta\mu + \left(\frac{29861}{30} - \frac{2297\nu}{10}\right)\delta q_A\right]e^2 \\
&+ \left.\left[\left(\frac{793}{90} + \frac{61\delta q_S}{90}\right)\delta\mu + \left(\frac{793}{90} - \frac{61\nu}{30}\right)\delta q_A\right]e^4\right)\bigg\}\chi_{\mathrm{eff}}\delta\chi \\
&+ e^2\bigg\{\frac{8887}{135} + \frac{2852\delta q_S}{105} + \frac{3461\delta q_A\delta\mu}{30} + \left(-\frac{13127}{27} - \frac{14461\delta q_S}{45}\right)\nu + \left[\frac{161077}{540} + \frac{1464091\delta q_S}{840} + \frac{11007\delta q_A\delta\mu}{40}\right. \\
&+ \left(-\frac{185723}{270} - \frac{21865\delta q_S}{12}\right)\nu\bigg]e^2 + \left[\frac{14827}{90} + \frac{166844\delta q_S}{105} + \frac{2941\delta q_A\delta\mu}{48} + \left(-\frac{45373}{360} - \frac{222533\delta q_S}{180}\right)\nu\right]e^4 \\
&+ \left[\frac{283}{32} + \frac{365363\delta q_S}{4480} + \frac{511\delta q_A\delta\mu}{640} + \left(-\frac{117}{20} - \frac{1287\delta q_S}{20}\right)\nu\right]e^6 + \sqrt{1-e^2}\left(\frac{812}{45} + \frac{10556\delta q_S}{45} + \frac{812\delta q_A\delta\mu}{45}\right. \\
&+ \left(-\frac{6496}{45} - \frac{812\delta q_S}{15}\right)\nu + \left[\frac{2297}{60} + \frac{29861\delta q_S}{60} + \frac{2297\delta q_A\delta\mu}{60} + \left(-\frac{4594}{15} - \frac{2297\delta q_S}{20}\right)\nu\right]e^2 \\
&+ \left.\left[\frac{61}{180} + \frac{793\delta q_S}{180} + \frac{61\delta q_A\delta\mu}{180} + \left(-\frac{122}{45} - \frac{61\delta q_S}{60}\right)\nu\right]e^4\right)\bigg\}\delta\chi^2\,. \quad\text{(B9b)}
\end{aligned}
$$

2. Evolution of the argument of periastron $\delta\lambda$

For the evolution equation of the argument of periastron $\delta\lambda$ (Eq. (86d)), we need an expression for the periastron advance k, which we express as the following PN series:

$$
k = y^2 \sum_{n=0}^{4} k_n y^n. \qquad\text{(B10)}
$$

The non-spinning part of k_n can be obtained from Ref. [189], by taking the expression of the periastron advance k in terms of the dimensionless energy ε and angular momentum j, substituting the expressions for $\varepsilon(x, e^{\mathrm{ADM}})$ and $j(x, e^{\mathrm{ADM}})$, and converting the eccentricity from ADM to harmonic coordinates using the expressions also provided

in that reference. Doing this we obtain

$$k_0 = 3\,, \tag{B11a}$$

$$k_2^{\mathrm{NS}} = \frac{27}{2} - 7\nu + \left(\frac{51}{4} - \frac{13}{2}\nu\right)e^2\,, \tag{B11b}$$

$$k_4^{\mathrm{NS}} = \frac{105}{2} + \left(-\frac{625}{4} + \frac{123}{32}\pi^2\right)\nu + 7\nu^2 + \left(\frac{573}{4} + \left(-\frac{357}{2} + \frac{123}{128}\pi^2\right)\nu + 40\nu^2\right)e^2$$
$$+ \left(\frac{39}{2} - \frac{55}{4}\nu + \frac{65}{8}\nu^2\right)e^4 + \sqrt{1-e^2}\left(15 - 6\nu + (30 - 12\nu)e^2\right)\,. \tag{B11c}$$

$$\tag{B11d}$$

The fully-spinning part of k_n can be found to 2PN order in Ref. [72]

$$k_1 = -\frac{7}{2}\chi_{\mathrm{eff}} - \frac{1}{2}\delta\mu\delta\chi\,, \tag{B12a}$$

$$k_2^{\mathrm{SS}} = \frac{3}{4}\left\{3\left(\hat{\boldsymbol{L}}\cdot\boldsymbol{s}\right)^2 - \boldsymbol{s}^2 + \sum_{i=1}^{2}(q_i - 1)\left[3\left(\hat{\boldsymbol{L}}\cdot\boldsymbol{s}_i\right)^2 - \boldsymbol{s}_i^2\right]\right\}\,. \tag{B12b}$$

Finally, the aligned-spin contributions to the periastron advance k can be found to 3PN in the supplementary material of Ref. [53]. Using our notation, these coefficients are

$$k_3 = \left[-26 + 8\nu + \left(-\frac{105}{4} + \frac{49\nu}{4}\right)e^2\right]\chi_{\mathrm{eff}} + \left[-8 + \frac{\nu}{2} + \left(-\frac{15}{4} + \frac{7\nu}{4}\right)e^2\right]\delta\mu\delta\chi\,, \tag{B13a}$$

$$k_4^{\mathrm{SS,AS}} = \left\{\frac{181}{8} + \frac{33\delta q_S}{8} + \frac{3\delta q_A\delta\mu}{4} + \left(-\frac{5}{2} - \frac{5\delta q_S}{8}\right)\nu + \left[\frac{369}{16} + \frac{75\delta q_S}{16} + \frac{3\delta q_A\delta\mu}{16} + \left(-\frac{29}{4} - \frac{29\delta q_S}{16}\right)\nu\right]e^2\right\}\chi_{\mathrm{eff}}^2$$
$$+ \left\{\left(\frac{43}{4} + \frac{3\delta q_S}{2}\right)\delta\mu + \left(\frac{33}{4} - \frac{5\nu}{4}\right)\delta q_A + \left[\left(\frac{21}{8} + \frac{3\delta q_S}{8}\right)\delta\mu + \left(\frac{75}{8} - \frac{29\nu}{8}\right)\delta q_A\right]e^2\right\}\chi_{\mathrm{eff}}\delta\chi$$
$$+ \left\{\frac{1}{8} + \frac{33\delta q_S}{8} + \frac{3\delta q_A\delta\mu}{4} + \left(-\frac{7}{2} - \frac{5\delta q_S}{8}\right)\nu + \left[-\frac{3}{16} + \frac{75\delta q_S}{16} + \frac{3\delta q_A\delta\mu}{16} - \frac{29\delta q_S\nu}{16}\right]e^2\right\}\delta\chi^2\,. \tag{B13b}$$

3. Precession averaged fully spinning spin-spin coefficients

The precession averages for most of the PN coefficients given in Appendices B1 and B2 are straight-forward, since they are written in terms of $\delta\chi$ and $\delta\chi^2$. Therefore, to compute their averages it will suffice to do $\delta\chi \to \langle\delta\chi\rangle$ and $\delta\chi^2 \to \langle\delta\chi^2\rangle$, which can be computed with Eq. (81) and Eq. (91) respectively. In contrast, the fully-spinning coefficients entering at 2PN, as written in Eq. (B7) and Eq. (B12b), depend on different quadratic functions of the full spins of the component objects, whose averages are given in Sec. IV A. Substituting these averages in the fully spinning spin-spin coefficients we obtain

$$\langle a_4^{\mathrm{SS}}\rangle = \left[-\frac{84}{5} - \frac{228}{5}e^2 - \frac{33}{5}e^4\right]\langle s_\perp^2\rangle + \left[\frac{8}{5} - 8\delta q_S + \left(\frac{24}{5} - \frac{108\delta q_S}{5}\right)e^2 + \left(\frac{3}{5} - \frac{63\delta q_S}{20}\right)e^4\right](s_1^2 + s_2^2)$$
$$+ \left[-8 - \frac{108}{5}e^2 - \frac{63}{20}e^4\right]\delta q_A(s_1^2 - s_2^2) + \left[\frac{156}{5} + 12\delta q_S + \left(84 + \frac{162\delta q_S}{5}\right)e^2 + \left(\frac{123}{10} + \frac{189\delta q_S}{40}\right)e^4\right]\chi_{\mathrm{eff}}^2$$
$$+ \left[24 + \frac{324}{5}e^2 + \frac{189}{20}e^4\right]\delta q_A\chi_{\mathrm{eff}}\langle\delta\chi\rangle + \left[-\frac{2}{5} + 12\delta q_S + \left(-\frac{6}{5} + \frac{162\delta q_S}{5}\right)e^2 + \left(-\frac{3}{20} + \frac{189\delta q_S}{40}\right)e^4\right]\langle\delta\chi^2\rangle\,, \tag{B14a}$$

$$\langle b_4^{\mathrm{SS}}\rangle = \left[\frac{2}{3} - \frac{1961}{15}e^2 - \frac{2527}{12}e^4 - \frac{157}{8}e^6\right]\langle s_\perp^2\rangle + \left[-\frac{4}{3} + \left(\frac{34}{3} - \frac{938\delta q_S}{15}\right)e^2 + \left(\frac{49}{2} - \frac{595\delta q_S}{6}\right)e^4$$
$$+ \left(\frac{9}{4} - \frac{37\delta q_S}{4}\right)e^6\right](s_1^2 + s_2^2) + \left[-\frac{938}{15} - \frac{595}{6}e^2 - \frac{37}{4}e^4\right]e^2(s_1^2 - s_2^2)\delta q_A + \left[\frac{2}{3} + \left(\frac{3667}{15} + \frac{469\delta q_S}{5}\right)e^2\right.$$

$$+ \left(\frac{4613}{12} + \frac{595\delta q_S}{4} \right) e^4 + \left(\frac{287}{8} + \frac{111\delta q_S}{8} \right) e^6 \Big] \chi_{\text{eff}}^2 + \left[\frac{938}{5} + \frac{595}{2} e^2 + \frac{111}{4} e^4 \right] e^2 \delta q_A \chi_{\text{eff}} \langle \delta\chi \rangle$$

$$+ \left[\frac{2}{3} + \left(\frac{1}{3} + \frac{469\delta q_S}{5} \right) e^2 + \left(-\frac{13}{4} + \frac{595\delta q_S}{4} \right) e^4 + \left(-\frac{3}{8} + \frac{111\delta q_S}{8} \right) e^6 \right] \langle \delta\chi^2 \rangle \,, \tag{B14b}$$

$$\langle k_2^{\text{SS}} \rangle = -\frac{3}{4} \langle s_\perp^2 \rangle - \frac{3}{8}\delta q_S \left(s_1^2 + s_2^2 \right) - \frac{3}{8}\delta q_A \left(s_1^2 - s_2^2 \right) + \left(\frac{3}{2} + \frac{9\delta q_S}{16} \right) \chi_{\text{eff}}^2 + \frac{9\delta q_A}{8} \chi_{\text{eff}} \langle \delta\chi \rangle + \frac{9\delta q_S}{16} \langle \delta\chi^2 \rangle \,, \tag{B14c}$$

where we have introduced the variable

$$\langle s_\perp^2 \rangle = \langle s^2 - \chi_{\text{eff}}^2 \rangle = \left\langle \sigma_0^{(1)} \right\rangle - \chi_{\text{eff}}^2 = s_{1\perp,0}^2 + s_{2\perp,0}^2 + \Delta_{J^2}^2 + \delta\mu \left(\frac{\delta\chi_0 - \langle \delta\chi \rangle}{y} \right) \,. \tag{B15}$$

Appendix C: Leading order time to coalescence

To estimate the time to coalescence at leading order in PN, we use the 0PN expressions for $\mathcal{D}y$ and $\mathcal{D}e^2$, given in appendix B 1, i.e.

$$\mathcal{D}y = \nu y^9 \left(\frac{32}{5} + \frac{28}{5} e^2 \right) \,, \tag{C1a}$$

$$\mathcal{D}e^2 = -\nu y^8 \left(\frac{608}{15} e^2 + \frac{242}{15} e^4 \right) \,. \tag{C1b}$$

Dividing Eq. (C1a) by Eq. (C1b) we obtain

$$\frac{\mathrm{d}y}{\mathrm{d}e^2} = -y \frac{48 + 42e^2}{e^2(304 + 121e^2)} \,, \tag{C2}$$

which can be integrated to obtain y as a function of the eccentricity e, i.e.

$$y(e) = y_0 \frac{h(e)}{h(e_0)} \,, \tag{C3}$$

where we have defined

$$h(e) = e^{-6/19} \left(1 + \frac{121}{304} e^2 \right)^{-435/2299} \,. \tag{C4}$$

From Eq. (C4) and Eq. (C3), we observe that, at coalescence ($y \to \infty$), the eccentricity becomes 0 (i.e. $e \to 0$). Therefore, we can obtain the coalescence time substituting $y(e)$ (Eq. (C3)) in $\mathcal{D}e^2$ (Eq. (C1b)) and integrating $\mathrm{d}t/\mathrm{d}e^2$ from $e^2 = e_0^2$ to $e^2 = 0$, obtaining

$$\tau_c = \frac{5}{256} \frac{M}{\nu y_0^8} \frac{F(e_0)}{\sqrt{1 - e_0^2}} \,, \tag{C5}$$

where $F(e_0)$ is defined as [190]

$$F(e_0) = \frac{24}{19} h^8(e_0) \sqrt{1 - e_0^2} \int_0^{e_0^2} \frac{x^{5/19} \left(1 + \frac{121}{304} x \right)^{1181/2299}}{(1 - x)^{3/2}} \mathrm{d}x, \tag{C6}$$

$$= \frac{48}{19} h^8(e_0) \sqrt{1 - e_0^2} \int_1^{\frac{1}{\sqrt{1-e_0^2}}} \left(1 - \frac{1}{u^2} \right)^{5/19} \left(\frac{425}{304} - \frac{121}{304} \frac{1}{u^2} \right)^{1181/2299} \mathrm{d}u \,. \tag{C7}$$

This function, shown in Fig. 19, is always of order one and can therefore easily be approximated. In our case, for $e_0^2 \le 0.4$ we take the Maclaurin seies of Eq. (C6) with respect to $x_0 = e_0^2$, while for $e_0^2 > 0.4$ we take the Maclaurin seies of Eq. (C7) with respect to $w_0 = \sqrt{1 - e_0^2}$. Substituting the definition of y, given in Eq. (42b), we can compute
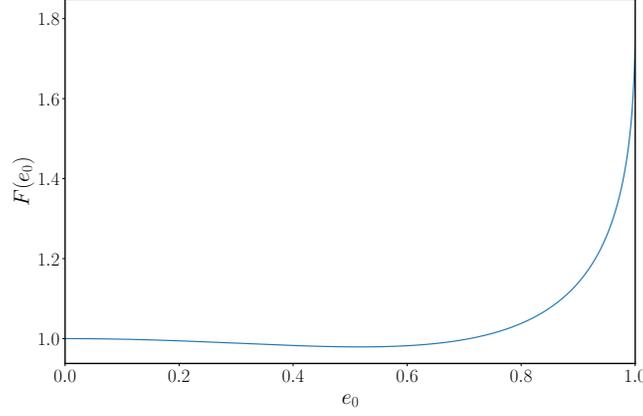
FIG. 19: Plot of the function $F(e_0)$, defined in Eq. (C6), as a function of the initial eccentricity e_0. At $e_0 = 0$, we have that $F(0) = 1$, while at $e_0 = 1$ we have that $F(1) = 768/425 \approx 1.81$.

the time to coalescence in terms of the initial frequency and eccentricity as

$$\tau_c = \frac{5}{256} \left(\frac{G\mathcal{M}_c}{c^3} \right)^{-5/3} \left(\pi f_0^{\mathrm{GW},22} \right)^{-8/3} (1 - e_0^2)^{7/2} F(e_0) , \tag{C8}$$

where we have reintroduced the universal constants G and c and we have defined the chirp mass as

$$\mathcal{M}_c = \nu^{3/5} M = \frac{(m_1 m_2)^{3/5}}{(m_1 + m_2)^{1/5}} . \tag{C9}$$

Appendix D: Series reversion

Given a function $y(x)$ with Maclaurin series

$$y(x) = a_1 x + a_2 x^2 + a_3 x^3 + \dots , \tag{D1}$$

we want to find the Maclaurin series of the inverse function $x(y)$, which we denote

$$x(y) = A_1 y + A_2 y^2 + A_3 y^3 + \dots , \tag{D2}$$

such that

$$y(x(y)) = a_1 A_1 y + (a_2 A_1^2 + a_1 A_2)y^2 + (a_3 A_1^3 + 2a_2 A_1 A_2 + a_1 A_3)y^3 + \dots = y . \tag{D3}$$

Solving Eq. (D3) order by order, we can obtain the constants A_j, which are well known and tabulated in the literature (e.g. in Ref. [105]). These are given as:

$$a_1 A_1 = 1 , \tag{D4a}$$
$$a_1^2 A_2 = -\tilde{a}_2 , \tag{D4b}$$
$$a_1^3 A_3 = 2\tilde{a}_2^2 - \tilde{a}_3 , \tag{D4c}$$
$$a_1^4 A_4 = 5\tilde{a}_2\tilde{a}_3 - \tilde{a}_4 - 5\tilde{a}_2^3 , \tag{D4d}$$
$$a_1^5 A_5 = 6\tilde{a}_2\tilde{a}_4 + 3\tilde{a}_3^2 + 14\tilde{a}_2^4 - \tilde{a}_5 - 21\tilde{a}_2^2\tilde{a}_3 , \tag{D4e}$$

where we have defined

$$\tilde{a}_j = \frac{a_j}{a_1} . \tag{D5}$$

In the context of inverting Eq. (134) to obtain the expression $t_i^{\text{SPA}}(\omega)$ in Eq. (135). We can use the above formulas identifying

$$x \to t_i^{\text{SPA}} - t_j \,, \tag{D6a}$$

$$y \to \omega - \omega_i(t_j) \,, \tag{D6b}$$

$$a_k \to \begin{cases} Q_{\omega,i,j,k} & ,1 \leq k \leq 3 \\ 0 & ,k \geq 4 \end{cases} \,, \tag{D6c}$$

$$A_k \to Q_{t,i,j,k} \,. \tag{D6d}$$

Appendix E: Wigner D-matrices and spin-weighted spherical harmonics used

The Wigner D-matrix can be written in terms of the Wigner small d-matrix as

$$D_{m',m}^l(\alpha, \beta, \gamma) = e^{-im'\alpha} \, d_{m',m}^l(\beta) \, e^{-im\gamma} \,, \tag{E1}$$

where with our convention, the Wigner small d-matrix is given by

$$d_{m',m}^l(\beta) = (-1)^{m'-m} \sqrt{(l+m')!(l-m')!(l+m)!(l-m)!} \sum_{k=\max(0,m-m')}^{\min(l+m,l-m')} \frac{(-1)^k \sin^{2k+m'-m}\left(\frac{\beta}{2}\right) \cos^{2(l-k)+m-m'}\left(\frac{\beta}{2}\right)}{k!(k-m+m')!(l+m-k)!(l-m'-k)!} \,, \tag{E2}$$

which agrees with the convention of Ref. [73] for integer m and m'. In this work, we only need to compute the Wigner matrices for $l = 2$ with $m = 0, \pm 2$. The required values of $d_{m',m}^l(\theta)$ are given by

$$d_{2,2}^2 = \left(\frac{1+\cos\theta}{2}\right)^2 \,, \tag{E3a}$$

$$d_{1,2}^2 = \frac{1}{2}\sin\theta(1+\cos\theta) \,, \tag{E3b}$$

$$d_{0,2}^2 = \sqrt{\frac{3}{8}}\sin^2\theta \,, \tag{E3c}$$

$$d_{-1,2}^2 = \frac{1}{2}\sin\theta(1-\cos\theta) \,, \tag{E3d}$$

$$d_{-2,2}^2 = \left(\frac{1-\cos\theta}{2}\right)^2 \,, \tag{E3e}$$

$$d_{1,0}^2 = -\sqrt{\frac{3}{2}}\sin\theta\cos\theta \,, \tag{E3f}$$

$$d_{0,0}^2 = \frac{3\cos^2\theta - 1}{2} \,. \tag{E3g}$$

The rest of the elements of the Wigner small d-matrix can be obtained by using that

$$d_{m',m}^l = (-1)^{m-m'} d_{m,m'}^l = d_{-m,-m'}^l \,. \tag{E4}$$

For the spin-weighted spherical harmonics we use the following convention

$$_sY_{lm}(\theta, \phi) = (-1)^m \sqrt{\frac{2l+1}{4\pi}} e^{-is\psi} D_{-m,s}^l(\phi, \theta, -\psi),$$

$$= (-1)^m \sqrt{\frac{2l+1}{4\pi}} e^{im\phi} \, d_{-m,s}^l(\theta) \,. \tag{E5}$$

With the d-matrix property of Eq. (E4), we can simplify the spin -2 spherical harmonics, used for decomposing GW emission, as

$$_{-2}Y_{lm}(\theta,\phi) = \sqrt{\frac{2l+1}{4\pi}}\,\mathrm{e}^{\mathrm{i}m\phi}\,d^l_{m,2}(\theta)\,. \tag{E6}$$

Appendix F: Extra parameter estimation information and results

As mentioned in Sec. VII B, for the PE analyses performed in this paper, we use `bilby`. In line with the standard `bilby` conventions, we specify quasi-circular injections via 15 parameters, namely the detector-frame component masses m_1 and m_2, the dimensionless spin magnitudes a_1 and a_2, the angle between the component spins and the angular momentum vector θ_1 and θ_2, the azimuthal angle between spin vectors ϕ_{12}, the azimuthal angle between the total and orbital angular momenta ϕ_{JL}, the angle between the total angular momentum and the vector from the binary to the observer θ_{JN}, the reference binary phase $\phi_{\mathrm{ref}} = \lambda_0$, the luminosity distance d_L, the right ascension ra, the declination dec, the polarization ψ and the reference geocent time $t^{\mathrm{geo}} = t_c$. For eccentric injections we need two more parameters, which we choose to be the initial eccentricity e_0 and initial mean anomaly ℓ_0. In table III we show the parameters of the three injections analyzed in Sec. VII B, together with the SNR at each detector and the total network SNR.

For sampling, we use `bilby`'s [166–168] `acceptance-walk` configuration of `dynesty`, running three parallel chains with $n_{\mathrm{live}} = 1000$ and $n_{\mathrm{accept}} = 60$. With these settings, each PE analysis required the number of likelihood evaluations listed in table IV. As expected, the number of calls increases with SNR and is higher in the eccentric case, due to the additional two parameters and the more constrained posteriors. Nonetheless, we observe that all these numbers are $\mathcal{O}\left(10^8\right)$, in agreement with what was discussed in Eq. (152). Consistently with the waveform timings of Fig. 7 and Eq. (152), the PE analyses took $\mathcal{O}\left(1\,\text{week}\right)$ to run in 16 cores.

In Figs. 20, 21 and 22 we show the corner plots of the posteriors for all important parameters, recovered by the PEs on the `pyEFPE` and Low and High SNR `IMRPhenomXP` injections, respectively. Note that in both Fig. 21 and Fig. 22, the time posteriors for the `pyEFPE` and `IMRPhenomXP` analyses are very different due to the reference time of the waveforms being different. For `pyEFPE` it is the coalescence time described in Eq. (120) while for `IMRPhenomXP`, it is the peak amplitude time [144].

	pyEFPE	IMRPhenomXP (Low SNR)	IMRPhenomXP (High SNR)
$m_1\,[M_\odot]$	10	10	10
$m_2\,[M_\odot]$	1.6	5	5
a_1	0.2	0.2	0.2
a_2	0.3	0.1	0.1
$\theta_1\,[\mathrm{rad}]$	0.9	0.5	0.5
$\theta_2\,[\mathrm{rad}]$	2.2	1.2	1.2
$\phi_{12}\,[\mathrm{rad}]$	3.0	4.0	4.0
$\phi_{JL}\,[\mathrm{rad}]$	3.3	5.0	5.0
$\theta_{JN}\,[\mathrm{rad}]$	1.0	0.4	0.4
$d_L\,[\mathrm{Mpc}]$	500	2000	1000
$\phi_{\mathrm{ref}}\,[\mathrm{rad}]$	0.9	1.6	1.6
$\mathrm{ra}\,[\mathrm{rad}]$	1.0	0.24	0.24
$\mathrm{dec}\,[\mathrm{rad}]$	-0.316	-0.4	-0.4
$\psi\,[\mathrm{rad}]$	0.6	2.7	2.7
$t_c^{\mathrm{GPS}}\,[\mathrm{s}]$	1262276684	1249852257	1249852257
e_0	0.2	–	–
$\ell_0\,[\mathrm{rad}]$	2.5	–	–
H1 SNR	13.25	7.76	15.52
L1 SNR	13.61	9.31	18.61
V1 SNR	5.06	3.91	7.82
Network SNR	19.7	12.7	25.5

TABLE III: Values of the parameters for the three injections analyzed in Sec. VII B. We also list the SNR in each detector (H1, L1 and V1), computed with their projected O5 sensitivities [132, 133], also used in the PEs of Sec. VII B. Finally, we show the total network SNR, obtained by combining in quadrature the individual detector SNRs.

	pyEFPE	IMRPhenomXP (Low SNR)	IMRPhenomXP (High SNR)
pyEFPE	$1.87 \cdot 10^8$	$0.81 \cdot 10^8$	$1.11 \cdot 10^8$
pyEFPE ($e_0 = 0$)	——	$0.81 \cdot 10^8$	$1.09 \cdot 10^8$
IMRPhenomXP	——	$0.81 \cdot 10^8$	$1.06 \cdot 10^8$

TABLE IV: Number of likelihood evaluations required in each PE analysis of Sec. VII B. Columns correspond to different injections, and rows to different recovery cases.
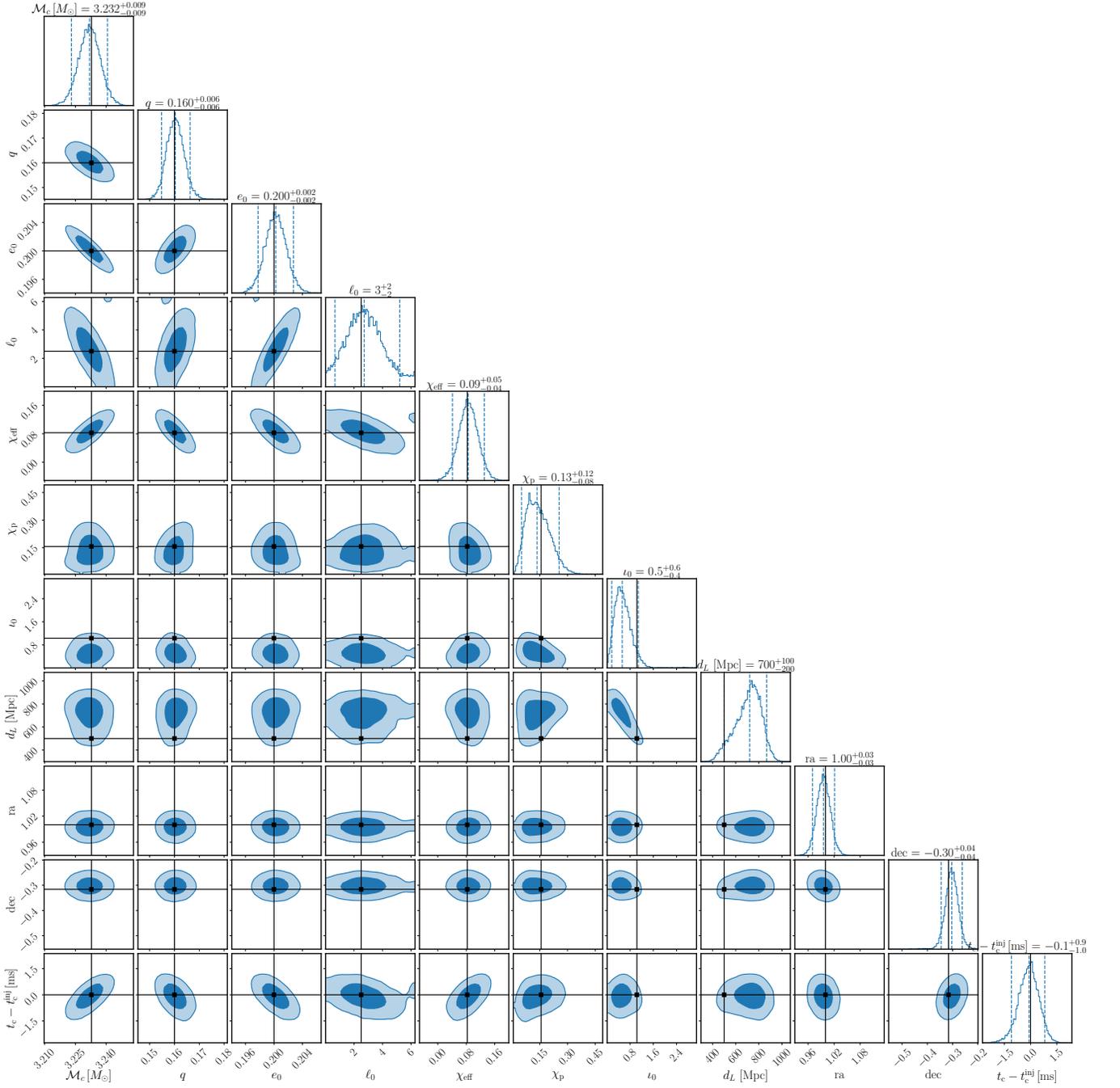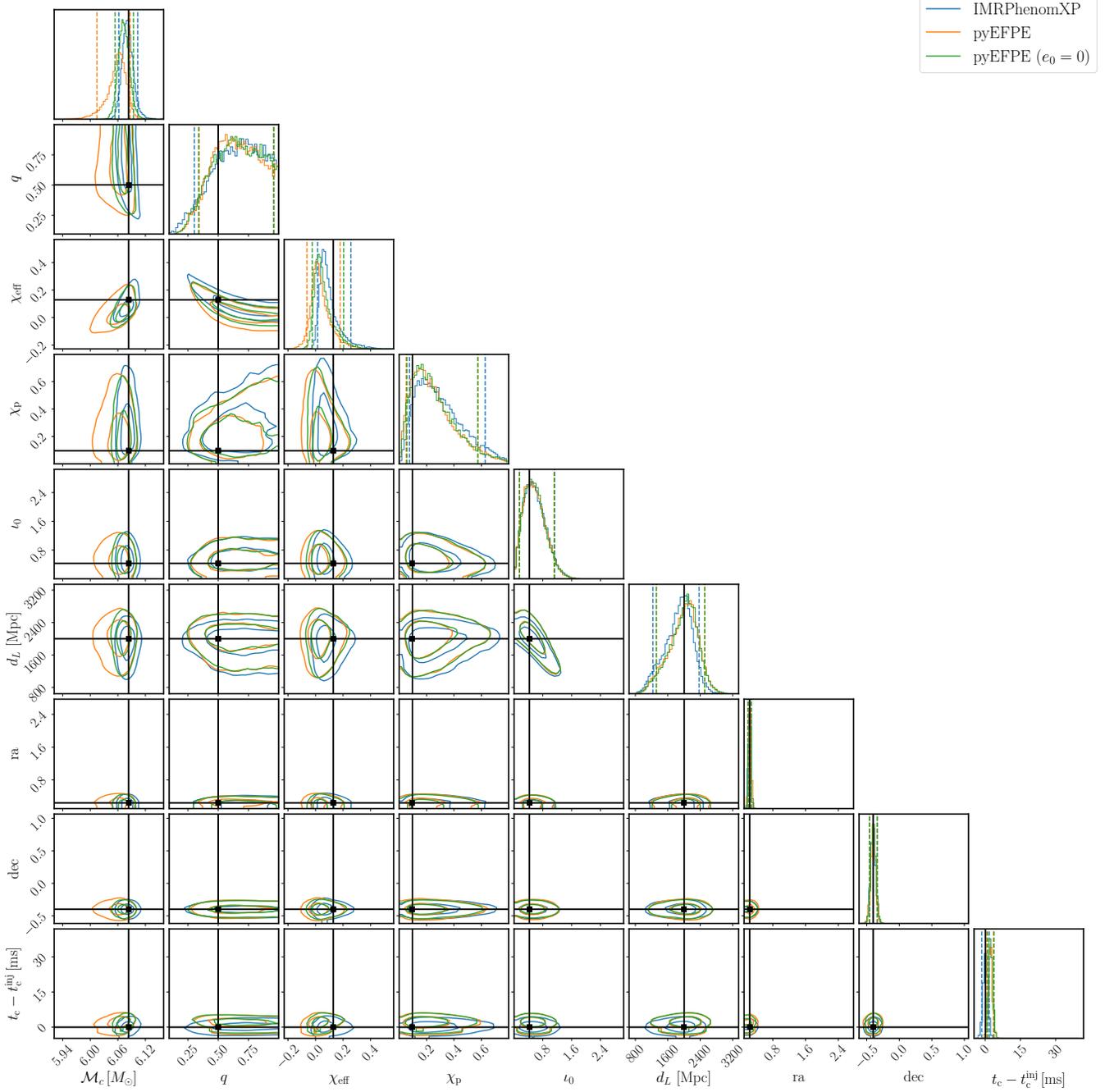
FIG. 20: Corner plot showing the joint posterior distributions of the most important parameters of the `pyEFPE` injection-recovery study. Specifically, the plot displays the chirp mass $\mathcal{M}_c$, mass ratio q, initial eccentricity e_0, initial mean anomaly ℓ_0, effective inspiral spin parameter $\chi_{\rm eff}$, effective precession spin parameter $\chi_{\rm P}$, initial inclination ι_0, luminosity distance d_L, right ascension ra, declination dec and difference between measured and injected coalescence times $t_c - t_c^{\rm inj}$. The diagonal panels display the marginal distributions for each parameter, along with the median and 90% confidence interval. The off-diagonal panels show the bivariate correlations between pairs of parameters, with the contours representing the 50% and 90% confidence regions. The black lines mark the values of the injected parameters.
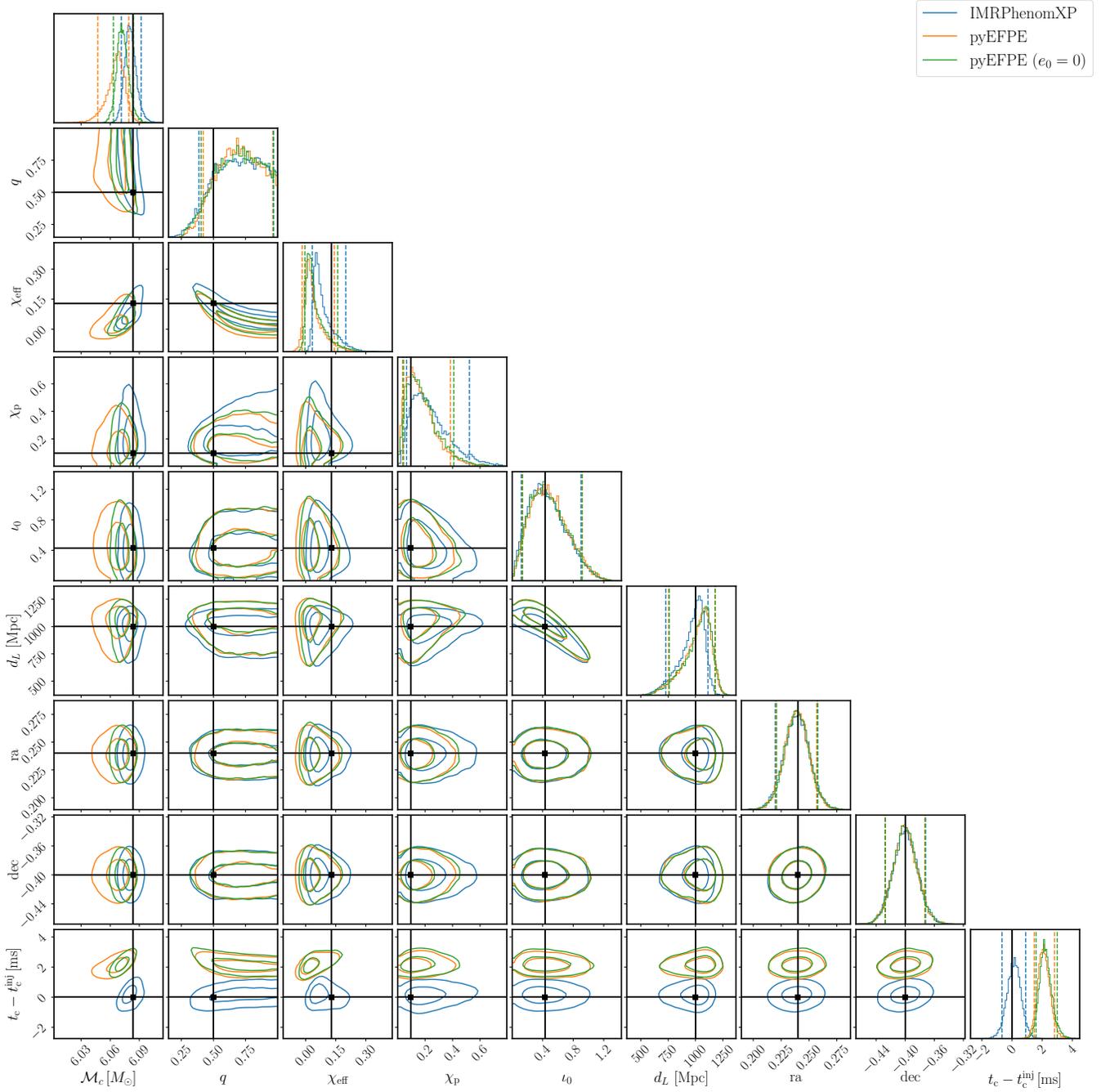
FIG. 21: Corner plot showing the joint posterior distributions of the most important parameters of the `IMRPhenomXP` injection recovered with `IMRPhenomXP`, `pyEFPE` and `pyEFPE` with $e_0 = 0$ for the low SNR case. Specifically, the plot displays the chirp mass $\mathcal{M}_c$, mass ratio q, effective inspiral spin parameter χ_{eff}, effective precession spin parameter χ_{p}, initial inclination ι_0, luminosity distance d_L, right ascension ra, declination dec and difference between measured and injected coalescence times $t_c - t_c^{\text{inj}}$. In each corner plot, the diagonal panels display the marginal distributions for each parameter, along with the 90% confidence interval. The off-diagonal panels show the bivariate correlations between pairs of parameters, with the contours representing the 50% and 90% confidence regions. The black lines mark the values of the injected parameters.

FIG. 22: Corner plot showing the joint posterior distributions of the most important parameters of the `IMRPhenomXP` injection recovered with `IMRPhenomXP`, `pyEFPE` and `pyEFPE` with $e_0 = 0$ for the high SNR case. Specifically, the plot displays the chirp mass $\mathcal{M}_c$, mass ratio q, effective inspiral spin parameter χ_{eff}, effective precession spin parameter χ_{p}, initial inclination ι_0, luminosity distance d_L, right ascension ra, declination dec and difference between measured and injected coalescence times $t_c - t_c^{\mathrm{inj}}$. In each corner plot, the diagonal panels display the marginal distributions for each parameter, along with the 90% confidence interval. The off-diagonal panels show the bivariate correlations between pairs of parameters, with the contours representing the 50% and 90% confidence regions. The black lines mark the values of the injected parameters.

[1] J. Aasi *et al.* (LIGO Scientific), Advanced LIGO, Class. Quant. Grav. **32**, 074001 (2015), arXiv:1411.4547 [gr-qc].

[2] F. Acernese *et al.* (VIRGO), Advanced Virgo: a second-generation interferometric gravitational wave detector, Class. Quant. Grav. **32**, 024001 (2015), arXiv:1408.3978 [gr-qc].

[3] T. Akutsu *et al.* (KAGRA), KAGRA: 2.5 Generation Interferometric Gravitational Wave Detector, Nature Astron. **3**, 35 (2019), arXiv:1811.08079 [gr-qc].

[4] B. P. Abbott *et al.* (LIGO Scientific, Virgo), GWTC-1: A Gravitational-Wave Transient Catalog of Compact Binary Mergers Observed by LIGO and Virgo during the First and Second Observing Runs, Phys. Rev. X **9**, 031040 (2019), arXiv:1811.12907 [astro-ph.HE].

[5] R. Abbott *et al.* (LIGO Scientific, Virgo), GWTC-2: Compact Binary Coalescences Observed by LIGO and Virgo During the First Half of the Third Observing Run, Phys. Rev. X **11**, 021053 (2021), arXiv:2010.14527 [gr-qc].

[6] R. Abbott *et al.* (KAGRA, VIRGO, LIGO Scientific), GWTC-3: Compact Binary Coalescences Observed by LIGO and Virgo during the Second Part of the Third Observing Run, Phys. Rev. X **13**, 041039 (2023), arXiv:2111.03606 [gr-qc].

[7] I. Mandel and A. Farmer, Merging stellar-mass binary black holes, Phys. Rept. **955**, 1 (2022), arXiv:1806.05820 [astro-ph.HE].

[8] M. Mapelli, Formation channels of single and binary stellar-mass black holes, in *Handbook of Gravitational Wave Astronomy*, edited by C. Bambi, S. Katsanevas, and K. D. Kokkotas (Springer, Singapore, 2021).

[9] D. Gerosa and M. Fishbach, Hierarchical mergers of stellar-mass black holes and their gravitational-wave signatures, Nature Astron. **5**, 749 (2021), arXiv:2105.03439 [astro-ph.HE].

[10] I. Mandel and F. S. Broekgaarden, Rates of compact object coalescences, Living Rev. Rel. **25**, 1 (2022), arXiv:2107.14239 [astro-ph.HE].

[11] R. Abbott *et al.* (KAGRA, VIRGO, LIGO Scientific), Population of Merging Compact Binaries Inferred Using Gravitational Waves through GWTC-3, Phys. Rev. X **13**, 011048 (2023), arXiv:2111.03634 [astro-ph.HE].

[12] C. L. Rodriguez, M. Zevin, C. Pankow, V. Kalogera, and F. A. Rasio, Illuminating Black Hole Binary Formation Channels with Spins in Advanced LIGO, Astrophys. J. Lett. **832**, L2 (2016), arXiv:1609.05916 [astro-ph.HE].

[13] D. Gerosa, E. Berti, R. O'Shaughnessy, K. Belczynski, M. Kesden, D. Wysocki, and W. Gladysz, Spin orientations of merging black holes formed from the evolution of stellar binaries, Phys. Rev. D **98**, 084036 (2018), arXiv:1808.02491 [astro-ph.HE].

[14] S. Banerjee, A. Olejak, and K. Belczynski, Symmetry Breaking in Merging Binary Black Holes from Young Massive Clusters and Isolated Binaries, Astrophys. J. **953**, 80 (2023), arXiv:2302.10851 [astro-ph.HE].

[15] S. Naoz, The eccentric kozai-lidov effect and its applications, Annual Review of Astronomy and Astrophysics **54**, 441–489 (2016).

[16] J. Samsing, Eccentric Black Hole Mergers Forming in Globular Clusters, Phys. Rev. D **97**, 103014 (2018), arXiv:1711.07452 [astro-ph.HE].

[17] H. Tagawa, B. Kocsis, Z. Haiman, I. Bartos, K. Omukai, and J. Samsing, Eccentric Black Hole Mergers in Active Galactic Nuclei, Astrophys. J. Lett. **907**, L20 (2021), arXiv:2010.10526 [astro-ph.HE].

[18] M. Zevin, I. M. Romero-Shaw, K. Kremer, E. Thrane, and P. D. Lasky, Implications of Eccentric Observations on Binary Black Hole Formation Channels, Astrophys. J. Lett. **921**, L43 (2021), arXiv:2106.09042 [astro-ph.HE].

[19] A. Bonino, R. Gamba, P. Schmidt, A. Nagar, G. Pratten, M. Breschi, P. Rettegno, and S. Bernuzzi, Inferring eccentricity evolution from observations of coalescing binary black holes, Phys. Rev. D **107**, 064024 (2023), arXiv:2207.10474 [gr-qc].

[20] V. Gayathri, J. Healy, J. Lange, B. O'Brien, M. Szczepanczyk, I. Bartos, M. Campanelli, S. Klimenko, C. O. Lousto, and R. O'Shaughnessy, Eccentricity estimate for black hole mergers with numerical relativity simulations, Nature Astron. **6**, 344 (2022), arXiv:2009.05461 [astro-ph.HE].

[21] R. Gamba, M. Breschi, G. Carullo, S. Albanesi, P. Rettegno, S. Bernuzzi, and A. Nagar, GW190521 as a dynamical capture of two nonspinning black holes, Nature Astron. **7**, 11 (2023), arXiv:2106.05575 [gr-qc].

[22] I. M. Romero-Shaw, P. D. Lasky, and E. Thrane, Four Eccentric Mergers Increase the Evidence that LIGO–Virgo–KAGRA's Binary Black Holes Form Dynamically, Astrophys. J. **940**, 171 (2022), arXiv:2206.14695 [astro-ph.HE].

[23] N. Gupte *et al.*, Evidence for eccentricity in the population of binary black holes observed by LIGO-Virgo-KAGRA, (2024), arXiv:2404.14286 [gr-qc].

[24] G. Fumagalli and D. Gerosa, Spin-eccentricity interplay in merging binary black holes, Phys. Rev. D **108**, 124055 (2023), arXiv:2310.16893 [gr-qc].

[25] G. Fumagalli, I. Romero-Shaw, D. Gerosa, V. De Renzis, K. Kritos, and A. Olejak, Residual eccentricity as a systematic uncertainty on the formation channels of binary black holes, Phys. Rev. D **110**, 063012 (2024), arXiv:2405.14945 [astro-ph.HE].

[26] I. M. Romero-Shaw, D. Gerosa, and N. Loutrel, Eccentricity or spin precession? Distinguishing subdominant effects in gravitational-wave data, Mon. Not. Roy. Astron. Soc. **519**, 5352 (2023), arXiv:2211.07528 [astro-ph.HE].

[27] C. McIsaac, C. Hoy, and I. Harry, Search technique to observe precessing compact binary mergers in the advanced detector era, Phys. Rev. D **108**, 123016 (2023), arXiv:2303.17364 [gr-qc].

[28] K. S. Phukon, P. Schmidt, and G. Pratten, A geometric template bank for the detection of spinning low-mass compact binaries with moderate orbital eccentricity, (2024), arXiv:2412.06433 [gr-qc].

[29] B. Gadre, K. Soni, S. Tiwari, A. Ramos-Buades, M. Haney, and S. Mitra, Detectability of eccentric binary black holes with matched filtering and unmodeled pipelines during the third observing run of LIGO-Virgo-KAGRA, Phys. Rev. D **110**, 044013 (2024), arXiv:2405.04186 [gr-qc].

[30] S. Schmidt *et al.*, Searching for gravitational-wave

signals from precessing black hole binaries with the GstLAL pipeline, Phys. Rev. D **110**, 023038 (2024), arXiv:2403.17186 [gr-qc].

[31] P. Saini, M. Favata, and K. G. Arun, Systematic bias on parametrized tests of general relativity due to neglect of orbital eccentricity, Phys. Rev. D **106**, 084031 (2022), arXiv:2203.04634 [gr-qc].

[32] P. Narayan, N. K. Johnson-McDaniel, and A. Gupta, Effect of ignoring eccentricity in testing general relativity with gravitational waves, Phys. Rev. D **108**, 064003 (2023), arXiv:2306.04068 [gr-qc].

[33] M. A. Shaikh, S. A. Bhat, and S. J. Kapadia, A study of the inspiral-merger-ringdown consistency test with gravitational-wave signals from compact binaries in eccentric orbits, Phys. Rev. D **110**, 024030 (2024), arXiv:2402.15110 [gr-qc].

[34] S. A. Bhat, P. Saini, M. Favata, C. Gandevikar, C. K. Mishra, and K. G. Arun, Parametrized tests of general relativity using eccentric compact binaries, Phys. Rev. D **110**, 124062 (2024), arXiv:2408.14132 [gr-qc].

[35] A. Sesana, Black Hole Science With the Laser Interferometer Space Antenna, Front. Astron. Space Sci. **8**, 601646 (2021), arXiv:2105.11518 [astro-ph.CO].

[36] P. Amaro-Seoane *et al.* (LISA), Astrophysics with the Laser Interferometer Space Antenna, Living Rev. Rel. **26**, 2 (2023), arXiv:2203.06016 [gr-qc].

[37] M. Colpi *et al.* (LISA), LISA Definition Study Report, (2024), arXiv:2402.07571 [astro-ph.CO].

[38] J. M. Bardeen and J. A. Petterson, The Lense-Thirring Effect and Accretion Disks around Kerr Black Holes, Astrophys. J. Lett. **195**, L65 (1975).

[39] T. Bogdanovic, C. S. Reynolds, and M. C. Miller, Alignment of the spins of supermassive black holes prior to merger, Astrophys. J. Lett. **661**, L147 (2007), arXiv:astro-ph/0703054.

[40] J. Lense and H. Thirring, Ueber den Einfluss der Eigenrotation der Zentralkoerper auf die Bewegung der Planeten und Monde nach der Einsteinschen Gravitationstheorie, Phys. Z. **19**, 156 (1918).

[41] P. J. Armitage and P. Natarajan, Eccentricity of supermassive black hole binaries coalescing from gas rich mergers, Astrophys. J. **634**, 921 (2005), arXiv:astro-ph/0508493.

[42] A. I. Macfadyen and M. Milosavljevic, An Eccentric Circumbinary Accretion Disk and the Detection of Binary Massive Black Holes, Astrophys. J. **672**, 83 (2008), arXiv:astro-ph/0607467.

[43] M. Dotti, M. Colpi, F. Haardt, and L. Mayer, Massive black hole binaries in gaseous nuclear discs, Mem. Soc. Ast. It. **79**, 1294 (2008), arXiv:0807.3626 [astro-ph].

[44] K. Hayasaki, A new mechanism for massive binary black hole coalescences, Publ. Astron. Soc. Jap. **61**, 65 (2009), arXiv:0805.3408 [astro-ph].

[45] J. Cuadra, P. J. Armitage, R. D. Alexander, and M. C. Begelman, Massive black hole binary mergers within sub-pc scale gas discs, Mon. Not. Roy. Astron. Soc. **393**, 1423 (2009), arXiv:0809.0311 [astro-ph].

[46] Z. Haiman, B. Kocsis, and K. Menou, The Population of Viscosity- and Gravitational Wave-driven Supermassive Black Hole Binaries Among Luminous Active Galactic Nuclei, Astrophys. J. **700**, 1952 (2009), arXiv:0904.1383 [astro-ph.CO].

[47] J. Zrake, C. Tiede, A. MacFadyen, and Z. Haiman, Equilibrium Eccentricity of Accreting Binaries, Astrophys. J. Lett. **909**, L13 (2021), arXiv:2010.09707 [astro-ph.HE].

[48] Y. Boetzel, A. Susobhanan, A. Gopakumar, A. Klein, and P. Jetzer, Solving post-Newtonian accurate Kepler Equation, Phys. Rev. D **96**, 044011 (2017), arXiv:1707.02088 [gr-qc].

[49] B. Moore and N. Yunes, A 3PN Fourier Domain Waveform for Non-Spinning Binaries with Moderate Eccentricity, Class. Quant. Grav. **36**, 185003 (2019), arXiv:1903.05203 [gr-qc].

[50] Y. Boetzel, C. K. Mishra, G. Faye, A. Gopakumar, and B. R. Iyer, Gravitational-wave amplitudes for compact binaries in eccentric orbits at the third post-Newtonian order: Tail contributions and postadiabatic corrections, Phys. Rev. D **100**, 044018 (2019), arXiv:1904.11814 [gr-qc].

[51] G. Cho, S. Tanay, A. Gopakumar, and H. M. Lee, Generalized quasi-Keplerian solution for eccentric, nonspinning compact binaries at 4PN order and the associated inspiral-merger-ringdown waveform, Phys. Rev. D **105**, 064010 (2022), arXiv:2110.09608 [gr-qc].

[52] K. Paul and C. K. Mishra, Spin effects in spherical harmonic modes of gravitational waves from eccentric compact binary inspirals, Phys. Rev. D **108**, 024023 (2023), arXiv:2211.04155 [gr-qc].

[53] Q. Henry and M. Khalil, Spin effects in gravitational waveforms and fluxes for binaries on eccentric orbits to the third post-Newtonian order, Phys. Rev. D **108**, 104016 (2023), arXiv:2308.13606 [gr-qc].

[54] O. Sridhar, S. Bhattacharyya, K. Paul, and C. K. Mishra, Spin effects in the phasing formula of eccentric compact binary inspirals till the third post-Newtonian order, (2024), arXiv:2412.10909 [gr-qc].

[55] D. Chiaramello and A. Nagar, Faithful analytical effective-one-body waveform model for spin-aligned, moderately eccentric, coalescing black hole binaries, Phys. Rev. D **101**, 101501 (2020), arXiv:2001.11736 [gr-qc].

[56] A. Nagar, A. Bonino, and P. Rettegno, Effective one-body multipolar waveform model for spin-aligned, quasicircular, eccentric, hyperbolic black hole binaries, Phys. Rev. D **103**, 104021 (2021), arXiv:2101.08624 [gr-qc].

[57] M. Khalil, A. Buonanno, J. Steinhoff, and J. Vines, Radiation-reaction force and multipolar waveforms for eccentric, spin-aligned binaries in the effective-one-body formalism, Phys. Rev. D **104**, 024046 (2021), arXiv:2104.11705 [gr-qc].

[58] A. Ramos-Buades, A. Buonanno, M. Khalil, and S. Ossokine, Effective-one-body multipolar waveforms for eccentric binary black holes with nonprecessing spins, Phys. Rev. D **105**, 044035 (2022), arXiv:2112.06952 [gr-qc].

[59] S. Albanesi, A. Placidi, A. Nagar, M. Orselli, and S. Bernuzzi, New avenue for accurate analytical waveforms and fluxes for eccentric compact binaries, Phys. Rev. D **105**, L121503 (2022), arXiv:2203.16286 [gr-qc].

[60] S. Albanesi, A. Nagar, S. Bernuzzi, A. Placidi, and M. Orselli, Assessment of effective-one-body radiation reactions for generic planar orbits, Phys. Rev. D **105**, 104031 (2022), arXiv:2202.10063 [gr-qc].

[61] A. Placidi, S. Albanesi, A. Nagar, M. Orselli, S. Bernuzzi, and G. Grignani, Exploiting Newton-factorized, 2PN-accurate waveform multipoles in

effective-one-body models for spin-aligned noncircularized binaries, Phys. Rev. D **105**, 104030 (2022), arXiv:2112.05448 [gr-qc].

[62] A. Nagar, D. Chiaramello, R. Gamba, S. Albanesi, S. Bernuzzi, V. Fantini, M. Panzeri, and P. Rettegno, Effective-one-body waveform model for noncircularized, planar, coalescing black hole binaries II:high accuracy by improving logarithmic terms in resummations, (2024), arXiv:2407.04762 [gr-qc].

[63] A. Nagar, R. Gamba, P. Rettegno, V. Fantini, and S. Bernuzzi, Effective-one-body waveform model for noncircularized, planar, coalescing black hole binaries: The importance of radiation reaction, Phys. Rev. D **110**, 084001 (2024), arXiv:2404.05288 [gr-qc].

[64] A. Gamboa, M. Khalil, and A. Buonanno, Third post-Newtonian dynamics for eccentric orbits and aligned spins in the effective-one-body waveform model SEOB-NRv5EHM, (2024), arXiv:2412.12831 [gr-qc].

[65] A. Gamboa *et al.*, Accurate waveforms for eccentric, aligned-spin binary black holes: The multipolar effective-one-body model SEOBNRv5EHM, (2024), arXiv:2412.12823 [gr-qc].

[66] T. Islam, V. Varma, J. Lodman, S. E. Field, G. Khanna, M. A. Scheel, H. P. Pfeiffer, D. Gerosa, and L. E. Kidder, Eccentric binary black hole surrogate models for the gravitational waveform and remnant properties: comparable mass, nonspinning case, Phys. Rev. D **103**, 064022 (2021), arXiv:2101.11798 [gr-qc].

[67] K. Paul, A. Maurya, Q. Henry, K. Sharma, P. Satheesh, Divyajyoti, P. Kumar, and C. K. Mishra, ESIGMAHM: An Eccentric, Spinning inspiral-merger-ringdown waveform model with Higher Modes for the detection and characterization of binary black holes, (2024), arXiv:2409.13866 [gr-qc].

[68] P. Csizmadia, G. Debreczeni, I. Racz, and M. Vasuth, Gravitational waves from spinning eccentric binaries, Class. Quant. Grav. **29**, 245002 (2012), arXiv:1207.0001 [gr-qc].

[69] B. Ireland, O. Birnholtz, H. Nakano, E. West, and M. Campanelli, Eccentric Binary Black Holes with Spin via the Direct Integration of the Post-Newtonian Equations of Motion, Phys. Rev. D **100**, 024015 (2019), arXiv:1904.03443 [gr-qc].

[70] M. van de Meent, Gravitational self-force on generic bound geodesics in Kerr spacetime, Phys. Rev. D **97**, 104033 (2018), arXiv:1711.09607 [gr-qc].

[71] A. Klein and P. Jetzer, Spin effects in the phasing of gravitational waves from binaries on eccentric orbits, Phys. Rev. D **81**, 124001 (2010), arXiv:1005.2046 [gr-qc].

[72] A. Klein, Y. Boetzel, A. Gopakumar, P. Jetzer, and L. de Vittori, Fourier domain gravitational waveforms for precessing eccentric binaries, Phys. Rev. D **98**, 104043 (2018), arXiv:1801.08542 [gr-qc].

[73] A. Klein, EFPE: Efficient fully precessing eccentric gravitational waveforms for binaries with long inspirals, (2021), arXiv:2106.10291 [gr-qc].

[74] J. N. Arredondo, A. Klein, and N. Yunes, Efficient gravitational-wave model for fully-precessing and moderately eccentric, compact binary inspirals, Phys. Rev. D **110**, 044044 (2024), arXiv:2402.06804 [gr-qc].

[75] X. Liu, Z. Cao, and Z.-H. Zhu, Effective-one-body numerical-relativity waveform model for eccentric spin-precessing binary black hole coalescence, Class. Quant. Grav. **41**, 195019 (2024), arXiv:2310.04552 [gr-qc].

[76] R. Gamba, D. Chiaramello, and S. Neogi, Toward efficient effective-one-body models for generic, non-planar orbits, Phys. Rev. D **110**, 024031 (2024), arXiv:2404.15408 [gr-qc].

[77] C. M. Bender and S. A. Orszag, *Advanced Mathematical Methods for Scientists and Engineers 1: Asymptotic Methods and Perturbation Theory* (Springer, New York, 1999).

[78] A. Klein, N. Cornish, and N. Yunes, Gravitational waveforms for precessing, quasicircular binaries via multiple scale analysis and uniform asymptotics: The near spin alignment case, Phys. Rev. D **88**, 124015 (2013), arXiv:1305.1932 [gr-qc].

[79] K. Chatziioannou, A. Klein, N. Yunes, and N. Cornish, Gravitational Waveforms for Precessing, Quasicircular Compact Binaries with Multiple Scale Analysis: Small Spin Expansion, Phys. Rev. D **88**, 063011 (2013), arXiv:1307.4418 [gr-qc].

[80] M. Kesden, D. Gerosa, R. O'Shaughnessy, E. Berti, and U. Sperhake, Effective potentials and morphological transitions for binary black-hole spin precession, Phys. Rev. Lett. **114**, 081103 (2015), arXiv:1411.0674 [gr-qc].

[81] D. Gerosa, M. Kesden, U. Sperhake, E. Berti, and R. O'Shaughnessy, Multi-timescale analysis of phase transitions in precessing black-hole binaries, Phys. Rev. D **92**, 064016 (2015), arXiv:1506.03492 [gr-qc].

[82] K. Chatziioannou, A. Klein, N. Yunes, and N. Cornish, Constructing Gravitational Waves from Generic Spin-Precessing Compact Binary Inspirals, Phys. Rev. D **95**, 104004 (2017), arXiv:1703.03967 [gr-qc].

[83] D. Gerosa, G. Fumagalli, M. Mould, G. Cavallotto, D. P. Monroy, D. Gangardt, and V. De Renzis, Efficient multi-timescale dynamics of precessing black-hole binaries, Phys. Rev. D **108**, 024042 (2023), arXiv:2304.04801 [gr-qc].

[84] A. Klein, N. Cornish, and N. Yunes, Fast Frequency-domain Waveforms for Spin-Precessing Binary Inspirals, Phys. Rev. D **90**, 124029 (2014), arXiv:1408.5158 [gr-qc].

[85] C. K. Mishra, K. G. Arun, and B. R. Iyer, Third post-Newtonian gravitational waveforms for compact binary systems in general orbits: Instantaneous terms, Phys. Rev. D **91**, 084040 (2015), arXiv:1501.07096 [gr-qc].

[86] P. Schmidt, M. Hannam, S. Husa, and P. Ajith, Tracking the precession of compact binaries from their gravitational-wave signal, Phys. Rev. D **84**, 024046 (2011), arXiv:1012.2879 [gr-qc].

[87] R. O'Shaughnessy, B. Vaishnav, J. Healy, Z. Meeks, and D. Shoemaker, Efficient asymptotic frame selection for binary black hole spacetimes using asymptotic radiation, Phys. Rev. D **84**, 124002 (2011), arXiv:1109.5224 [gr-qc].

[88] M. Boyle, R. Owen, and H. P. Pfeiffer, A geometric approach to the precession of compact binaries, Phys. Rev. D **84**, 124011 (2011), arXiv:1110.2965 [gr-qc].

[89] P. Schmidt, M. Hannam, and S. Husa, Towards models of gravitational waveforms from generic binaries: A simple approximate mapping between precessing and non-precessing inspiral signals, Phys. Rev. D **86**, 104063 (2012), arXiv:1207.3088 [gr-qc].

[90] T. Damour and N. Deruelle, Ann. Inst. Henri Poincaré Phys. Théor. **43**, 107 (1985).

[91] P. Colwell, *Solving Kepler's Equation over Three Cen-*

turies (Willmann-Bell, 1993).

[92] T. Damour and G. Schaefer, Higher Order Relativistic Periastron Advances and Binary Pulsars, Nuovo Cim. B **101**, 127 (1988).

[93] G. Schäfer and N. Wex, Second post-Newtonian motion of compact binaries, Phys. Lett. A **174**, 196 (1993), provided by the SAO/NASA Astrophysics Data System.

[94] N. Wex, The second post-Newtonian motion of compact binary-star systems with spin, Class. Quant. Grav. **12**, 983 (1995).

[95] R.-M. Memmesheimer, A. Gopakumar, and G. Schaefer, Third post-Newtonian accurate generalized quasi-Keplerian parametrization for compact binaries in eccentric orbits, Phys. Rev. D **70**, 104011 (2004), arXiv:gr-qc/0407049.

[96] T. Damour, A. Gopakumar, and B. R. Iyer, Phasing of gravitational waves from inspiralling eccentric binaries, Phys. Rev. D **70**, 064028 (2004), arXiv:gr-qc/0404128.

[97] K. G. Arun, L. Blanchet, B. R. Iyer, and M. S. S. Qusailah, Tail effects in the 3PN gravitational wave energy flux of compact binaries in quasi-elliptical orbits, Phys. Rev. D **77**, 064034 (2008), arXiv:0711.0250 [gr-qc].

[98] K. S. Thorne, Multipole Expansions of Gravitational Radiation, Rev. Mod. Phys. **52**, 299 (1980).

[99] L. E. Kidder, Using full information when computing modes of post-Newtonian waveforms from inspiralling compact binaries in circular orbit, Phys. Rev. D **77**, 044016 (2008), arXiv:0710.0614 [gr-qc].

[100] B. M. Barker and R. F. O'Connell, Gravitational Two-Body Problem with Arbitrary Masses, Spins, and Quadrupole Moments, Phys. Rev. D **12**, 329 (1975).

[101] T. A. Apostolatos, C. Cutler, G. J. Sussman, and K. S. Thorne, Spin-induced orbital precession and its modulation of the gravitational waveforms from merging binaries, Phys. Rev. D **49**, 6274 (1994).

[102] M. Boyle, L. E. Kidder, S. Ossokine, and H. P. Pfeiffer, Gravitational-wave modes from precessing black-hole binaries, (2014), arXiv:1409.4431 [gr-qc].

[103] A. Ramos-Buades, P. Schmidt, G. Pratten, and S. Husa, Validity of common modeling approximations for precessing binary black holes with higher-order modes, Phys. Rev. D **101**, 103014 (2020), arXiv:2001.10936 [gr-qc].

[104] A. Buonanno, Y.-b. Chen, and M. Vallisneri, Detecting gravitational waves from precessing binaries of spinning compact objects: Adiabatic limit, Phys. Rev. D **67**, 104025 (2003), [Erratum: Phys.Rev.D 74, 029904 (2006)], arXiv:gr-qc/0211087.

[105] M. Abramowitz and I. Stegun, *Handbook of Mathematical Functions with Formulas, Graphs, and Mathematical Tables* (Dover Publications, Incorporated, 1974).

[106] D. E. Amos, Algorithm 644: A portable package for bessel functions of a complex argument and nonnegative order, ACM Trans. Math. Softw. **12**, 265–273 (1986).

[107] P. Virtanen *et al.*, SciPy 1.0: Fundamental Algorithms for Scientific Computing in Python, Nature Methods **17**, 261 (2020).

[108] M. Colleoni, F. A. R. Vidal, N. K. Johnson-McDaniel, T. Dietrich, M. Haney, and G. Pratten, IMRPhenomXP_NRTidalv2: An improved frequency-domain precessing binary neutron star waveform model, (2023), arXiv:2311.15978 [gr-qc].

[109] B. M. Barker and R. F. O'Connell, The gravitational interaction: spin, rotation, and quantum effects - a review., General Relativity and Gravitation **11**, 149 (1979).

[110] T. Damour, Coalescence of two spinning black holes: an effective one-body approach, Phys. Rev. D **64**, 124013 (2001), arXiv:gr-qc/0103018.

[111] E. Racine, Analysis of spin precession in binary black hole systems including quadrupole-monopole interaction, Phys. Rev. D **78**, 044021 (2008), arXiv:0803.1820 [gr-qc].

[112] P. Ajith *et al.*, Inspiral-merger-ringdown waveforms for black-hole binaries with non-precessing spins, Phys. Rev. Lett. **106**, 241101 (2011), arXiv:0909.2867 [gr-qc].

[113] P. Schmidt, I. W. Harry, and H. P. Pfeiffer, Numerical Relativity Injection Infrastructure, (2017), arXiv:1703.01076 [gr-qc].

[114] M. Ebersold, Y. Boetzel, G. Faye, C. K. Mishra, B. R. Iyer, and P. Jetzer, Gravitational-wave amplitudes for compact binaries in eccentric orbits at the third post-Newtonian order: Memory contributions, Phys. Rev. D **100**, 084043 (2019), arXiv:1906.06263 [gr-qc].

[115] C. Cutler *et al.*, The Last three minutes: issues in gravitational wave measurements of coalescing compact binaries, Phys. Rev. Lett. **70**, 2984 (1993), arXiv:astro-ph/9208005.

[116] W. H. Press, S. A. Teukolsky, W. T. Vetterling, and B. P. Flannery, *Numerical Recipes: The Art of Scientific Computing*, 3rd ed. (Cambridge University Press, 2007).

[117] F. J. Harris, On the use of windows for harmonic analysis with the discrete fourier transform, Proceedings of the IEEE **66**, 51 (1978).

[118] B. P. Abbott *et al.* (LIGO Scientific, Virgo), A guide to LIGO–Virgo detector noise and extraction of transient gravitational-wave signals, Class. Quant. Grav. **37**, 055002 (2020), arXiv:1908.11170 [gr-qc].

[119] C. Talbot, E. Thrane, S. Biscoveanu, and R. Smith, Inference with finite time series: Observing the gravitational Universe through windows, Phys. Rev. Res. **3**, 043049 (2021), arXiv:2106.13785 [astro-ph.IM].

[120] B. S. Sathyaprakash and S. V. Dhurandhar, Choice of filters for the detection of gravitational waves from coalescing binaries, Phys. Rev. D **44**, 3819 (1991).

[121] C. Cutler and E. E. Flanagan, Gravitational waves from merging compact binaries: How accurately can one extract the binary's parameters from the inspiral wave form?, Phys. Rev. D **49**, 2658 (1994), arXiv:gr-qc/9402014.

[122] S. Droz, D. J. Knapp, E. Poisson, and B. J. Owen, Gravitational waves from inspiraling compact binaries: Validity of the stationary phase approximation to the Fourier transform, Phys. Rev. D **59**, 124016 (1999), arXiv:gr-qc/9901076.

[123] J. Dormand and P. Prince, A family of embedded runge-kutta formulae, Journal of Computational and Applied Mathematics **6**, 19 (1980).

[124] L. F. Shampine, Some practical runge-kutta formulas, Mathematics of Computation **46**, 135 (1986).

[125] G. Pratten *et al.*, Computationally efficient models for the dominant and subdominant harmonic modes of precessing binary black holes, Phys. Rev. D **103**, 104056 (2021), arXiv:2004.06503 [gr-qc].

[126] A. Ramos-Buades, A. Buonanno, H. Estellés, M. Khalil, D. P. Mihaylov, S. Ossokine, L. Pompili, and M. Shiferaw, Next generation of accurate and ef-

ficient multipolar precessing-spin effective-one-body waveforms for binary black holes, Phys. Rev. D **108**, 124037 (2023), arXiv:2303.18046 [gr-qc].

[127] V. Varma, S. E. Field, M. A. Scheel, J. Blackman, D. Gerosa, L. C. Stein, L. E. Kidder, and H. P. Pfeiffer, Surrogate models for precessing binary black hole simulations with unequal masses, Phys. Rev. Research. **1**, 033015 (2019), arXiv:1905.09300 [gr-qc].

[128] M. Cabero, A. B. Nielsen, A. P. Lundgren, and C. D. Capano, Minimum energy and the end of the inspiral in the post-Newtonian approximation, Phys. Rev. D **95**, 064016 (2017), arXiv:1602.03134 [gr-qc].

[129] J. M. Bardeen, W. H. Press, and S. A. Teukolsky, Rotating black holes: Locally nonrotating frames, energy extraction, and scalar synchrotron radiation, Astrophys. J. **178**, 347 (1972).

[130] X. Zhao, M. Kesden, and D. Gerosa, Nutational resonances, transitional precession, and precession-averaged evolution in binary black-hole systems, Phys. Rev. D **96**, 024007 (2017), arXiv:1705.02369 [gr-qc].

[131] L. N. Trefethen, *Approximation Theory and Approximation Practice*, Other Titles in Applied Mathematics, Vol. 128 (SIAM, 2013) p. 318.

[132] B. P. Abbott *et al.*, Prospects for observing and localizing gravitational-wave transients with advanced LIGO, advanced virgo and KAGRA, Living Reviews in Relativity **23**, 10.1007/s41114-020-00026-9 (2020).

[133] B. P. Abbott *et al.*, *Noise curves used for Simulations in the update of the Observing Scenarios Paper*, Tech. Rep. LIGO-T2000012 (LIGO Virgo KAGRA Collaboration, 2020).

[134] P. C. Peters and J. Mathews, Gravitational radiation from point masses in a Keplerian orbit, Phys. Rev. **131**, 435 (1963).

[135] L. S. Finn and D. F. Chernoff, Observing binary inspiral in gravitational radiation: One interferometer, Phys. Rev. D **47**, 2198 (1993), arXiv:gr-qc/9301003.

[136] I. Harry, S. Privitera, A. Bohé, and A. Buonanno, Searching for Gravitational Waves from Compact Binaries with Precessing Spins, Phys. Rev. D **94**, 024012 (2016), arXiv:1603.02444 [gr-qc].

[137] C. Talbot and E. Thrane, Measuring the binary black hole mass spectrum with an astrophysically motivated parameterization, Astrophys. J. **856**, 173 (2018), arXiv:1801.02699 [astro-ph.HE].

[138] LIGO Scientific Collaboration, LIGO Algorithm Library - LALSuite, free software (GPL) (2018).

[139] A. Buonanno, B. Iyer, E. Ochsner, Y. Pan, and B. S. Sathyaprakash, Comparison of post-Newtonian templates for compact binary inspiral signals in gravitational-wave detectors, Phys. Rev. D **80**, 084043 (2009), arXiv:0907.0700 [gr-qc].

[140] R. Sturani, Note on the derivation of the angular momentum and spin precessing equations in SpinTaylor codes (2015).

[141] S. Isoyama, R. Sturani, and H. Nakano, Post-Newtonian templates for gravitational waves from compact binary inspirals 10.1007/978-981-15-4702-7_31-1 (2020), arXiv:2012.01350 [gr-qc].

[142] D. Gerosa, M. Kesden, R. O'Shaughnessy, A. Klein, E. Berti, U. Sperhake, and D. Trifirò, Precessional instability in binary black holes with aligned spins, Phys. Rev. Lett. **115**, 141102 (2015), arXiv:1506.09116 [gr-qc].

[143] V. Varma, M. Mould, D. Gerosa, M. A. Scheel, L. E.

Kidder, and H. P. Pfeiffer, Up-down instability of binary black holes in numerical relativity, Phys. Rev. D **103**, 064003 (2021), arXiv:2012.07147 [gr-qc].

[144] G. Pratten, S. Husa, C. Garcia-Quiros, M. Colleoni, A. Ramos-Buades, H. Estelles, and R. Jaume, Setting the cornerstone for a family of models for gravitational waves from compact binaries: The dominant harmonic for nonprecessing quasicircular black holes, Phys. Rev. D **102**, 064001 (2020), arXiv:2001.11412 [gr-qc].

[145] A. H. Nitz, A. Lundgren, D. A. Brown, E. Ochsner, D. Keppel, and I. W. Harry, Accuracy of gravitational waveform models for observing neutron-star–black-hole binaries in Advanced LIGO, Phys. Rev. D **88**, 124039 (2013), arXiv:1307.1757 [gr-qc].

[146] P. Kumar, K. Barkett, S. Bhagwat, N. Afshari, D. A. Brown, G. Lovelace, M. A. Scheel, and B. Szilágyi, Accuracy and precision of gravitational-wave models of inspiraling neutron star-black hole binaries with spin: Comparison with matter-free numerical relativity in the low-frequency regime, Phys. Rev. D **92**, 102001 (2015), arXiv:1507.00103 [gr-qc].

[147] M. Pürrer and C.-J. Haster, Gravitational waveform accuracy requirements for future ground-based detectors, Phys. Rev. Res. **2**, 023151 (2020), arXiv:1912.10055 [gr-qc].

[148] M. Maggiore *et al.* (ET), Science Case for the Einstein Telescope, JCAP **03**, 050, arXiv:1912.02622 [astro-ph.CO].

[149] M. Branchesi *et al.*, Science with the Einstein Telescope: a comparison of different designs, JCAP **07**, 068, arXiv:2303.15923 [gr-qc].

[150] D. Reitze *et al.*, Cosmic Explorer: The U.S. Contribution to Gravitational-Wave Astronomy beyond LIGO, Bull. Am. Astron. Soc. **51**, 035 (2019), arXiv:1907.04833 [astro-ph.IM].

[151] A. Bohé *et al.*, Improved effective-one-body model of spinning, nonprecessing binary black holes for the era of gravitational-wave astrophysics with advanced detectors, Phys. Rev. D **95**, 044028 (2017), arXiv:1611.03703 [gr-qc].

[152] M. Boyle *et al.*, The SXS Collaboration catalog of binary black hole simulations, Class. Quant. Grav. **36**, 195006 (2019), arXiv:1904.04831 [gr-qc].

[153] B. Moore, M. Favata, K. G. Arun, and C. K. Mishra, Gravitational-wave phasing for low-eccentricity inspiralling compact binaries to 3PN order, Phys. Rev. D **93**, 124061 (2016), arXiv:1605.00304 [gr-qc].

[154] S. A. Usman *et al.*, The PyCBC search for gravitational waves from compact binary coalescence, Class. Quant. Grav. **33**, 215004 (2016), arXiv:1508.02357 [gr-qc].

[155] B. Zackay, T. Venumadhav, J. Roulet, L. Dai, and M. Zaldarriaga, Detecting gravitational waves in data with non-stationary and non-Gaussian noise, Phys. Rev. D **104**, 063034 (2021), arXiv:1908.05644 [astro-ph.IM].

[156] F. Aubin *et al.*, The MBTA pipeline for detecting compact binary coalescences in the third LIGO–Virgo observing run, Class. Quant. Grav. **38**, 095004 (2021), arXiv:2012.11512 [gr-qc].

[157] A. H. Nitz, S. Kumar, Y.-F. Wang, S. Kastha, S. Wu, M. Schäfer, R. Dhurkunde, and C. D. Capano, 4-OGC: Catalog of Gravitational Waves from Compact Binary Mergers, Astrophys. J. **946**, 59 (2023), arXiv:2112.06878 [astro-ph.HE].

[158] S. Sakon *et al.*, Template bank for compact binary merg-

ers in the fourth observing run of Advanced LIGO, Advanced Virgo, and KAGRA, Phys. Rev. D **109**, 044066 (2024), arXiv:2211.16674 [gr-qc].

[159] S. Klimenko, I. Yakushin, A. Mercer, and G. Mitselmakher, Coherent method for detection of gravitational wave bursts, Class. Quant. Grav. **25**, 114029 (2008), arXiv:0802.3232 [gr-qc].

[160] R. Lynch, S. Vitale, R. Essick, E. Katsavounidis, and F. Robinet, Information-theoretic approach to the gravitational-wave burst detection problem, Phys. Rev. D **95**, 104046 (2017), arXiv:1511.05955 [gr-qc].

[161] M. Drago *et al.*, Coherent WaveBurst, a pipeline for unmodeled gravitational-wave data analysis 10.1016/j.softx.2021.100678 (2020), arXiv:2006.12604 [gr-qc].

[162] T. Bayes, Rev., An essay toward solving a problem in the doctrine of chances, Phil. Trans. Roy. Soc. Lond. **53**, 370 (1764).

[163] J. Veitch *et al.*, Parameter estimation for compact binaries with ground-based gravitational-wave observations using the LALInference software library, Phys. Rev. D **91**, 042003 (2015), arXiv:1409.7215 [gr-qc].

[164] E. Thrane and C. Talbot, An introduction to Bayesian inference in gravitational-wave astronomy: parameter estimation, model selection, and hierarchical models, Publ. Astron. Soc. Austral. **36**, e010 (2019), [Erratum: Publ.Astron.Soc.Austral. 37, e036 (2020)], arXiv:1809.02293 [astro-ph.IM].

[165] R. E. Kass and A. E. Raftery, Bayes factors, Journal of the american statistical association **90**, 773 (1995).

[166] G. Ashton *et al.*, BILBY: A user-friendly Bayesian inference library for gravitational-wave astronomy, Astrophys. J. Suppl. **241**, 27 (2019), arXiv:1811.02042 [astro-ph.IM].

[167] R. J. E. Smith, G. Ashton, A. Vajpeyi, and C. Talbot, Massively parallel Bayesian inference for transient gravitational-wave astronomy, Mon. Not. Roy. Astron. Soc. **498**, 4492 (2020), arXiv:1909.11873 [gr-qc].

[168] I. M. Romero-Shaw *et al.*, Bayesian inference for compact binary coalescences with bilby: validation and application to the first LIGO–Virgo gravitational-wave transient catalogue, Mon. Not. Roy. Astron. Soc. **499**, 3295 (2020), arXiv:2006.00714 [astro-ph.IM].

[169] J. S. Speagle, DYNESTY: a dynamic nested sampling package for estimating Bayesian posteriors and evidences, Mon. Not. Roy. Astron. Soc. **493**, 3132 (2020), arXiv:1904.02180 [astro-ph.IM].

[170] C. L. Rodriguez, B. Farr, V. Raymond, W. M. Farr, T. B. Littenberg, D. Fazi, and V. Kalogera, Basic Parameter Estimation of Binary Neutron Star Systems by the Advanced LIGO/Virgo Network, Astrophys. J. **784**, 119 (2014), arXiv:1309.3273 [astro-ph.HE].

[171] P. A. R. Ade *et al.* (Planck), Planck 2015 results. XIII. Cosmological parameters, Astron. Astrophys. **594**, A13 (2016), arXiv:1502.01589 [astro-ph.CO].

[172] P. Schmidt, F. Ohme, and M. Hannam, Towards models of gravitational waveforms from generic binaries II: Modelling precession effects with a single effective precession parameter, Phys. Rev. D **91**, 024043 (2015), arXiv:1408.1810 [gr-qc].

[173] K. Chatziioannou, N. Cornish, A. Klein, and N. Yunes, Spin-Precession: Breaking the Black Hole–Neutron Star Degeneracy, Astrophys. J. Lett. **798**, L17 (2015), arXiv:1402.3581 [gr-qc].

[174] G. Pratten, P. Schmidt, R. Buscicchio, and L. M. Thomas, Measuring precession in asymmetric compact binaries, Phys. Rev. Res. **2**, 043096 (2020), arXiv:2006.16153 [gr-qc].

[175] M. Favata, C. Kim, K. G. Arun, J. Kim, and H. W. Lee, Constraining the orbital eccentricity of inspiralling compact binary systems with Advanced LIGO, Phys. Rev. D **105**, 023003 (2022), arXiv:2108.05861 [gr-qc].

[176] E. Roebber *et al.*, Milky Way Satellites Shining Bright in Gravitational Waves, Astrophys. J. Lett. **894**, L15 (2020), arXiv:2002.10465 [astro-ph.GA].

[177] R. Buscicchio, A. Klein, E. Roebber, C. J. Moore, D. Gerosa, E. Finch, and A. Vecchio, Bayesian parameter estimation of stellar-mass black-hole binaries with LISA, Phys. Rev. D **104**, 044065 (2021), arXiv:2106.05259 [astro-ph.HE].

[178] A. Klein *et al.*, The last three years: multiband gravitational-wave observations of stellar-mass binary black holes, (2022), arXiv:2204.03423 [astro-ph.HE].

[179] G. Pratten, P. Schmidt, H. Middleton, and A. Vecchio, Precision tracking of massive black hole spin evolution with LISA, Phys. Rev. D **108**, 124045 (2023), arXiv:2307.13026 [gr-qc].

[180] R. Buscicchio, J. Torrado, C. Caprini, G. Nardini, N. Karnesis, M. Pieroni, and A. Sesana, Stellar-mass black-hole binaries in LISA: characteristics and complementarity with current-generation interferometers, (2024), arXiv:2410.18171 [astro-ph.HE].

[181] S. Ghosh, P. Kolitsidou, and M. Hannam, First frequency-domain phenomenological model of the multipole asymmetry in gravitational-wave signals from binary-black-hole coalescence, Phys. Rev. D **109**, 024061 (2024), arXiv:2310.16980 [gr-qc].

[182] E. E. Flanagan and T. Hinderer, Constraining neutron star tidal Love numbers with gravitational wave detectors, Phys. Rev. D **77**, 021502 (2008), arXiv:0709.1915 [astro-ph].

[183] H. Yang, W. E. East, V. Paschalidis, F. Pretorius, and R. F. P. Mendes, Evolution of Highly Eccentric Binary Neutron Stars Including Tidal Effects, Phys. Rev. D **98**, 044007 (2018), arXiv:1806.00158 [gr-qc].

[184] P. Schmidt and T. Hinderer, Frequency domain model of f-mode dynamic tides in gravitational waveforms from compact binary inspirals, Phys. Rev. D **100**, 021501 (2019), arXiv:1905.00818 [gr-qc].

[185] M. LaHaye, H. Yang, B. Bonga, and Z. Lyu, Efficient fully precessing gravitational waveforms for binaries with neutron stars, Phys. Rev. D **108**, 043018 (2023), arXiv:2212.04657 [gr-qc].

[186] E. Dones, Q. Henry, and L. Bernard, Tidal contributions to the full gravitational waveform to the second-and-a-half post-Newtonian order, (2024), arXiv:2412.14249 [gr-qc].

[187] W. Tulczyjew, Equations of motion of rotating bodies in general relativity theory, Acta Phys. Polon. **18**, 37 (1959), [Erratum: Acta Phys. Polon. **18**, 534 (1959)].

[188] W. G. Dixon, Dynamics of extended bodies in general relativity. I. Momentum and angular momentum, Proc. Roy. Soc. Lond. A **314**, 499 (1970).

[189] K. G. Arun, L. Blanchet, B. R. Iyer, and S. Sinha, Third post-Newtonian angular momentum flux and the secular evolution of orbital elements for inspiralling compact binaries in quasi-elliptical orbits, Phys. Rev. D **80**, 124018 (2009), arXiv:0908.3854 [gr-qc].

[190] M. Maggiore, *Gravitational Waves. Vol. 1: Theory and Experiments*, Oxford Master Series in Physics (Oxford University Press, 2007) p. 572.